Universidade de Évora

Departamento de Física

IIFA - Instituto de Investigação e Formação Avançada

Cloud Characterization in the presence of aerosols over Portugal region

Dina da Conceição Nunes dos Santos

Supervisor: Professora Doutora Maria João Tavares da Costa
Co-Supervisor: Professora Doutora Ana Maria Almeida e Silva

A dissertation submitted to the University of Évora to obtain the
Degree of Doctor in Earth and Space Sciences

Évora

2011

"The scientist does not study nature because it is useful to do so. He studies it because he takes pleasure in it, and he takes pleasure in it because it is beautiful. If nature were not beautiful it would not be worth knowing, and life would not be worth living…"

Henri Poincaré

To José Firmino dos Santos,

my grandfather!

Acknowledgments

This space is dedicated to those who gave their contribution and made the realization of this thesis possible. To all of them I leave here my sincere gratitude, it is a pleasure to thank them.

To start, I express my gratitude to my Ph.D. supervisors Professora Doutora Maria João Costa and Professora Doutora Ana Maria Silva. Their guidance, enthusiasm, inspiration, their support and their great efforts to explain things clearly and simply, were fundamental. Throughout my thesis-writing period, they provided encouragement, sound advice, good teaching, good company, and lots of good ideas. I would have been lost without them. I am also grateful for the freedom of action that contributed to my personal development.

I am grateful also to Professor Doutor Rui Salgado for the endless support, patience and encouragement.

I am indebted to my friends and colleagues, especially to Patrick Sousa, Telma Teixeira, Carla Silvestre, Vera Rocha, Dário Passos, Sandra Brás, Miguel Potes, Ana Domingues and Sérgio Pereira for the never-ending support. Also a special thank to my goddaughters, Lara Trindade Agostinho and Marlene Costa, for the love that they gave, and still giving, me. A special thought to my very special friend Elsa Trindade Agostinho, for the endless care, even when we seem to be apart.

To Vitor Pereira, not necessarily for coming along at the right time, trough this last 19 years ☺ , but for the wonderful person he is. And for the incredible amount of patience, support, care and love that he gave to me in the last months. It's time to start on that list of things to do "Yes, after the thesis...".

To my dearly loved parents, José Raimundo Santos and Celisa Nunes dos Santos, I'm grateful for never letting disappear the smile in my face, for always believing and supporting me in all my adventures, even the most daring.

To my treasured grandmother, Maria Celeste Gago, I would like to show my gratitude for her constant care, affection and enormous support. To my grandparents, José Nunes Viegas e Mercês da Conceição Dias, I am grateful for never leaving me. And for last, but no least, I would like to give a special gratitude to my grandfather, José Firmino do Santos, who past way this year, and who I miss a lot... To him I dedicate this thesis!

I also would like to thank all those institutions that have contributed to this thesis providing data and financial support:

- MODIS data are courtesy of NASA Earth Science Enterprise and the official algorithms were developed by the MODIS Science Teams. They were processed by the MODIS Adaptive Processing System (MODAPS) and Goddard Distributed Active Archive Center (DAAC), the latter being in charge of archiving and distribution.

- The NOAA Air Resources Laboratory (ARL) for the provision of the HYSPLIT transport and dispersion model and/or READY website (http://www.arl.noaa.gov/ready.php) used in this work.

This thesis was financially supported by the FCT - Fundação para a Ciência e Tecnologia, trough the grant SFRH/BD/27870/2006.

Table of Contents

Resumo

“Caracterização das nuvens em presença de aerossóis na área de Portugal”

Este trabalho investiga a interacção entre aerossóis minerais, do tipo poeiras do deserto, e propriedades de nuvens sobre a Península Ibérica e Oceano Atlântico circundante. Esta interacção é feita utilizando modelação atmosférica regional e dados de detecção remota, fornecidas por satélite e medições in situ.

A determinação das propriedades dos aerossóis fornece informações sobre a altitude da camada de aerossóis e a determinação das propriedades das nuvens, influenciadas pela presença de aerossóis, fornece informações sobre as alterações que essas nuvens podem sofrer. O forçamento radiativo, devido a nuvens e a aerossóis, no topo da atmosfera e à superfície, também são estimados.

Os resultados deste estudo confirmam que os aerossóis minerais alteram as propriedades das nuvens. Com esta pesquisa é feita uma contribuição para melhor compreender a interacção de nuvens/aerossóis, bem como sua interacção com a radiação. É obtida também uma quantificação dos efeitos radiativos devido a nuvens e/ou aerossóis.

Abstract

This work investigates the interaction between mineral desert dust aerosols and cloud properties over the Iberian Peninsula and the Atlantic Ocean surrounding area. This interaction is studied using regional atmospheric modeling and remote sensing data, provided by satellite and in situ measurements.

The assessment of the aerosol properties provides information on the aerosol layers altitude and the cloud properties determination, influenced by the desert dust aerosols presence, gives information about the alterations that clouds may suffer. The aerosol and cloud radiative forcing at the top of the atmosphere and at surface levels are also estimated.

The results of this study are consistent with mineral aerosols altering cloud properties and changing cloud amounts. With this research a contribution is made in order to better understand the interaction of clouds/aerosols as well as their interaction with radiation. A contribution is also made for the quantification of cloud/aerosol radiative effects.

List of Principal Acronyms

AERONET – AErosol RObotic NETwork

AIRS - Atmospheric InfraRed Sounder

CALIPSO - Cloud–Aerosol Lidar and Infrared Pathfinder Satellite Observation

CCN - Cloud Condensation Nuclei

CERES - Clouds and the Earth's Radiant Energy System

CGE – Centro de Geofísica de Évora

CLBASCONV - base height of convective clouds

CLDFR - cloud fraction

CLTOPCONV - top height of convective clouds

CLWER - Cloud Liquid Water Effective Radius

COD - Cloud Optical Depth

CRF - Cloud Radiative Forcing

DD – Desert Dust

ETS – Equitable Threat Score

HYSPLIT - Hybrid Single Particle Lagragean Integrated Trajectory

IN – Ice Nuclei

IPCC – Intergovernmental Panel on Climate Change

IR - InfraRed

LIDAR - LIght Detection And Ranging

LW – LongWave

LWC – Liquid Water Content

LWCRF - Cloud LongWave Radiative Forcing

LWF - LongWave radiative Forcing

LWP – Liquid Water Path

MODIS - MODerate resolution Imaging Spectrometer

NOAA - National Oceanic and Atmospheric Administration

UTC – Coordinated Universal Time

SurfSWF - Surface ShortWave radiative Forcing

SW – ShortWave

SWCRF - Cloud ShortWave Radiative Forcing

SWF - ShortWave radiative Forcing

TOA – Top Of the Atmosphere

TOASWF - Top Of the Atmosphere ShortWave radiative Forcing

List of Principal Symbols

c - Velocity of light in vacuum ($2,9979 \times 10^{-34}\ ms^{-1}$);

ds - Thickness element (*m*);

D_p - Diameter of spherical aggregates (cm);

F_0 - Total solar flux density (Wm^{-2});

F_{0_λ} - Monochromatic solar flux density (Wm^{-2});

$F^{\uparrow}$ - Upward total flux density (Wm^{-2});

$F^{\downarrow}$ - Downward total flux density (Wm^{-2});

F^{net} - Net radiation (Wm^{-2});

g - Gravitational acceleration ($m\,s^{-2}$);

H - Model's top height (km);

h - Planck constant ($6.6262 \times 10^{-34}\ J\,s$);

I_λ - Monochromatic radiance ($Wm^{-2}\mu m^{-1} sr^{-1}$);

I_{0_λ} - TOA incident solar monochromatic radiance ($Wm^{-2}\mu m^{-1} sr^{-1}$);

J_λ - Monochromatic source function ($Wm^{-2}\mu m^{-1} sr^{-1}$);

K - Von Karman's constant;

k - Boltzmann constant ($1.3806 \times 10^{-23}\ J\,k^{-1}$);

k_λ^e - Mass extinction cross section ($m^2 kg^{-1}$);

k_λ^a - Mass absorption cross section ($m^2 kg^{-1}$);

k_λ^s - Mass scattering cross section ($m^2 kg^{-1}$);

m - Mass (kg);

m_{λ} - Refractive index;

$m_{r_{\lambda}}$ - Real part of the refractive index;

$m_{i_{\lambda}}$ - Imaginary part of the refractive index;

$n(r)$ - Particle size distribution ($\mu m^{-1} cm^{-3}$);

N - Total number of pairs of modeled and observed values;

N_0 - Number of observed values above the threshold value;

N_c - Number of correct modeled values above the threshold value;

N_p - Number of modeled values above the threshold value;

$P_{\lambda}(\Theta)$ - Scattering phase function;

Q_s - Saltation flux ($g\,cm^{-1}\,s^{-1}$);

Q_{λ}^{e} - Mie extinction efficiency;

Q_{λ}^{s} - Mie scattering efficiency;

r - Particle radius (μm);

r_{eff} - Effective radius (μm);

Re - Reynolds number;

R_g - Surface roughness (μm);

$u(z)$ - Wind velocity (ms^{-1});

u_* - Wind friction velocity (ms^{-1});

U_t - Threshold friction velocity (ms^{-1});

$V_{g,p}$ - Particle gravitational velocity (ms^{-1});

W - Soil humidity ($\%\, air\, mass/dry\, sol\, mass$);

W_s - Soil residual humidity ($\%\, air\, mass/dry\, sol\, mass$);

Z - Altitude above the sea level (km);

Z_S - Surface altitude in each geographical position (km);

$\overline{Z}$ - Model's vertical coordinate (km);

β_λ^e - Volume extinction coefficient (m^{-1});

β_λ^s - Volume scattering coefficient (m^{-1});

ΔF - Total radiative forcing (Wm^{-2});

ε_λ - Emissivity of the atmosphere;

Θ - Scattering angle (º);

θ - Zenith angle (º);

θ_0 - Solar zenith angle (º);

λ - Wavelength (μm);

μ - Cosine of the zenith angle;

μ_0 - Cosine of the solar zenith angle;

ρ - Density ($kg\, m^{-3}$);

ρ_a - Air density ($kg\, m^{-3}$);

ρ_p - Density of the spherical aggregates ($kg\, m^{-3}$);

σ_λ^s - Scattering cross section (m^2);

τ_λ - Optical thickness;

τ - Tangential constraint exercised by the atmospheric flow to the soil ($N\,m^{-2}$);

ϕ - Azimuth angle (º);

ϕ_0 - Solar azimuth angle (º);

$\phi - \phi_0$ - Relative azimuth angle (º);

ν - Kinematic viscosity ($m^2\,s^{-1}$);

χ - Mie size parameter;

ϖ - Single scattering albedo;

1. Introduction

The effects of aerosol particles and clouds on atmospheric dynamics, weather, climate, and public health are one of the central topics in contemporary environmental research. Aerosol particles and clouds influence the Earth's radiative energy budget by scattering, absorption and emission of solar and terrestrial radiation (Charlson and Heintzenberg, 1995, Houghton et al., 2001; Andreae et al., 2005; Lohmann and Feichter, 2005, Forster et al., 2007, Andreae and Rosenfeld, 2008, Santos et al., 2008, 2011). Furthermore, they play key roles in the hydrological cycle and in the formation of precipitation (Lohmann and Feichter, 2005; Pöschl, 2005; Andreae and Rosenfeld, 2008; Rosenfeld et al., 2008; Heintzenberg and Charlson, 2009, Costa et al., 2010).

Despite the significance of clouds and aerosols for the climate system, the present knowledge of clouds and aerosols and the complex atmospheric processes associated with them is very far from complete (e. g. IPCC 2007, Baker and Peter 2008). As a result, the capability of state-of-the-art atmospheric models to reproduce observed cloud and aerosol parameters is frequently inadequate. Furthermore, several cloud processes take place in small spatial scales that are not resolute by present-day weather and climate forecast models, meaning that the majority of the cloud processes must be parameterized. The clouds representation and their interaction with aerosols and radiation constitute the greatest source of uncertainty in the estimation of future climate (IPCC, 2007). These uncertainties can at least in part be attributed to the enormous changeability that clouds reveal in space and time making them difficult to model and monitor.

In this work the interaction between mineral desert dust aerosols and cloud properties over Iberian Peninsula and the Atlantic Ocean surrounding area is considered. This interaction is studied using regional atmospheric modelling and remote sensing data, provided by satellite and in situ measurements. The results of this study are consistent with mineral aerosols altering cloud properties and changing cloud amounts.

1.1 Notes on state-of-the-art investigations on clouds, aerosols and their interaction

The term "atmospheric aerosol" covers a wide range of particle types, suspended in the atmosphere, having different compositions, sizes, shapes, and optical properties. The aerosol quantity in the atmosphere is generally quantified by mass concentration or by an optical property, aerosol optical depth (AOD). AOD is the vertical integral through the entire height of the atmosphere of the fraction of incident light either scattered or absorbed by airborne particles (Chin et al., 2009).

Cloud droplets and ice particles form in the atmosphere by condensation of supersaturated water vapour on aerosol particles. Cloud condensation nuclei (CCN) are aerosol particles that have the potential to nucleate liquid cloud droplets and the aerosol particles that can induce the ice crystals formation are called ice nuclei (IN) (Andreae and Rosenfeld, 2008). According to Andreae and Rosenfeld (2008) when clouds form in air with elevated CCN concentrations, contain higher concentrations of smaller cloud droplets with respect to clouds forming in cleaner environments (low CCN concentrations); this reduction in the size of the droplets slows their coalescence into raindrops (e.g., Squires and Twomey, 1966, Twomey, 1977). When CCN concentrations are low, rain is formed more rapidly, not including necessarily the participation of an ice phase, even in deep convective clouds with warm bases. These clouds prevail in the tropics, as well as in the mid-latitudes, during summer. Important progress has been made in recent years in identify the beginning processes that produce cloud-active aerosols, the properties that allow aerosols to act as CCN and IN, the effects of aerosols on cloud physics and precipitation and the consequences for the climate system (Hitzenberger et al., 1997; Levin et al., 2003. Lohmann, 2006; Lohmann and Hoose, 2009; Wiacek and Lohmann, 2010; Isotta et al., 2011).

Aerosols and clouds interactions are the issue of substantial scientific investigation, due to the significance of clouds in controlling climate (e.g., Levin and Ganor, 1996; Pruppacher and Klett, 1997; Rosenfeld et al., 2001; Sassen, 2002; Myhre et al., 2007; Rosenfeld, 2006a,b; Forster et al., 2007; Klüser and Holzer-Popp, 2010). The aerosol effects on the cloud formation and precipitation can lead to deep alterations in the dynamics and radiative properties of cloud systems (see Figures. 2.5 and 2.11).

These processes may influence the strength and organization of heavy weather events like hail and rainstorms and cascade all the way to altering the atmosphere global circulation and the Earth's energy budget (Andreae et al., 2004; Lohmann and Feichter, 2005; Rosenfeld et al., 2008; Heintzenberg and Charlson, 2009).

As one of the four key terrestrial sources of atmospheric aerosols (desert dust, biomass burning, biogenic and anthropogenic air pollution), mineral dust is responsible for remarkable climate forcing. The Saharan desert contributes with the largest concentrations of dust to the atmosphere (e. g. Swap et al., 1996; D'Almeida, 1986; Israelevich et al., 2002). This dust can contribute to CCN, giant CCN (GCCN), and IN concentrations while suspended in the atmosphere. Current studies have proposed that dust from arid regions can influence, globally, the cloud formation and cloud microphysics (e. g. Sassen, 2002; DeMott et al., 2003; Mahowald and Kiehl, 2003; Stith et al., 2009; Twohy et al., 2009; Min et al., 2009; Koehler et al., 2010).

The presence of aerosols and clouds in the atmosphere modifies the amount of sunlight scattered back to space, absorbed in the atmosphere and arriving at the surface, as it was mentioned before. Such a perturbation of solar radiation by aerosols and clouds is nominated aerosol and/or cloud radiative forcing (RF). The RF estimated at the top of the atmosphere (TOA), the bottom of the atmosphere, or every altitude in the middle, will result in different values, since the vertical aerosol distribution influences the radiative effect both at the TOA and surface levels, especially when aerosols have strong absorption of shortwave radiation (e.g., Haywood and Ramaswamy, 1998; Costa et al., 2004a, b, 2006; Meloni et al., 2005, Santos et al., 2008, 2011). Still, the aerosol and/or cloud RF remains difficult to assess.

Because mineral dust particles are of a quite large size and since it becomes lofted to high altitudes in the troposphere, in addition to the shortwave (SW) RF, it may exert a noteworthy long-wave (LW) RF. The global mean SW RF will be negative due to the predominantly scattering nature in the solar spectrum (although partial absorption may lead to a local positive radiative forcing over high surface albedos and clouds) and the global mean LW RF will be positive (Ramaswamy et al., 2001).

Among other net RF calculations, the ones based on Miller and Tegen (1998) estimate the RF to be -0.22 Wm^{-2} in the SW and +0.16 Wm^{-2} in the LW, resulting in a net RF of -0.06 Wm^{-2}. Hansen et al. (1998) perform similar calculations and calculate a net RF of -0.12 Wm^{-2} by assuming a different vertical distribution, different optical parameters and using a different global model. Jacobson (2001) used a multi-component global aerosol model to estimate the direct RF to be -0.062 Wm^{-2} in the SW and +0.05 Wm^{-2} in the LW, resulting in a net radiative forcing of -0.012 Wm^{-2}. Geographical distributions of the RF (Tegen et al., 1996) show regions of positive and negative forcing. Positive forcing have a propensity to exist over regions of high surface reflectance and negative radiative forcings tend to subsist over areas of low surface reflectance. This is due to the dependency of the forcing on surface reflectance and the supplementary effects of the LW radiative forcing.

Because the resultant global mean net RF is a residual obtained by summing the SW and the LW radiative forcings which are of roughly comparable magnitudes, the uncertainty in the RF is large and even the sign is unsure due to the competing nature of the SW and LW effects. The studies above suggest that the SW forcing is likely to be of a larger magnitude than the LW radiative forcing, which indicates that the net RF is likely to be negative, although a net positive RF cannot be ruled out.

Different clouds induce diverse climate effects. They both cool (by reflecting sunlight) and warm (by trapping IR radiation) the atmosphere. Depending on the type and altitude of the cloud different effects can dominate. Their huge changeability and innumerable interdependencies implicated makes quantifying their global effect very difficult.

In the third IPCC assessment report (IPCC, 2001), the cloud albedo effect was found to be a key uncertainty in the climate radiative forcing. Although a best estimate of the radiative forcing associated with the cloud albedo effect is now given in the IPCC AR4 with a value of -0.7 Wm^{-2} and a 90% confidence range from -1.8 Wm^{-2} to -0.3 Wm^{-2}, the uncertainties remain large and the level of scientific understanding low. This radiative forcing still carries the greatest uncertainty of all climate forcing mechanisms reported by the IPCC AR4 (2007).

The restricted quantity of cloud measurements and thus the restricted knowledge of cloud microphysical properties in association to their effects on the radiative budget and on the vertical energy redistribution within the atmosphere is part of the reason for the discussed uncertainties. Cloud observations are sparse, compared to other meteorological variables like temperature, pressure and humidity, even though these observations are indispensable in order to better understand the complex processes associated with clouds including their interaction with radiation. This understanding is important for the advance of the cloud representation and cloud processes in numerical weather prediction (NWP) and climate models (e.g. Hogan et al., 2001, Hogan et al., 2003a,b; Brooks et al., 2005; Illingworth et al., 2007; Hogan et al., 2009; Shonk et al., 2010a, b).

The quantitative knowledge and predictability of aerosol and cloud properties, interactions and effects in the climate system are, though, very limited. The lack of coincident in-situ measurements of cloud microphysical properties and aerosol characteristics within clouds has been a severe impediment to assess detailed cloud-resolving models that can be used for acquire a more complete understanding of aerosol-cloud interactions. The major difficulty has been the complexity to investigate and characterize these properties and interactions by in-situ and remote sensing observations (Andreae and Rosenfeld, 2008; Rosenfeld et al., 2008; Heintzenberg and Charlson, 2009, Costa et al., 2010.).

According to Jacobson (1998), since the introduction of the atmospheric computer modelling in 1948, models have been applied to study weather and/or climate on urban, regional, and global scales. Several fundamental weather variables comprise wind direction, wind speed, temperature, pressure, relative humidity, and rainfall at a given location or averaged over a region. One intention of developing a model is to better understand the physical, chemistry, dynamical, and radiative properties of air pollution and meteorology. A second purpose is to develop the model so that it may be used for forecasting. According to Lafore et al.(1998), numerical models for research on atmospheric processes are becoming progressively more complex tools as the considered physical processes grow in number and complexity and the range of scales of interest expands (Rummukainen, 2010).

In the 80's, French climate researchers develop several models and used them independently. Approximately 15 years later, a consensus was reached in the French community of meso- and micro-scale modellers of starting a new more efficient project, and develope a single, all-purpose model. According to Lafore et al.(1998), this model should have the capacity to represent all dynamical and physical processes of interest to our community, at a reasonable quality-cost ratio. It should also be user-friendly, in order to allow rapid acquaintance for new users and students. It should be easily adaptable to a large number of sites. As a direct outcome, the Meso-NH model (Lafore et al., 1998) was developed by a dedicated team of scientists during the period 1994-1997 (http://mesonh.aero.obs-mip.fr/mesonh/).

The Meso-NH Atmospheric Simulation System is a joint effort of the Centre National de Recherches Météorologiques and Laboratoire d'Aérologie. It contains some elements; a numerical model capable to simulate the atmospheric motions, ranging from the large meso-alpha scale down to the micro-scale, with a comprehensive physical package, a flexible file manager, an ensemble of facilities to prepare initial states, either idealized or interpolated from meteorological analyses or forecasts, a flexible post-processing and graphical facility to visualize the results, and an ensemble of interactive procedures to control these functions. Meso-NH is designed as a research tool for small and meso-scale atmospheric processes.

1.2 Focus of this study

The general goals of this research can be enlighten by the followed subjects:

- ✓ To assess the model ability to simulate the behaviour of desert dust aerosols and low level clouds in the atmosphere;

- ✓ To estimate the radiative forcing due to mineral desert dust aerosols and to investigate the effect of different surfaces on the dust radiative forcing;
- ✓ To investigate the possible modifications that low level clouds may suffer due the presence of mineral dust aerosols;
- ✓ To estimate the radiative forcing due to low level clouds in an atmosphere where desert dust aerosols are present or absent.

With this study a contribution is made in order to better understand the interaction of low level clouds/aerosols as well as their interaction with solar or IR radiation. With this research, a contribution is also done towards the quantification of low level cloud/aerosol radiative effects.

1.3 Thesis Structure

This thesis is divided into 4 major chapters.

The first chapter introduces the thesis, presenting a review of the related work, highlighting the central role that clouds, aerosols and their interactions, play on studies regarding, especially, the modeling of cloud-aerosols interactions and their interaction with radiation. Also the general goals of this research are presented in this chapter.

In chapter 2 the tools used, as well as the methodology of the research work developed are presented. In the first, of its four sections, the general description of the meteorological model MesoNH is provided and theoretical aspects related. The second and third sections deal with the description of the Moderate Resolution Imaging Spectroradiometer (MODIS) instrument and the VAISALA ceilometer, whose data is used in this work. To finish, in the last section of the 2nd chapter, a description of the case studies selected as well as the method followed in this research is made.

Chapter 3 shows the results of the applications of the methodologies developed to analyze the effects of Desert Dust (DD) aerosols upon the clouds developing in the presence as well as in the absence of DD aerosols. The confirmation of the presence of DD in the days chosen to this study is presented in the first part of the chapter. The following section deals with the comparisons carried out between the simulated results and independent VAISALA ceilometer retrievals. The results obtained for the vertical profiles of some of the aerosol and cloud properties and the direct radiative effects of DD aerosols for the days and regions under study are presented in the third section. In the two following sections, of the present chapter, the effect of DD aerosols upon cloud properties is presented as well as the indirect radiative forcing due to DD aerosols. Finally, the sixth and last section of chapter 3 presents the comparison between aerosols and cloud properties, simulated with MesoNH model, with the same quantities obtained from the MODIS aerosol and cloud products.

The thesis concludes with a summary of the main results regarding the mineral dust aerosols and cloud properties, the direct and indirect radiative forcings due to DD aerosols. Furthermore, a discussion on the possible work to be developed in future investigations is presented.

2. Tools, Data and Method

This chapter presents the tools used, as well as the methodology of the research work developed. It is divided in four sections, the first one dedicated to the general description of the meteorological model MesoNH, and concerning the radiative forcing due to aerosols and clouds. The second and third sections deal with the description of two instruments whose data is used along the work: the Moderate Resolution Imaging Spectroradiometer (MODIS) onboard Terra and Aqua satellites and a ceilometer installed in the Évora Geophysics Centre Observatory, in Évora. As a final point, the last section of this chapter describes the case studies selected for this work as well as the method followed to prepare and compare the simulated results.

The first section deals with the mesoscale non-hydrostatic MesoNH model, including the description of the surface scheme used in MesoNH. The following subsection explains the radiative transfer scheme within MesoNH and with the physical properties of aerosols and clouds, relevant in the radiative processes. In the following part, a brief description of the atmospheric radiative transfer theory is given, including its interaction with the atmospheric constituents (responsible for the absorption, emission and scattering processes in the atmosphere) and with the Earth's surface. The radiative transfer equation presented is limited to the complexity required by the present work, considering that the maximum generality possible in the mathematical formalism would be out of the scope here. Moreover, in the following subsection, considerations regarding the treatment of Desert Dust aerosols in MesoNH are presented. The MesoNH model allows to study the full cycle of the mineral desert dust aerosols and to estimate their impacts on the radiative balance. The representations of cloud particles, species taken into account and distribution laws that describe them in MesoNH, are then discussed.

The following two sections are dedicated the MODIS instrument and the VAISALA Ceilometer data used, respectively.

Finally, in the next section the selected and studied days in this work are presented. Also, in this last section, the assumptions taken regarding the simulations are explained as well as the method to compare the simulated data with MODIS and VAISALA data and, lastly, the method to assess the aerosol and cloud radiative forcing is presented.

2.1 The MesoNH atmospheric simulation system

The MesoNH model is the non-hydrostatic (NH) mesoscale (Meso) atmospheric model of the French research community. It has been jointly developed by the CNRM (Météo-France and Centre National de la Recherche Scientifique) and Laboratoire d'Aérologie (Centre National de la Recherche Scientifique and Université de Toulouse) (Lafore et al., 1998). MesoNH is able to simulate dynamical and physical processes, in the atmosphere, from small scale atmospheric circulations (horizontal resolution of a few meters) to synoptic scale (horizontal resolution of several tens of kilometers).

This atmospheric model uses a set of equations based on the anelastic formulation (Lipps and Hemler,1982 ; Wilhelmson and Ogura,1972 and Durran, 1989).

In this approach, the acoustic waves are removed from the set of continuous equations by the use of a constant density profile instead of the actual fluid density in the continuity equation and in the momentum equations, except in the buoyancy terms. The fluid becomes thus formally incompressible, and the pressure is deduced from the solution of an elliptic equation. All anelastic approach systems are based on the supposition that the atmosphere will not depart very far from a "reference state", defined as an atmosphere at rest, in hydrostatic equilibrium, with horizontally uniform profiles of temperature and water vapor. No condensed water is considered in the reference state. The reference profiles are often chosen as the initial horizontal averages of actual fields over the expected domain of simulation. Any profile, however, may be used, but the inaccuracy of the computation increases if the reference state is far from the actual mean state. The perturbations are resolved by the resolution of the model equation system. Numerically, this equation system is solved by discretization on an independent way and in the three directions of the coordinate system. Taking into account the Earth’s spherical form (roughly), the coordinate system can’t be Cartesian, so, for meteorological studies, the coordinate system is defined by latitude, longitude and altitude (Z) above sea level.

The model’s vertical coordinate ($\overline{Z}$) is the classic coordinate of Gal-Chen at Summerville (1975) defined by:

$$\overline{Z} = \frac{Z - Z_S}{H - Z_S} \tag{2.1}$$

where H is the model top heigth, Z_S the surface altitude in each considered geographical position and Z is the altitude above the sea level.

Therefore, in the atmospheric low level layers, the isolines of this vertical coordinate acquire the surface form and, as the altitude in the atmosphere increases, these isolines have the propensity to become horizontal.

For the spatial discretization, a grid based on the formulation of Messinger and Arakawa (1976) is used, and the temporal discretization scheme is an explicit leapfrog scheme with a time filter (Asselin, 1972) in order to control the rapid oscillations produced by the iterations.

The model's prognostic variables are the three-dimensional wind components, the potential temperature, the turbulent kinetic energy, and the mixing ratios of water vapour and of several classes of hydrometeors (water vapour, cloud water, liquid water, ice, snow, and graupel).

The horizontal resolution is able to vary between the hundreds of kilometers to a few meters in order to answer to the scale constraints of the studied phenomena. To avoid long time calculations, fine resolutions can be obtained using the grid nesting technique (Clark, 1984; Stein et al., 2000). Figure 2.1 illustrates this technique.

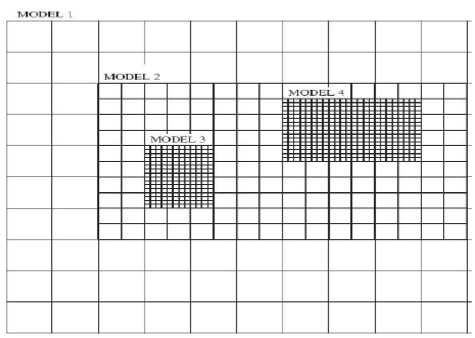

Figure 2.1 Nested models with different resolutions.

The grid nesting technique allows focusing on specific regions described by a higher spatial resolution, maintaining a correct representation of large scale flow with a moderate size memory occupation and greater computational efficiency. More than two models can be used together. The nesting is restricted to horizontal directions. The temporal and horizontal spatial resolution ratios between the fine grid (child) model and its coarse grid (parent) must be integer.

The model needs to be initialized and coupled. At the beginning of the simulation, all model prognostic variables are initialized for all the meshes of the model. The atmosphere is regarded as chaotic and small changes in initial conditions can lead to large variations in the final state. The initialization must be done carefully since the outcome results depend on this initialization and, therefore, the quality of the simulation. During the simulation, the use of coupling is made in order to provide data at the lateral limits of the model simulations with open boundary conditions.

The model boundary conditions can be real or artificial. They may be cyclic or rigid (with mass conservation) or open (where the mass is not conserved). The lateral and upper limits of the model are the artificial limits related to the non-global nature of the model. The lower limit is a real limit (the surface), therefore it is necessary to take into account the surface – atmosphere interactions. The conditions for lower and upper limits, despite their different natures, are of the rigid type. The normal velocities are zero at the boundaries and other variables are symmetric there. The last simulated layers on the top of the model are considered purely absorbing layers, in order to avoid unwanted wave reflections. The lateral boundary conditions can be of any type, but are generally open for the study of real cases. For open boundary conditions, the incoming conditions are given by the coupling files. The outgoing conditions are the model prognostic values.

Initialization and coupling of real cases are generally made for the 'father' model (see Figure 2.1), from analyses or forecasts of a large scale global model system, namely from the analysis of the European Center for Medium-range Weather Forecasts (ECMWF). These analyses are interpolated or averaged over the model grid. In the case of nested models, the 'son' model simulations are initialized and coupled from the 'father' model through a set of functions that allow for preparing the initial states. Due to the absence of cloud analysis by the operational models, the departure of the Meso-NH model is always made in conditions of clear sky, which imposes a spin-up time corresponding at the time for cloud formation by the model.

Despite all the filtrations, discontinuities and uncertainties associated to the domain, boundaries have an influence on the mesh along the modeling domain. It is essential to have a domain large enough in order to ensure that all domain boundaries are far from the zone of interest, avoiding then their interference to the maximum.

Parameterizations have been introduced for convection (Bechtold et al., 2001), cloud microphysics (Pinty and Jabouille, 1998; Cohard and Pinty, 2000; Geoffroy, 2007), turbulence (Bougeault and Lacarrere, 1989; Cuxart et al., 2000), biosphere–atmosphere thermodynamic exchanges (ISBA) (Noilhan and Mahfouf, 1996), urban–atmosphere interactions (Masson, 2000), lake-atmosphere interactions (Salgado and Le Moigne, 2010), lightning processes (Barthe et al., 2005), gaseous chemistry (Suhre et al., 1998; Tulet et al., 2003) and aerosol chemistry (Tulet et al., 2006).

Among all the MesoNH physical parameterizations mentioned above, only the parameterizations essential to this work will be described in the following subsections, namely: the surface scheme, the radiation scheme, the treatment of mineral aerosol emissions and of cloud microphysics in the model.

2.1.1 The surface scheme SurfEx

The Meso-NH atmospheric model is coupled to an externalized surface model (SurfEx) which simulates the fluxes between the atmosphere and the surface.

In SurfEx, the exchanges between the surface and the atmosphere are made by means of a standardized interface (Polcher 1998; Best et al., 2004) that offers a generalized two-way coupling between the atmosphere and the surface.

For a model time step period, each surface grid-box receives the upper air temperature, specific humidity, horizontal wind components, pressure, total precipitation, long-wave, as well as shortwave direct and diffuse radiation and also, if selected, concentrations of chemical species and dust. On the other hand, SurfEx computes averaged fluxes for momentum, sensible and latent heats and, if selected, chemical species and dust fluxes. These quantities are then sent back to the atmosphere with the addition of a radiative surface temperature, surface direct and diffuse albedo and also the surface emissivity. All this information, mentioned before, is used as lower boundary conditions for the atmospheric radiation and turbulent schemes. One of the ideas of SurfEx is to split each model grid-box into fractions of sea, lake urban and natural areas. The coverage of each of these surfaces is known through the global ECOCLIMAP database (Masson et al., 2003), which combines land cover maps and satellite information. Each surface type is simulated with a specific surface model (ISBA for natural areas, TEB for urban areas, FLake or Watflx for lakes and Watflx for seas) and the total flux of grid box results from the addition of the individual fluxes weighted by their respective fraction.

In order to be used in several operational atmospheric models, the ISBA land surface scheme has been designed to be simple and efficient. ISBA computes the exchanges of energy and water between the continuum soil-vegetation-snow and the atmosphere above. At the present time, the ISBA scheme is used in the French operational and research forecast models.

The TEB model is based on the canyon concept (Oke 1987), where a town is represented with a roof, a road and two facing walls with characteristics playing a key role in the town energy budget. More especially, the ability of the canyon to trap a fraction of the incoming solar and infrared radiation is taken into account by the model.

The representation of water surfaces has also been improved. There are two possibilities to compute fluxes over marine surfaces. The simplest one consists of using Charnock's approach to compute the roughness length and fluxes with the simulation period. Secondly, a one-dimensional ocean mixing layer model has been introduced in order to simulate more accurately the time evolution of the sea surface temperature and the fluxes at the sea-air interface. This model based on Gaspar (1990), helps to represent the diurnal cycle of sea-surface temperature (Lebeaupin 2006) especially at the mesoscale modeling. An improved restitution of lake surface temperature and consequently of the associated surface fluxes is made through the use of the FLake model (Mironov, 2008) inserted in the SurfEx system by Salgado and Le Moigne (2010). The FLake model parameterizes the local-scale energy exchanges between lake surfaces and the atmosphere, simulating the temperature profile as well as the budgets of heat and turbulent kinetic energy in water.

In the present work, the emissions of dust aerosols are calculated directly from the surface parameters of ISBA and the atmospheric variables at the first Meso-NH level, and then sent to the atmosphere consistently with the fluxes of momentum, energy and humidity. A more detailed description about dust aerosols emissions is given in section 2.1.3.

2.1.2 The radiative transfer within MesoNH

Radiative transfer describes the transfer of electromagnetic energy in the atmosphere. The transfer of solar (shortwave) and terrestrial (longwave) radiation through the atmosphere influences all aspects of the climate system. For a significant portion of the earth's surface the radiation budget is the dominant term in the surface energy balance. Understanding how radiation is attenuated by clouds, aerosols, and gases as it passes through the atmosphere is therefore a prerequisite to understand the dynamic and thermodynamic components of the global climate system.

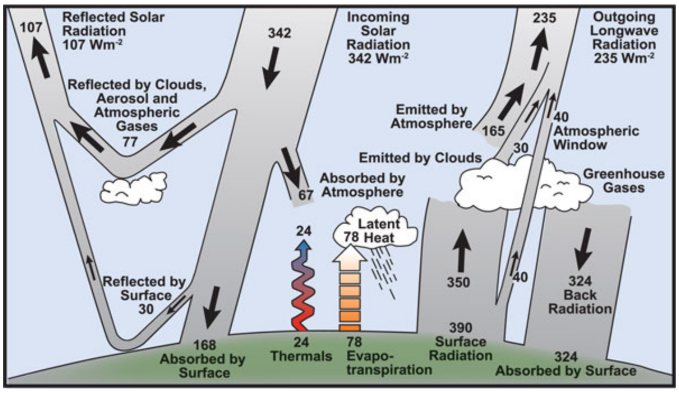

Figure 2.2 Estimate of the Earth's annual and global mean energy balance. Source: Kiehl and Trenberth (1997).

According to Figure 2.2 and over the long term, the amount of incoming solar radiation absorbed by the Earth and atmosphere is balanced by the outgoing longwave radiation emitted by the Earth and atmosphere at the top of the atmosphere. About half of the incoming solar radiation is absorbed by the Earth's surface. This energy is transferred to the atmosphere by warming the air in contact with the surface (sensible heat flux), by evapotranspiration (latent heat flux) and by longwave radiation that is absorbed by clouds and greenhouse gases. The atmosphere in turn radiates longwave energy back to Earth as well as out to space.

2.1.2.1 Aerosol and Cloud Radiative Properties

Several changes, especially reductions, in solar radiation at the surface and at the TOA levels, have been reported by numerous studies (Stanhill and Cohen, 2001; Liepert, 2002; Ramanathan et al., 2005). The sources of these changes are attributed to changes in aerosols, clouds or both. Field studies have revealed that aerosols by themselves can lead to changes as large as those observed.

Aerosol-cloud interactions can contribute to additional large-scale changes in the surface solar radiation (e.g., Kaufman et al., 2005). Moreover, the presence of clouds can significantly change the radiative impact of aerosols (Liao and Seinfeld, 1998a; Haywood and Ramaswamy, 1998; Myhre et al., 2003). Therefore, understanding the role of aerosols / clouds in solar radiation is crucial to understand the observed changes in solar radiation.

In order to characterize aerosols, it is necessary to know their microphysical and chemical composition (e. g. shapes, dimensions) and states of mixtures and the total quantity in the atmospheric column). The three first parameters may be achieved through the aerosol optical properties and a scattering theory. The aerosol optical properties can be measured or derived from various techniques namely from remote sensing. The aerosol remote sensing is based on the effect that these particles have in the scattering and transmission of radiation in the Earth's atmosphere and, consequently, is based on aerosols radiative/optical quantities (Lenoble, 1993). These quantities, for a given wavelength (λ), include the volume scattering coefficient (β_λ^s), the volume absorption coefficient (β_λ^a), the phase function $(P_\lambda(\Theta))$, where Θ is known as the scattering angle formed between the directions of the incident and scattering radiation. The volume extinction coefficient (β_λ^e) can be obtained summing the volume scattering coefficient with the volume absorption coefficient. The ratio between the volume scattering coefficient and the volume extinction coefficient is the single scattering albedo (ϖ_λ).

The phase function and the extinction, scattering and absorption coefficients depend on the particle shape, composition and dimension. The refractive index (m_λ), which is related to the aerosol chemical composition and their state of mixture, is given by:

$$m_\lambda = m_{r_\lambda} - i m_{i_\lambda} \tag{2.2}$$

If the particles are non-absorbing, then $m_\lambda = m_{r_\lambda}$, meaning that the refractive index is only real. If the particles absorb radiation, m_λ is complex and the imaginary part, m_{i_λ}, is directly related to the absorption in the following way:

$$m_{i_\lambda} = \frac{\lambda \beta_\lambda^a}{4\pi} \tag{2.3}$$

In this work, it is considered that all the particles in the atmosphere behave as spherical particles, being then appropriate the use of the Mie theory. A more detailed description of Mie theory may be found in literature, such as Liou (1980). The results of Mie theory can be used for a homogeneous sphere with a size parameter, the radius r. However, in the atmosphere, one cannot find only one particle but several ones. It is assumed then that the scattering particles are sufficiently away, one from the others, and that distance is much larger than the incident radiation wavelength, becoming then possible the study of the scattering processes for each one of these particles without the influence of the other particles (this phenomenon is known as independent scattering), being then possible to apply the Mie theory.

Considering all the assumptions made previously, and considering a particle sample with size described by the size distribution function $n(r)dr$, the volume extinction, scattering and absorption coefficients are given, respectively, by:

$$\beta_\lambda^e(m) = \int_{R_{\min}}^{R_{\max}} \pi r^2 Q_\lambda^e(r,m)\, n(r)\, dr \tag{2.4}$$

$$\beta_\lambda^s(m) = \int_{R_{\min}}^{R_{\max}} \pi r^2 Q_\lambda^s(r,m)\, n(r)\, dr \tag{2.5}$$

$$\beta_\lambda^a(m) = \int_{R_{\min}}^{R_{\max}} \pi r^2 Q_\lambda^a(r,m)\, n(r)\, dr \tag{2.6}$$

where Q_λ^e, Q_λ^s and Q_λ^a are, respectively, the Mie extinction, scattering and absorption efficiencies defined by:

$$Q_\lambda^e(r,m) = \frac{2}{\chi^2}\sum_{n=1}^{\infty}(2n+1)\,\mathrm{Re}(a_n + b_n) \tag{2.7}$$

$$Q_\lambda^s(r,m) = \frac{2}{\chi^2}\sum_{n=1}^{\infty}(2n+1)(|a_n|^2 + |b_n|^2) \tag{2.8}$$

and

$$Q_\lambda^a(r,m) = Q_\lambda^e(r,m) - Q_\lambda^s(r,m) \tag{2.9}$$

where Re represents the real part and a_n and b_n are the Mie coefficients. χ is the Mie size parameter given by:

$$\chi = \frac{2\pi r}{\lambda} \tag{2.10}$$

where r is the radius of the spherical particle and λ the radiation wavelength.

The single scattering albedo can be defined as the ratio between the volume scattering coefficient β_λ^s and the volume extinction (scattering plus absorption) coefficient β_λ^e.

$$\varpi_\lambda = \frac{\beta_\lambda^s}{\beta_\lambda^e} \tag{2.11}$$

For pure scattering aerosols, ϖ_λ is equal to unity and for pure absorbing aerosols the single scattering albedo would be null.

The particle influence on extinction is weighted through the geometrical cross section πr^2 . The size distribution $n(r)$ of a sample of *N* particles represents the particle distribution in the atmosphere. The phase function, of the sample of particles, described by the size distribution function $n(r)$, can be expressed by:

$$P_\lambda(m,\Theta) = \int_{R_{\min}}^{R_{\max}} \frac{\lambda^2}{2\pi\,\sigma_\lambda^d(r,m)} (|S_1|^2 + |S_2|^2)\, n(r)\, dr \tag{2.12}$$

where $S_1(\chi,m,\Theta)$ and $S_2(\chi,m,\Theta)$ are complex functions defined through Maxwell's equations, related to the amplitude of the scattered radiation perpendicular and parallel to the scattering plane, respectively, and $\sigma_\lambda^s(r,m)$ is the scattering cross section of a spherical aerosol , which can be defined as:

$$\sigma_\lambda^s(r,m) = \pi r^2\, Q_\lambda^s(r,m) \tag{2.13}$$

The phase function is normalized, meaning that its integral over a sphere of unit radius centered on the spherical aerosol is given by:

$$\int_0^{2\pi}\int_0^{\pi} P_\lambda(\Theta,m) \sin\Theta\, d\Theta\, d\phi = 4\pi \tag{2.14}$$

The total spectral aerosol optical depth normal to the atmosphere τ_λ can be defined through the following equation:

$$\tau_\lambda = \int_{z=0}^{\infty} k_\lambda^e(z)\,\rho\, dz = \int_{z=0}^{\infty} \beta_\lambda^e(z)\, dz = \int_{z_1}^{z_2}\int_{r_{\min}}^{r_{\max}} (\pi r^2 Q_{ext}(\lambda, N(r), m_\lambda, shape) dN(r) dr) dz \tag{2.15}$$

where the volume extinction coefficient (β_λ^e) can be related with the aerosol mass extinction cross section, k_λ^e and the aerosol density ρ.

Considering $n(r)$ the particle size distribution r the particle radius, it is very useful, sometimes, to use the effective radius r_{eff}, which can be defined as the ratio of the total volume to the total surface area of the particles:

$$r_{eff} = \frac{\int_0^\infty r^3\, n(r)\, dr}{\int_0^\infty r^2\, n(r)\, dr} \tag{2.16}$$

and its associated variance υ_{eff}, which can be expressed in terms of the size distribution parameters as:

$$\upsilon_{eff} = \frac{\int_0^\infty \left(r - r_{eff}\right)^2 r^2\, n(r)\, dr}{r_{eff}^2 \int_0^\infty r^2\, n(r)\, dr} \tag{2.17}$$

Considering now the particular case of water clouds, the liquid water path (LWP) can be obtained from the definition of the vertically integrated liquid water content (LWC), for the spherical particles, as:

$$LWP = \int_{z_1}^{z_2} LWC\, dz \tag{2.18}$$

where

$$LWC = \frac{4\pi}{3} \rho_l \int_0^\infty r^3\, n(r)\, dr \tag{2.19}$$

where ρ_l is the liquid water density.

The effective radius can be related with the LWP through the following equation:

$$LWP = \frac{2}{3} \tau_\lambda\, r_{eff} \tag{2.20}$$

According to Brenguier et al. (2011), in liquid water clouds the cloud optical depth can be related to the liquid content and effective radius (Hansen and Travis, 1974; Stephens, 1978) via:

$$COD = \int_{z=0}^{h} \frac{3\,LWC}{2\pi\rho_l r_{eff}} dz\,. \tag{2.21}$$

The spectral variation of the aerosol optical thickness is often approximated by the Angström power law:

$$\tau_\lambda = \beta\,\lambda^{-\alpha} \tag{2.22}$$

where β is the Angström turbidity coefficient and α the Angström exponent, related to the particle size (decreases when the particle size increases). The Angström exponent can be obtained from the aerosol optical thickness at two wavelengths (λ_1 and λ_2):

$$\alpha = \frac{\log\left(\frac{\tau_1}{\tau_2}\right)}{\log\left(\frac{\lambda_1}{\lambda_2}\right)} \tag{2.23}$$

2.1.2.2 The radiative transfer in the atmosphere

Assuming an atmospheric layer, with density ρ, and characterized by a mass extinction cross section, k_λ^e, the intensity of radiation, I_λ or monochromatic radiation, after traversing a thickness ds in the direction of its propagation, becomes $I_\lambda + dI_\lambda$, for radiation of wavelength λ. According to the previous assumptions it can be assumed that:

$$dI_\lambda = -I_\lambda k_\lambda^e \rho\, ds \tag{2.24}$$

The spectral mass extinction cross section k_λ^e (m^2/kg) is given by the sum of the spectral mass absorption (k_λ^a) and scattering (k_λ^d) cross sections:

$$k_\lambda^e = k_\lambda^a + k_\lambda^d \tag{2.25}$$

This reduction in intensity is due to atmospheric constituents such as aerosols, clouds and gases, therefore the spectral mass extinction cross section k_λ^e is the sum of the spectral mass extinction cross sections due to aerosols, a, clouds, c and gases, g

$k_\lambda^e = k_{\lambda a}^e + k_{\lambda c}^e + k_{\lambda g}^e$. In equation 2.24, $-I_\lambda$ corresponds to the sink function and represents the attenuated radiation caused by the absorption and single scattering processes, along the direction of propagation.

On the other hand, the intensity of radiation may be strengthened in the same direction of propagation by atmospheric emission plus multiple scattering coming from all other directions. This increase in the intensity of radiation may be given by:

$$dI_\lambda = J_\lambda k_\lambda^e \rho\, ds \tag{2.26}$$

where J_λ is known as the source function and represents the contributions of emission, single scattering and multiple scattering for the increase of the radiation beam along the incident direction of propagation.

Combining equations 2.24 and 2.26, the following equation for an absorbing/emitting and scattering atmospheric layer of thickness *ds* is obtained:

$$dI_\lambda = -I_\lambda k_\lambda^e \rho\, ds + J_\lambda k_\lambda^e \rho\, ds \tag{2.27}$$

Equation 2.27 can also be written as:

$$\frac{dI_\lambda}{k_\lambda^e \rho\, ds} = -I_\lambda + J_\lambda \tag{2.28}$$

where in a spherical coordinated system, the source and sink functions of equation 2.28 can be expressed as:

$$\frac{dI_\lambda(s;\theta,\phi)}{k_\lambda^e \rho\, ds} = -I_\lambda(s;\theta,\phi) + J_\lambda(s;\theta,\phi) \tag{2.29}$$

being $I_\lambda(s;\theta,\phi)$ the monochromatic radiance, in units of energy per time, wavelength and solid angle ($Wm^{-2}m\mu^{-1}sr^{-1}$), that emerges from the level *s of* a layer with thickness *ds* in the direction of the propagation beam, which subtends an angle θ , called zenithal angle, with the normal to the layer and whose horizontal projection forms an angle ϕ with the southern direction, called azimuthal angle.

Equation 2.29 may be re-written in terms of the altitude variable z , normal to the atmospheric layer, instead of the slant path s , where $dz = \cos\theta\, ds = \mu\, ds$:

$$\mu \frac{dI_\lambda(z;\mu,\phi)}{k_\lambda^e \rho\, dz} = -I_\lambda(z;\mu,\phi) + J_\lambda(z;\mu,\phi) \tag{2.30}$$

The normal optical thickness of the atmospheric thickness *dz* can be defined through the following equation:

$$d\tau = -k_\lambda^e(z)\rho\, dz = -\beta_\lambda^e(z) dz \tag{2.31}$$

where $\beta_\lambda^e(z)$ is the volume extinction coefficient, expressed in units of area per volume (m^{-1}) which changes with the altitude *z*. If this quantity only refers to the extinction due to aerosols it can be related to the spectral extinction cross section, σ_λ^e in units of area (m^2) and with the total concentration of particles, N in units of particles per volume unit (m^{-3}) leading to the following equation:

$$d\tau = -\sigma_\lambda^e N\, dz \tag{2.32}$$

where *N* can be calculated from the aerosol size spectra *n(r)* by the following equation:

$$N(r) = \int_{r_{\min}}^{r_{\max}} n(r) dr \tag{2.33}$$

and $n(r)dr$ represents the number of particles with a radius between *r* and *r+dr.*

Introducing $d\tau_\lambda$, given by equation 2.33, in equation 2.30, it becomes:

$$\mu \frac{dI_\lambda(\tau;\mu,\phi)}{d\tau} = I_\lambda(\tau;\mu,\phi) - J_\lambda(\tau;\mu,\phi) \tag{2.34}$$

that constitutes the general equation for the radiative transfer in plane parallel atmospheres, which can, at the same time, absorb, scatter and emit radiation.

In the discussion of the radiative transfer, it is commonly assumed, in localized portions, the atmosphere as being plane and parallel (see Figure 2.3). This assumption implies that variations in the intensity and atmospheric parameters are permitted only in the vertical direction (e. g., height or pressure).

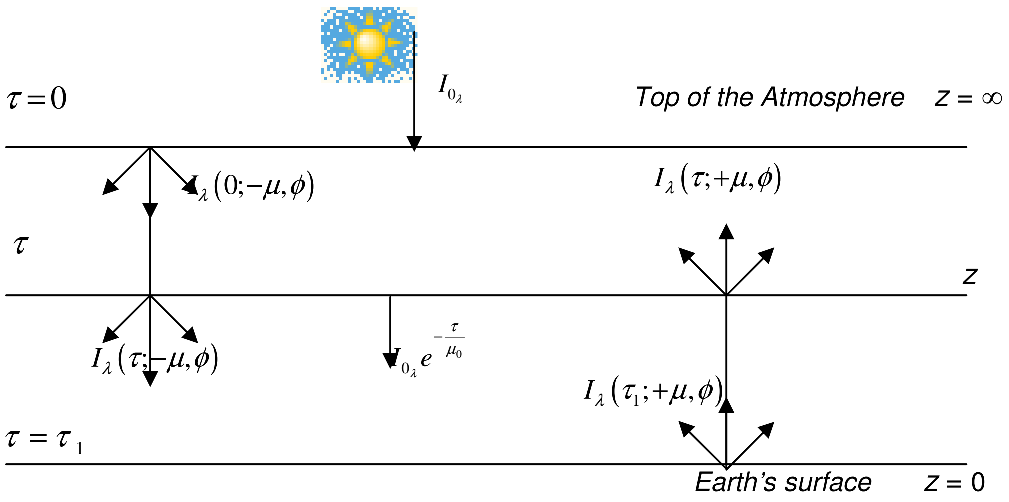

Figure 2.3 Upwelling and downwelling radiation fluxes crossing a finite plane-parallel atmospheric layer. Source: Liou, 1980.

Considering now an absorbing, scattering and emitting atmosphere bounded at the bottom with $\tau = \tau_1$ and at the top with $\tau = 0$, as shown in Figure 2.3, the formal solutions of equation 2.34 are for the upward radiance $I_\lambda^{\uparrow} \equiv I_\lambda(\tau;+\mu,\phi)$:

$$I_\lambda(\tau;+\mu,\phi) \equiv I_\lambda^{\uparrow} = I_\lambda(\tau_1;+\mu,\phi)e^{-\frac{\tau_1-\tau}{\mu}} + \int_\tau^{\tau_1} J_\lambda(\tau';+\mu,\phi)e^{-\frac{\tau'-\tau}{\mu}}\frac{d\tau'}{\mu} \tag{2.35}$$

and for the downward radiance $I_\lambda^{\downarrow} \equiv I_\lambda(\tau;-\mu,\phi)$:

$$I_\lambda(\tau_1;-\mu,\varphi) \equiv I_\lambda^{\downarrow} = I_\lambda(0;-\mu,\phi)e^{-\frac{\tau}{\mu}} + \int_0^{\tau_1} J_\lambda(\tau';-\mu,\varphi)e^{-\frac{\tau_1-\tau'}{\mu}}\frac{d\tau'}{\mu} + I_{0_\lambda} e^{-\frac{\tau}{\mu_0}} \tag{2.36}$$

crossing an atmospheric layer τ . I_{0_λ} is the direct solar radiance at the TOA and $\mu_0 = \cos\theta_0$ where θ_0 is the solar zenith angle.

The term $I_{0_\lambda} e^{-\frac{\tau}{\mu_0}}$, in equation 2.36 represents the attenuation that the direct solar radiance suffers when it crosses the considered atmospheric layer.

Considering a negative sign for the downward direction ($\mu_0 < 0$) the first terms of the right hand side, of equations 2.35 and 2.36, represent, respectively, the monochromatic radiance that leaves the surface, and is attenuated by the atmosphere until it reaches level τ , and the diffuse monochromatic radiance that emerges from the top of the atmosphere and is attenuated until it reaches level τ , which can be neglected.

The monochromatic intensity at the surface (diffuse + direct), considering there is no downward emitted diffuse radiance at the top of the atmosphere ($I_\lambda(0;-\mu,\phi)=0$), is given by:

$$I_\lambda(\tau_1;-\mu,\phi) \equiv I_\lambda^{\downarrow} = \int_0^{\tau_1} J_\lambda(\tau';-\mu,\phi)e^{-\frac{\tau_1-\tau'}{\mu}}\frac{d\tau'}{\mu} + I_{0_\lambda}e^{-\frac{\tau}{\mu_0}} \tag{2.37}$$

and, the upward monochromatic intensity that reaches the top of the atmosphere is:

$$I_\lambda(0;+\mu,\phi) \equiv I_\lambda^{\uparrow} = I_\lambda(\tau_1;+\mu,\phi)e^{-\frac{\tau_1}{\mu}} + \int_0^{\tau_1} J_\lambda(\tau';+\mu,\phi)e^{-\frac{\tau'}{\mu}}\frac{d\tau'}{\mu} \tag{2.38}$$

In equation 2.37, the first term on the right hand side represents the upward diffuse radiance, originating in the Earth's surface, attenuated by the atmosphere. The integral terms of equations 2.36 and 2.37 represent the intern contributions of the atmosphere.

Taking into account the emission and scattering physical processes the source function may be given by:

$$\begin{aligned} J_\lambda(\tau;\mu,\phi) &= \frac{\varpi_\lambda}{4\pi}F_{0_\lambda}P_\lambda(\mu,\phi;-\mu_0,\phi_0)e^{-\frac{\tau}{\mu_0}} + \\ &+ \frac{\varpi_\lambda}{4\pi}\int_0^{2\pi}\int_{-1}^{1} I_\lambda(\tau;\mu',\phi')P_\lambda(\mu,\phi;\mu',\phi')d\mu'\,d\phi' + (1-\varpi_\lambda)B_\lambda(T) \end{aligned} \tag{2.39}$$

where the first term represents the contribution of the diffuse intensity scattered out of the incident direct solar flux density $\left(F_{0_\lambda}\right)$ coming from the direction $(-\mu_0,\varphi_0)$ into the emerging direction (μ,ϕ), due to single scattering. The second term corresponds to the radiation that suffers the scattering process more than once (multiple scattering), coming from the (μ',ϕ') direction into the emerging (μ,ϕ) direction. The third term of equation 2.39, $B_\lambda(T)$, is the Planck function that relates the emitted monochromatic intensity with the wavelength and the absolute temperature of the emitting material (Earth's surface or atmosphere that can be considered to have a blackbody's behaviour). $P_\lambda(\mu,\phi;\mu',\phi')$ is the scattering phase function (equation 2.12) which describes the probability of a particle to scatter radiation, coming from the direction (μ',ϕ') into the (μ,ϕ) direction, as a function of the wavelength. ϖ_λ is the single scattering albedo (see above equation 2.48) that gives the amount of scattered radiation, with respect to the radiation that suffers extinction (scattering plus absorption), when single scattering is considered.

The solar and terrestrial radiation spectra are generally considered to be separated at the wavelength of 4.0 µm, with a small overlap in the surrounding regions. This separation gives the possibility of treating the radiative transfer of solar radiation independently of terrestrial (thermal IR) radiation since the dominant physical processes resulting from the interaction with the atmospheric constituents (such as aerosols) differ in the two spectral regions.

In the infrared spectral region (λ> 4 µm), the dominant physical process is the absorption / emission of radiation, since scattering of radiation can be in good approximation neglected. The Planck function $B_\lambda(T)$, in units of energy per unit time, area, solid angle and wavelength, is given by:

$$B_\lambda(T) = \frac{2hc^2}{\lambda^5\left(e^{\frac{hc}{k\lambda T}} - 1\right)} \tag{2.40}$$

where h is the Planck constant ($h = 6.6262 \times 10^{-34}\, Js$), c is the speed of light in the vacuum ($c = 2.9979 \times 10^{8}\, ms^{-1}$) and k is the Boltzmann constant ($h = 1.3806 \times 10^{-23}\, JK^{-1}$).

Considering a non-scattering atmosphere ($\varpi = 0_\lambda$), where only absorption and emission processes occur and assuming local thermodynamic equilibrium, the source function (equation 2.39) becomes only the product of the Planck function by the emissivity of the atmosphere (ε_λ):

$$J_\lambda(\tau;\mu) = \varepsilon_\lambda B_\lambda(T) \tag{2.41}$$

Since a plane-parallel atmosphere is assumed, where only vertical variations of the physical properties are considered, the source function depends only on the height coordinate and on the zenith angle (Liou, 1992).

Considering that the Earth's surface and atmosphere may be assumed as blackbodies in the infrared spectral region ($\varepsilon_\lambda = 1$), the radiative transfer equation in a plane-parallel atmosphere (equation 2.34), for a medium where no scattering processes are considered, only absorption and emission processes occur becomes the Schwarzschild equation:

$$\mu \frac{dI_\lambda(\tau;\mu)}{d\tau} = I_\lambda(\tau;\mu) - B_\lambda(T) \qquad (2.42)$$

For this case, the general solution of the radiative transfer equation presented in equations 2.35 and 2.36, for an atmosphere, bounded at the bottom by $\tau = \tau_1$ and at the top by $\tau = 0$, where no emission is considered at the TOA ($\beta_\lambda\left(T_{(0)}\right) = 0$ so $\beta_\lambda\left(T_{(0)}\right) \cdot e^{-\frac{\tau}{\mu}} = 0$), the downward radiance becomes:

$$I_\lambda^\downarrow \equiv I_\lambda(\tau; -\mu) = \int_0^\tau B_\lambda\left(T_{(\tau')}\right) \cdot e^{-\frac{(\tau-\tau')}{\mu}} \frac{d\tau'}{\mu} \qquad (2.43)$$

and the upward radiance:

$$I_\lambda^\uparrow \equiv I_\lambda(\tau; +\mu) = B_\lambda\left(T_{(\tau_1)}\right) \cdot e^{-\frac{(\tau_1-\tau)}{\mu}} + \int_\tau^{\tau_1} B_\lambda\left(T_{(\tau')}\right) \cdot e^{-\frac{(\tau'-\tau)}{\mu}} \frac{d\tau'}{\mu} \qquad (2.44)$$

The first term on the right hand side of equation 2.44 represents the emission contribution of the Earth's surface attenuated by the atmosphere and the integral, in both equations (2.43 and 2.44), states for the emission contributions of each of the atmospheric layers.

Several computational methods exist to provide the numerical solution of the radiative transfer equation for the upward radiation (equation 2.35) and for the downward radiation (equation 2.36). The most common is the discrete ordinates method, which has been developed by Chandrasekhar (1950) and uses a discretization of the radiative transfer equation and the expansion of the phase function in a Legendre polynomial series approximation, supplying the analytical solutions of the diffuse intensity for any optical thickness (Lenoble, 1993). In the MesoNH model, for the shortwave, the estimation of the radiative fluxes is based on the Delta Eddington approximation (Joseph and Wiscombe, 1976), which assumes the separation of radiative fluxes in one part going upward and another one going downward (Fouquart and Bonnel, 1980). For the longwave radiation, two schemes are available: one based also on a method of splitting into two fluxes (upwelling and downwelling fluxes) and another one based on the methods of k-correlation (RRTM). Although RRTM method better represents the different windows of atmospheric absorption, it is computationally very expensive.

For radiation balance studies it is essential to define the total flux density ($F^{\uparrow\downarrow}$) in the upward or downward directions, expressed in units of energy per unit time and area:

$$F^{\uparrow\downarrow} = \int_0^\infty F_\lambda^{\uparrow\downarrow} d\lambda \tag{2.45}$$

Integrating the monochromatic radiance I_λ in the zenith and azimuth directions, the monochromatic flux density $F_\lambda^{\uparrow\downarrow}$ is obtained. The downward diffuse solar flux, yielding at the surface is given by:

$$F_\lambda^{\downarrow} = \int_0^{2\pi} \int_0^{+1} I_\lambda(-\mu,\phi) \cdot \mu \cdot d\mu \cdot d\phi + \mu_0 \cdot F_{0_\lambda} \cdot e^{-\frac{\tau_1}{\mu_0}} \tag{2.46}$$

and the upwelling diffuse solar flux at the TOA:

$$F_\lambda^{\uparrow} = \int_0^{2\pi} \int_0^{+1} I_\lambda(+\mu,\phi) \cdot \mu \cdot d\mu \cdot d\phi \tag{2.47}$$

The radiation balance at a given level is denoted by the net radiation and can be written:

$$F^{net} = F^{\downarrow} - F^{\uparrow} \tag{2.48}$$

It is sometimes convenient to introduce the separation between the shortwave (SW) and the longwave (LW) radiation:

$$F^{\uparrow\downarrow} = F_{SW}^{\uparrow\downarrow} + F_{LW}^{\uparrow\downarrow} \tag{2.49}$$

and consequently:

$$F^{net} = F_{SW}^{\downarrow} - F_{SW}^{\uparrow} + F_{LW}^{\downarrow} - F_{LW}^{\uparrow} \tag{2.50}$$

2.1.2.3 Radiative Forcing

The Earth-atmosphere system can be considered in radiative equilibrium, on a long term basis and for the entire Globe, since the emitted infrared radiation compensates the incoming absorbed solar radiation by the Earth-Atmosphere. Small changes in the solar or terrestrial radiation due to natural or man induced changes in the atmosphere and or at the surface radiative properties might lead to variations in the global radiative equilibrium and consequently in the global climate.

The influence of a factor that may cause climate change is often evaluated in terms of its radiative forcing. Radiative forcing is defined here as a (momentary) change of the energy balance at some reference level. The word radiative comes up because the different factors (atmospheric aerosols, gases, clouds and surface changes) are responsible for perturbing the balance between incoming solar radiation and the outgoing infrared radiation in the climate system. This radiative balance controls the Earth's surface temperature. The expression forcing is used to point out that Earth's radiative balance is being pushed away from its normal state.

Ramaswamy et al. (2001) and the IPCC fourth assessment reports (e. g. IPCC, 2007) define radiative forcing as 'the change in net (downward minus upward) irradiance (solar plus longwave, in Wm^{-2}) at the tropopause after allowing for stratospheric temperatures to readjust to radiative equilibrium, but with surface and tropospheric temperatures and state held fixed at the unperturbed values'. Radiative forcing is used to evaluate and compare the anthropogenic and natural drivers of climate change. Radiative forcing is generally quantified as the rate of energy change per unit area of the globe as measured at the top of the atmosphere, and is expressed in units of 'Watts per square meter' (see Figure 2.4). When radiative forcing due to a factor or a group of factors is estimated as positive, the energy of the Earth-atmosphere system will ultimately increase, leading to a warming of the system. In contrast, for a negative radiative forcing, the net energy will eventually decrease, leading to a cooling of the system. Fundamental challenges for the climate scientists are: i) to identify all the factors that influence climate and the mechanisms by which they exert a forcing; ii) to quantify the radiative forcing of each factor and to assess the total radiative forcing from the group of factors. The contributions to radiative forcing from some of the factors influenced by human activities are shown in Figure 2.4. The uncertainties affecting each of the contributions are also indicated by horizontal bars. The RF values reproduce the total forcing related to the beginning of the industrial era (about 1750). The radiative forcings for all greenhouse gases are positive since each gas absorbs part of the outgoing infrared radiation emitted by the Earth-atmosphere system. Among the greenhouse gases, CO_2 increase has caused the largest forcing over this period. The increase of tropospheric ozone has also contributed to warming the Earth-atmosphere system, whereas the decrease of stratospheric ozone has contributed to the cooling of this system.

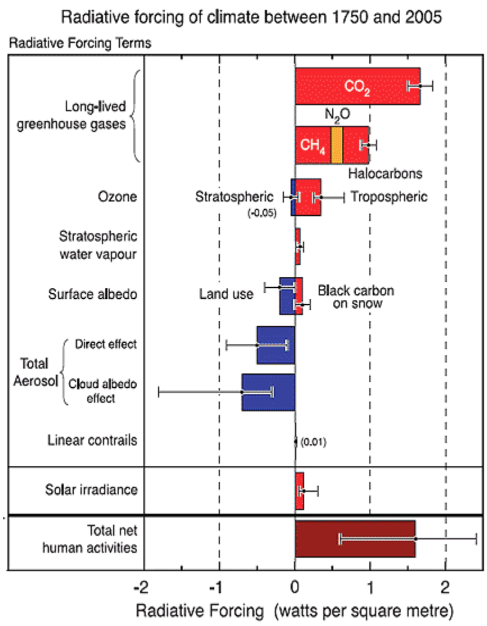

Figure 2.4 Summary of the principal components of the radiative forcing of climate change.(Source: Forster et al., 2007)

Aerosol particles directly influence radiative forcing through scattering and absorption of solar and infrared radiation in the atmosphere. Various aerosols cause a negative forcing, while others cause a positive forcing. Considering all aerosol types, the total direct radiative forcing is negative. In addition, aerosols cause a negative radiative forcing indirectly throughout the modifications that they cause in cloud properties, some of these illustrated in the Figure 2.4.

Assuming that the several factors influenced by human activities and contributing to the radiative forcing act independently, which is not necessarily true, the total net radiative forcing due to all of them is the sum of all the partial radiative forcings. This is also illustrated in Figure 2.5.

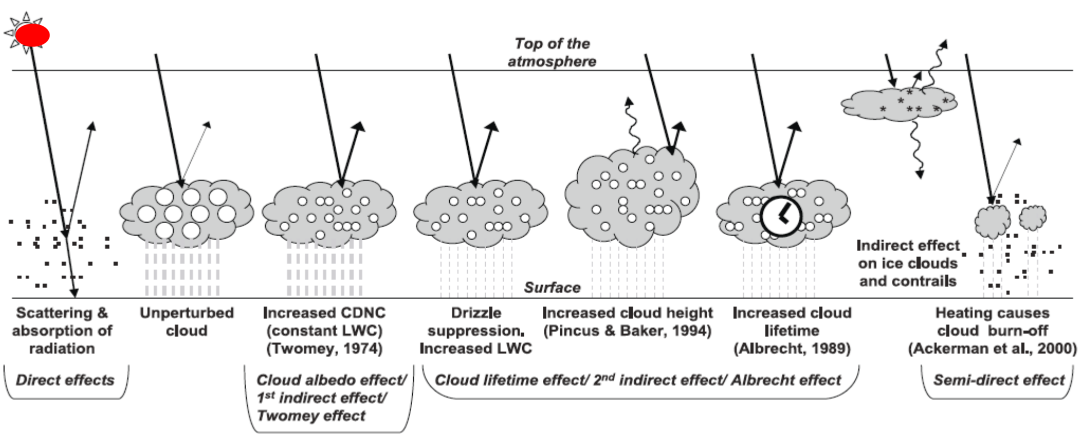

Figure 2.5 Known or suspected direct and indirect aerosol climate forcings. (source: IPCC, 2007)

According to the above mentioned definition of radiative forcing, the total radiative forcing F at a given level, expressed in units of energy per unit time and area, is defined as:

$$F = F^{net}_{perturbation} - F^{net}_{NO\,perturbation} \tag{2.51}$$

The first term corresponds to the total net flux (downward minus upward solar and longwave fluxes) at a certain level of the atmosphere that suffered an external perturbation and the second term to the total atmospheric net flux at a same level that did not suffer the perturbation.

Since the most significant direct effects of aerosol particles in the radiation field are connected to their interaction with sunlight, mainly through the scattering and sometimes absorption processes, it is more frequent to study and to assess only the SW radiative forcing due to an increase of the aerosol load in the atmosphere, leading to the following expression:

$$F_{SW} = F^{net}_{SW_{aerosols}} - F^{net}_{SW_{NO\,aerosols}} \tag{2.52}$$

2.1.2.4 The coupling with a radiative transfer code

It is essential that the aerosol and cloud interactions with solar and terrestrial radiation are introduced in the Meso-NH model, and that they are reverberated on the dynamics, concerning the study of the aerosol and cloud radiative impacts.

In the MesoNH model this is done via coupling with the ECMWF radiative transfer code, developed by Morcrette (1989). The microphysical / dynamical / radiative interactions are taken into account through the calculations of the radiative warming / cooling rates in the atmosphere (Bou Karam, 2008).

The code contains the solar and terrestrial spectrums in 6 spectral intervals for the shortwave wavelengths (0.185 - 0.25 – 0.44 – 0.69 – 1.19 – 2.38 – 4.00 μm) and 16 spectral bands in the domain of the thermal infrared (10 – 250 – 500 – 630 – 700 -820 – 9890 – 1080 – 1180 – 1390 – 1480 – 1800 – 2080 – 2250 – 2380 – 2600 – 3000 μm).

The radiative flux estimations are made in 1D and depend on the solar zenithal angle and on the flux at the top of the model. The processes of absorption and emission are taken into account for the infrared thermal radiation and the scattering and absorption of the solar radiation by the atmosphere and by the terrestrial surface, during the flux calculations. The fluxes are also calculated in different ways for clear sky and cloudy sky conditions.

The ECMWF radiative transfer code considers six different types of aerosols: low absorbing marine type, background stratospheric type, semi-urban absorbing type, volcanic, a type of mineral aerosols close to the emission sources and a last type of mineral aerosol distant from sources (continental), after the fading of the larger particles by sedimentation during the transport.

For the calculation of the aerosol optical properties, required by the code, such as the single scattering albedo, the complex refractive index and the asymmetry factor, pre-calculated Mie look up tables in the different spectral intervals are used (Tulet et al., 2008).

According to Bou Karam (2008), the coupling between MesoNH and this radiative code is made taking into account that the aerosol information such as concentration and size distribution at any grid point, is provided by MesoNH to the radiation code, allowing for the calculations of the aerosol optical thickness (at 550nm). This parameter is in fact proportional to the aerosol concentration. In return, the warming / cooling rate values calculated by the radiative code are introduced into the MesoNH model. More precisely, the radiative scheme acts directly on the temperature and pressure variables. Due to this fact, the aerosol radiative impact is taken into account in the MesoNH through these parameters and is able to reflect in the atmospheric profiles via the dynamic scheme of MesoNH.

2.1.3 Mineral dust aerosols within MesoNH

This subsection is divided in two parts: the first part presents the processes concerning the mobilization of desert dust particles and their emissions to the atmosphere and the second part of this subsection presents the Dust Entrainment and Deposition model (DEAD) (Zender et al., 2003a) and its coupling with MesoNH.

2.1.3.1 Mineral aerosols production modes

Considering that the atmosphere is a motion fluid around the spherical Earth, its motion is slowed down at the surface level by the presence of soil or water surface (Bouet, 2007). The surface wind is very sensitive to changes in surface characteristics at small scale. These modifications can be related to the presence of different types of soil vegetation. Regarding the first few meters of the atmosphere, a surface boundary layer develops, and the wind speed horizontal component presents a vertical gradient whose magnitude depends on the soil capacity to slowing down the atmospheric flow (Figure 2.6).

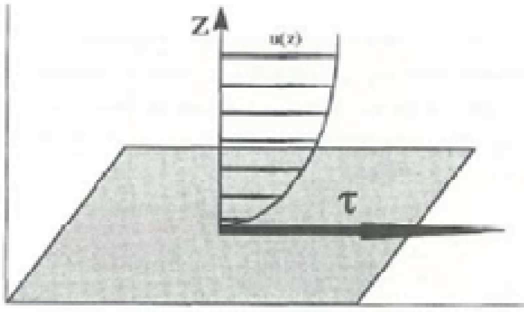

Figure 2.6 Illustration of the surface effect on the air flow and the tangential constraint τ exerted by the air flow on the surface (Alfaro, 1997). The wind velocity profile is represented by $u(z)$ the wind velocity horizontal component, which is dependent of the altitude z .

To quantify the friction forces exerted by wind on surface, a physical quantity is defined as friction wind speed u_* (Figure 2.6):

$$u_* = \frac{\tau}{\rho_a} \tag{2.53}$$

where ρ_a is the air density (in $kg\ m^{-3}$).

The wind speed profile may be given by (Priestley, 1959):

$$u(z) = \frac{u_*}{K} \ln\left(\frac{z}{Z_0}\right) \tag{2.54}$$

where u_* is the friction wind speed (in ms^{-1}), $K = 0.4$ is the Von Karman's constant and Z_0 is the height of the aerodynamic roughness (in m).

Z_0 indicates the effect of the surface roughness on the wind u and, consequently, influences the u effectiveness in mobilizing the material of the surface (Bouet, 2007 and Bou Karam, 2008).

- **Putting in movement the surface aggregate constituents**

The regions considered as sources of mineral aerosols emissions are constituted generally by aggregates (Petitjohn et al., 1972; Greeley and Iversen, 1985). These aggregates may be considered spherical, having all the same diameter (D_p) and the same density (ρ_p), in order to simplify the estimation of the effect of the atmospheric flow in these aggregates (Greeley and Iversen, 1985).

According to Bouet (2007), the gravity force, the capillary forces (when soil reaches a certain content of liquid water) and the interparticle cohesive forces *(*Iversen and White, 1982*)* are the ones applied on the soil grains and the ones responsible for the maintenance of the aggregates cohesion *(*McKenna-Neumann and Nickling, 1989; Fécan et al., 1999; Ishizuka et al., 2005*).* To put the soil grains in movement, it is necessary to exert a force, on the surface, greater and of opposite sign than the sum of the gravity force with the capillary forces and with the interparticle cohesive forces*.* It means that, for every soil type, there is a minimal friction velocity, called threshold wind friction velocity, U_t , which is necessary to be exceeded to tear off the particle from the surface. The threshold wind friction velocity values depend on the surface cover, surface composition, and surface humidity and on the particle diameter.

- **The different movements of the mobilized particles**

Particles turn off from the surface will get different movements, depending on to their size, as illustrated on Figure 2.7. Once raised, the particle is going to be subjected to its weight, which makes it fall again, and to the vertical resultant aerodynamic force, which supports its movement in the atmosphere.

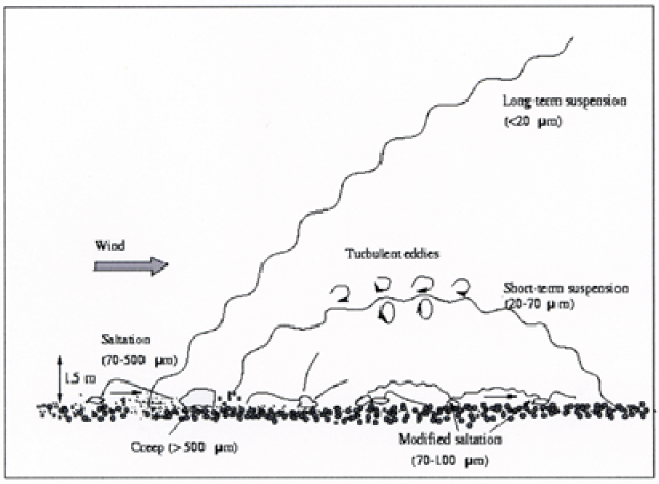

Figure 2.7 Surface grain movements under the effect of the wind according to their diameter (Shao and Lu, 2000).

According to Bouet (2007), to determine if the raised particle continues its rising or fall again back to the surface, it is enough to compare the particle threshold friction velocity, U_t, in a supposed immobilized air, with the wind friction velocity u_*.

If $U_t < u_*$ the particle enters in a rising movement called «suspension». Under natural conditions, ($0 < u_* < 100\ cm\, s^{-1}$), it is estimated that the particles whose diameter is less than $70\mu m$ are entrained in suspension (Bouet, 2007; Bou Karam, 2008). However, such particles are rarely found in a free state on natural soils and require a mechanical action that releases finer particles. In the case of particles whose diameter is between 20 and $70\mu m$, the suspension will be relatively brief, these particles will fall relatively close to source areas. In the case of particles whose diameter is less than $20\mu m$, the time during which the particle is in suspension may be longer and these particles can be transported for longer distances.

If $U_t > u_*$ the particle enters in an essentially horizontal movement, a process known as sandblasting where the aggregates, when entering in saltation and falling again on the surface, cause the release of the finer particles due to the aggregates kinetic energy (Gillette and Goodwin, 1974; Gillette and Walker , 1977), as shown in Figure 2.8.

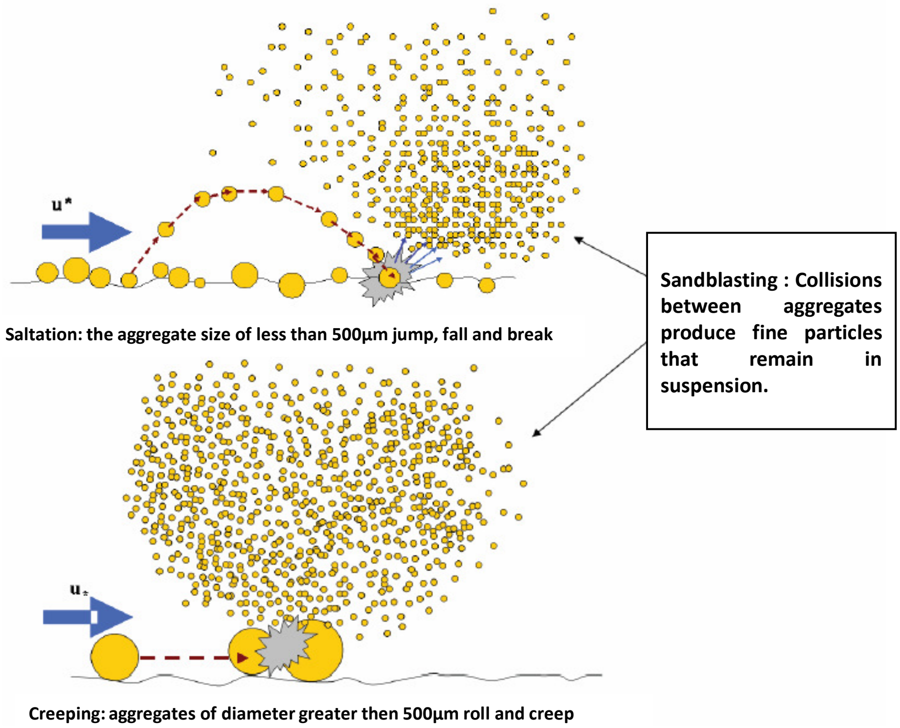

Figure 2.8 Sandblasting processes illustration (source Bouet, 2007).

Depending on their size, the particles can acquire a creep movement ($D_p > 500\mu m$) (Pye, 1987; Shao, 2000) or a saltation movement (Figure 2.8) ($70 < D_p < 500\mu m$). Considering this last movement situation, the intensity of production of fine particles depends on the relationship between the kinetic energy flux transferred by the aggregates and the particle cohesive forces forming the aggregates.

According to Bouet (2007) and Bou Karam (2008), in order to quantify the effectiveness of putting in movement the surface particles due to the wind velocity, it is possible to define a saltation flux, Q_s . This flux, expressed in $g\,cm^{-1}\,s^{-1}$, is described as the particle mass which crosses, in every second, a rectangular surface with unitary width and infinite height, placed perpendicularly to the surface and with the flow direction (Bagnold, 1941).

Due to their small size, the finer particles liberated by sandblasting, are then directly drawn away in suspension and constitute, in this sense, the fundamental of mineral aerosols vertical flux.

This vertical flux, expressed in $\mu g\,m^{-2}\,s^{-1}$, is defined as the particle mass crossing, by unit time, a unit surface area, parallel to the surface. It is also proportional to the horizontal flux of particles released by sandblasting (Marticorena et al. 1997). The approximate aerosol emissions in the atmosphere are therefore crucial to estimate the vertical fluxes.

An actual knowledge of the physical processes represented before, responsible for the production of the mineral aerosols is needed by the currently atmospheric models that work with the modulation of the desert mineral dust emissions (MesoNH, RegCM, RAMS,…). To note that these models are also restricted to the available data experiments. Therefore, the dust emission schemes, which were developed with this aim (Marticorena and Bergametti, 1995; Shao et al., 1996; Alfaro et Gomes, 2001; Shao, 2001), numerically reproduce the saltation and sandblasting processes (Bou Karam, 2008).

2.1.3.2 The Dust Entrainment and Deposition model

According to Marticorena and Bergametti (1995), the flux of desert dust aerosols is calculated according to the processes of saltation and sandblasting. This is the physical basis where the Dust Entrainment and Deposition model (DEAD) (Zender et al., 2003a) is based.

DEAD provides desert dust fluxes from the wind friction velocities, which are themselves parameterized according to the factors on which they depend (soil humidity, surface roughness, etc…). In order to best simulate the interaction between the surface and the air flow, DEAD has its own boundary layer where the friction velocity, the soil type, and the soil water content are represented.

In the processes of mineral dust aerosol uprising, the friction velocity threshold (U_t) is a key element, since it controls the frequency and intensity of emissions. It is therefore primordial to well define this threshold and pay particular attention to the retrieval of parameters on which U_t depends. The erosion threshold can be considered as function of the surface roughness $\left(R_g\right)$, the diameter of soil grains $\left(D_p\right)$, and soil humidity $\left(W\right)$ (Bou Karam, 2008). For a smooth surface and a dry soil (idealized consitions), U_t depends only on the soil grain diameters, $U_t\left(D_p\right)$ and can be determined according to the formulation of Marticorena and Bergametti (1995), which consists in adjusting an empirical expression as a function of the particle diameter:

For $0.03 \leq \mathrm{Re} \leq 10$

$$U_t\left(D_p\right)=\left[\frac{0.1666681\rho_p\, g\, D_p}{-1+1.928\left(\mathrm{Re}\right)^{0.0922}}\left(1+\frac{6\cdot 10^{-7}}{\rho_p\, g\, D_p^{\;2.5}}\right)\right]^{\frac{1}{2}}\rho_p^{\;-\frac{1}{2}} \tag{2.55}$$

For $\mathrm{Re}\geq 10$

$$U_t\left(D_p\right)=\left\{0.0144\rho_p\, g\, D_p\left[1-0.0858e^{-0.0517\left(\mathrm{Re}\;-10\right)}\right]\left(1+\frac{6\cdot 10^{-7}}{\rho_p\, g\, D_p^{\;2.5}}\right)\right\}^{\frac{1}{2}}\rho_p^{\;-\frac{1}{2}} \tag{2.56}$$

ρ_p is the particle density, g is the acceleration due to gravity and Re is the Reynolds number defined by:

$$\mathrm{Re}=\frac{U_t\, D_p}{v} \tag{2.57}$$

where $v = 0.157\, cm^2 s^{-1}$ represents the kinematic viscosity.

The existence of interstitial water between the soil grains has the effect of increasing the cohesion between the soil particles and therefore on the increase of the friction velocity threshold. This increase is integrated into DEAD module through a parameterization developed by Fécan et al. (1999). When the soil humidity (W) becomes higher than the soil residual humidity (W_s) , the threshold increase in humid conditions (U_{tw}) related to the threshold in dry conditions (U_t) is determined by:

For $W > W_s$

$$U_{tw}=U_t\left[1+1.21\left(W-W_s\right)^{0.68}\right]^{\frac{1}{2}} \tag{2.58}$$

For $W < W_s$

$$U_{tw}=U_t \tag{2.59}$$

The soil moisture threshold is a function of the clay soil content, and can be written as:

$$W_s=0.17(\%Clay)+0.14(\%Clay)^2 \tag{2.60}$$

The effects of the soil roughness on the friction velocity threshold are set in DEAD scheme according to the parameterization of Marticorena and Bergametti (1995), which consists of a relationship between the roughness length of the smooth surface, Z_{0s}, and the roughness length of the erodible surface, Z_0 (Bou Karam, 2008). This relationship is given by:

$$R_g = 1 - \frac{\ln\left(Z_0 / Z_{0s} \right)}{\ln\left[0.35 \left(10 / Z_{0s} \right)^{0.8} \right]} . \tag{2.61}$$

Consequently, the friction velocity threshold, function of the soil aggregates diameter, of the roughness length of the erodible surface and roughness length of the smooth surface, can be expressed as:

$$U_t \left(D_p, Z_0, Z_{0s} \right) = \frac{U_t \left(D_p \right)}{R_g \left(Z_0, Z_{0s} \right)} \tag{2.62}$$

The horizontal saltation flux *Qs* (in $kg \cdot m^{-1} \cdot s^{-1}$) in calculated in DEAD trough the White's (1979) relationship. This equation allows for the computation of the amount of material mobilized by wind as a function of wind friction velocity:

$$Q_s = \frac{C_s \rho_{air} u_*^3}{g} \left(1 - \frac{U_t}{u_*} \right) \left(1 + \frac{U_t}{u_*} \right)^2 \tag{2.63}$$

where $C_s = 2.6$ is a constant and ρ_{air} is the air density.

Q_s depends thus, directly of D_p, Z_0 and Z_{0s}, considering the expression kept by Marticorena and Bergametti (1995) to parameterize the friction velocity threshold (equation 2.63).

Marticorena et al. (1997) established a proportionality relationship between the vertical flux of emitted particles to the atmosphere (F) and the saltation flux (Q_s), taking into account that the available quantity of soil fine particles controls the soil ability to produce them. The ratio between the vertical flux and the horizontal flux is a function of the clay content on the soil. For clay contents between 0 and 20% this ratio (α) is given by:

$$\alpha = \frac{F}{Q_s} = 100 \cdot e^{(13.4\%Clay - 6)\cdot \ln 10} \tag{2.64}$$

The flux of desert dust aerosols emitted to the atmosphere can be calculated from this equation. According to Bou Karam (2008), this expression, allows for finding the orders of greatness of emissions fluxes with an identical confidence level for every soil of desert regions. It leads only to global information on the emission flux (total mass emitted flux), without any information on the distribution of this flux in the different size classes. However, the work of Alfaro and Gomes (2001), allows for the estimation of the dust flux, calculated using this formulation, in three modes taking into account the dependency on size distribution of the flux particles and the wind conditions (Alfaro et al., 1998). Nevertheless, this scheme does not take into account the limited conditions of soil in erodible material, being only applicable to soils always furnished with erodible material produced by aeolian erosion. This limitation drives to overestimations of the desert dust flux in regions with encrusted soil. Another limitation of this scheme is that it does not take into account the fine particles liberated by collisions between the present particles in air, after the sandblasting. In fact, laboratory studies with the 'wind tunnel' technology showed that this mechanism is very frequent despite the fact that it requires energy much higher than the energy solicited during the bombing of the surface by aggregates (Dong et al., 2002). This second limitation drives, on the other hand, to an underestimation of the aerosol quantity present in the air.

- **The coupling with MesoNH**

DEAD was coupled with the model MesoNH according to what is described in Grini et al. (2006). MesoNH provides to the DEAD scheme, for every time step, the necessary input data for the mass flux estimation of emitted mineral aerosols. DEAD provide to MesoNH, in response, for every time step, the calculated aerosol flux (Bou Karam, 2008). The DEAD input data comprise: the wind friction velocity, the soil humidity, the roughness length of the erodible surface and the roughness length of the smooth surface estimated from the SurfEx surface scheme of MesoNH (see section 2.1.1).

2.1.3.3 Modelling the transport and the dry and humid deposition

Desert dust particles are size distributed according to Alfaro and Gomes (2001), once lifted and injected through MesoNH. It is a three mode lognormal distribution whose modal radius are: $0.75\mu m$ (9% in mass), $3.35\mu m$ (43% in mass), and $7.1\mu m$ (48% in mass). The module ORILAM (Organic and inorganic log-normal aerosols model, Tulet et al., 2005) provide the aerosol transport in the MesoNH model. ORILAM simulates the time and spatial evolution of the lognormal distribution of the aerosols in the atmosphere. It is a dynamic model in which moments of different order are treated. These moments correspond respectively to the number concentration, average radius and to standard deviation of the aerosol size distributions (Binkowski and Roselle, 2003).

Besides, particle coagulation and nucleation during the transport, ORILAM also takes into account the dry deposition (D_s) and sedimentation processes. These last two processes are driven by the Brownian diffusivity:

$$D_s = \left(\frac{kT}{6\pi\upsilon\rho_{air} r_p}\right) C_C \tag{2.65}$$

and by gravitational velocity:

$$V_{g,p} = \left[\frac{2g}{9\upsilon}\left(\frac{\rho_{p,i}}{\rho_{air}}\right) r_p^2\right] C_C \tag{2.66}$$

where k is the Boltzmann constant, T is the ambient temperature, υ is the air kinematic velocity, ρ_{air} is the air density, g is the gravitational acceleration, r_p is particle radius, C_C is the gliding coefficient and $\rho_{p,i}$ is the aerosol density of mode i .

2.1.4 Clouds within MesoNH

The interactions between aerosols and the cloud structure intervene at the cloud scale therefore it is necessary to study these interactions using mesoscale models, such as MesoNH, to be able, in a second time step, to establish consistent and effective parameterizations for global scale climate models.

2.1.4.1 The cloud particles

Several microphysical schemes are available in MesoNH model, as described in the following section, considering warm and cold phases only or mixed-phase clouds.

Despite the scheme used by the modeler, the warm cloud phase, the cloud water vapor, the cloud water and cloud rain are always considered in all of the available microphysical schemes (see dashed box in the bottom left of Figure 2.9). On the other hand, the number of ice hydrometeors considered depends on the chosen microphysics scheme for the ice phase / mixed-phase cloud. For this ice phase / mixed-phase cloud, the maximum number of ice hydrometeors is four, and includes: pristine ice, snow, graupel and hail (Berthet, 2010). Figure 2.9 illustrates the life cycles of these hydrometeor classes within a mixed-phase cloud system.

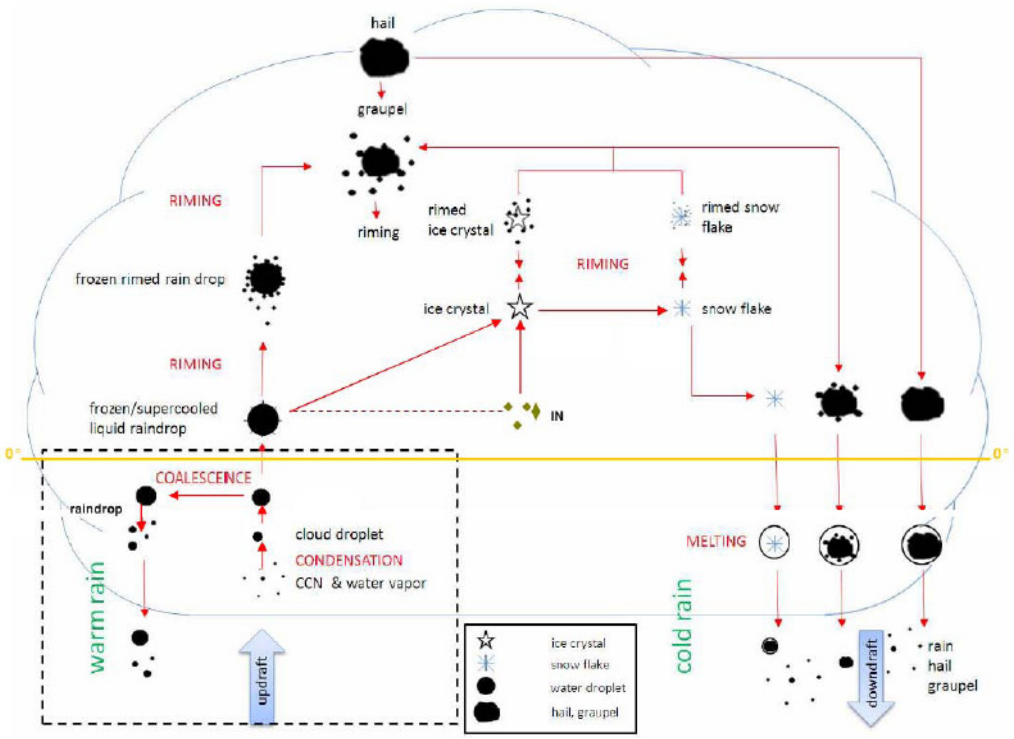

Figure 2.9 Different hydrometeor classes cycle in MesoNH model. Source: Adapted from W. Langhans, COPS Summer School 2007.

According to Berthet (2010), the MesoNH model has "bulk" microphysical schemes, where the hydrometeors follow the size distribution laws, determined in advance. On the contrary, models where the microphysics is represented by the diameter classes are called “class by class” models. Depending on the choose of the microphysics scheme to be simulated by the MesoNH model, the expression of these moments, which characterize the different hydrometeors, is invariant. The microphysical scheme assumes that the six hydrometeor classes (rain, snow/aggregate, graupel, and hail) with an assigned index h ∊ [r, s, g, h], follows a generalized gamma distribution, given below in the normalized form:

$$n(D)dD = N_h g(D)dD = N_h \frac{\alpha_h}{\Gamma(\nu_h)} \lambda_h^{\alpha_h \nu_h} D^{\alpha_h \nu_h - 1} \exp\left[-(\lambda_h D)^{\alpha_h}\right] dD \qquad (2.67)$$

where D is the maximum dimension of the particles, $g(D)$ is the normalized hydrometeor distribution law, dependent on the dispersion parameters α_h, ν_h and on the slope parameter λ_h, related to the considered hydrometeor class h and Γ is the Gamma Function (Press et al., 1992). N_h is the total number concentration of the h hydrometeor, prognostic variable for cloud water, rain and pristine ice, and diagnostic variable for the other ice hydrometeors.

The generalized gamma law use allows the representation of the particle size distribution while $M(p)$, the p^{th} moment, for hydrometeors, of the law is calculated as:

$$M(p) = \int_0^\infty D^p g(D)dD = \int_0^\infty D^p \frac{\alpha_h}{\Gamma(\nu_h)} \lambda_h^{\alpha_h \nu_h} D^{\alpha_h \nu_h - 1} e^{-(\lambda_h D)^{\alpha_h}} dD = \frac{1}{\lambda_h} \frac{\Gamma(\nu_h + p/\alpha_h)}{\Gamma(\nu_h)} \qquad (2.68)$$

where $N_h M_0 = \int_0^\infty n(D)dD = N_h$ is the hydrometeor class concentration, M_1 gives the average diameter distribution, and $\frac{4}{3}\pi N_h M_3 = \int_0^\infty m(D)n(D)dD = \rho_{air} q_h$ calculates the mixing ratio of the considered hydrometeor.

2.1.4.2 Microphysical Processes

Figure 2.10 presents an outline of the several interactions operating between the different water species (shown in Figure 2.9) and the related microphysical processes which are taken into account.

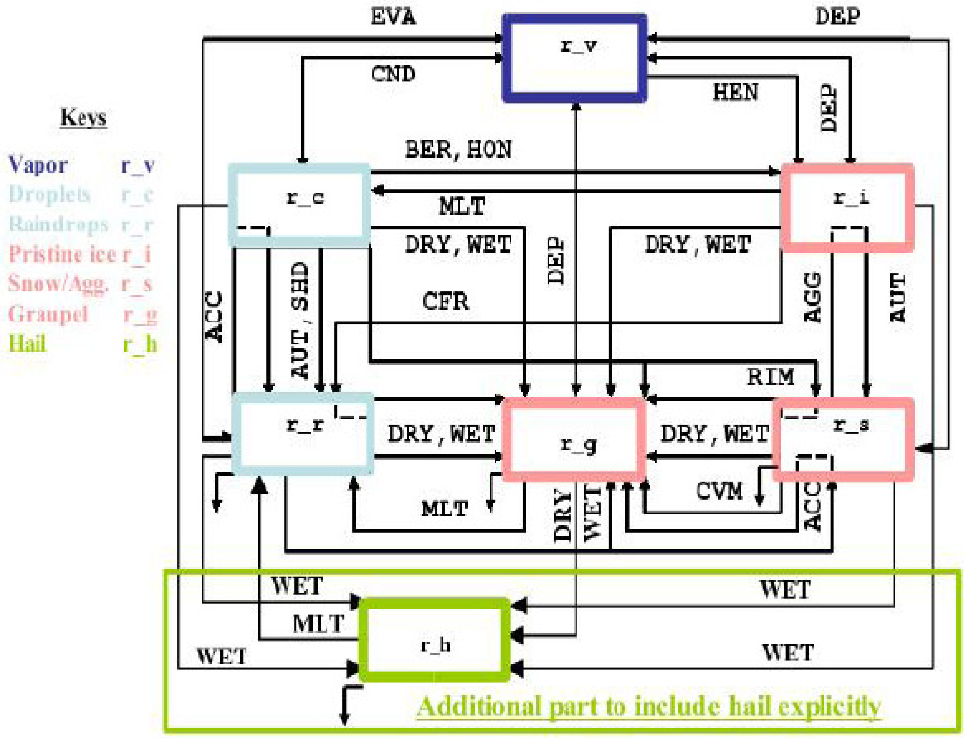

Figure 2.10 Microphysical processes included in the mixed-phase scheme in MesoNH model. With the mixing ratio of water vapour (r_v,), cloud droplets (r_c), raindrops (r_r), pristine ice (r_i), snow/aggregates (r_s), graupel (r_g) and hail (r_h). Source: Berthet (2010),

- Warm cloud phase

Cloud nucleation happens once, for an air parcel saturated by adiabatic or diabatic cooling or mixing processes, small drops form as water molecules change from the gaseous to the liquid phase. The newly formed water drop is unstable unless it achieves a significant size where the energy necessary to maintain the surface tension is smaller or in equilibrium with the energy liberated by the phase change. In the atmosphere, water drops form by heterogeneous nucleation with an aerosol particle acting as a cloud condensation nuclei (CCN). Availability, chemical structure, and size distribution of CCNs have a large effect on cloud drop formation in the atmosphere.

Once the drop is formed, may continue to grow by water vapor diffusion from the air to the drop, through the condensation process (CND). The opposite process when water molecules disperse from the drop to the air is described as evaporation (EVA). During condensation latent heat is released from the drop to the surrounding air and during evaporation the heat has to be provided by the atmosphere.

Growing drops achieve the position where their fall velocity is not any more unimportant and particles leave the volume through sedimentation (SED). Drops with different sizes get to different terminal sedimentation velocities and larger drops descending faster can have a collision and join with smaller drops during their fall. This important process in the formation of the typical rain drop spectrum is designed by coalescence. The coalescence processes involve the autoconversion (AUT) process, whereby cloud droplets grow to drizzle-drop size and the accretion (ACC) process, whereby cloud droplets grow to raindrops.

- Cold cloud phase

Pristine ice crystals are initiated by heterogeneous nucleation or by homogeneous freezing. These processes are called, correspondingly, HEN (for "Heterogeneous nucleation ") and HON (for "Homogeneous Nucleation ") in Figure 2.10.

Liquid water droplets in clouds do not spontaneously freeze when they are lifted above the freezing level by updrafts. The freezing process is a gradual one, as some of the droplets encounter ice nuclei and freeze into ice crystals as a result. According to Bergeron and Findeisen, a mixed environment of supercooled droplets and a few ice crystals promotes rapid diffusional growth of the ice crystals as a consequence of the saturation vapor pressure over ice being lower than that over liquid water. Once these crystals are formed, there are two growth modes: the vapour deposition (DEP) or solid condensation and the Bergeron-Findeisen process (BER), which is equivalent to a mass transfer of small droplets surrounding a certain crystal.

According to Berthet (2010), the autoconversion (AUT) of these pristine crystals of ice in snow has been adapted from Harrington et al. (1995), which considers the sublimation or deposition (DEP) as the most effective process of crystal growth. Once this crystal reaches a critical size, they are comparable to snow crystals. The snow crystals grow by sublimation (DEP), icing cloud of water droplets (RIM), accretion of rain (ACC) or following aggregation of ice particles (AGG), the collection of nuclei initially defined by Long (1974) to accretion of rain, have been transposed by the aggregation of snow pristine ice crystals.

The collect of droplets and drops by ice crystals (CFR) or snow (CVM) is based on continuous core collection (Pruppacher and Klett, 1997; Seinfeld and Pandis, 1998), and allows the conversion of part of the ice / snow graupel, beyond a critical size. Graupel is formed following icing of snow (RIM) and it grows by vapor deposition (DEP) or accretion (VAC) depending on the temperature of the atmosphere. Graupel is subject to two distinct modes of growth: dry (DRY) or wet (WET). The initiation of hail is based on a conversion rate of graupel hail, which depends on a weighting factor calculated from the growth trends, dry (DRY) or wet (WET) (Berthet, 2010).

2.1.4.3 Microphysical diagrams

Three microphysical schemes for warm clouds are currently implemented in the MesoNH model. The simplest one is the one moment scheme developed by Kessler (1969) which predicts the mixing ratios of cloud water and rain; the other two microphysical schemes are two moment schemes that predict the cloud water content and rain content and the concentration of cloud droplets and rain.

The first scheme that was implemented was the C2R2 scheme developed by Cohard and Pinty (2000a, b). The second scheme was the KHKO scheme and it was developed by Khairoutdinov and Kogan (2000) and has been implemented and validated by Geoffroy (2007).

KHKO is especially dedicated to weakly precipitating clouds that are stratocumulus, while C2R2 has been established for the whole universe of precipitating clouds.

The C2R2 microphysical scheme diagnoses the droplet concentration formed from a monodisperse population of CCN and a constant homogeneous spread in space. For these schemes, the atmosphere is an infinite reservoir of CCN. Similarly, the C2R2 scheme estimates the amount of nucleated droplets from an homogeneous mode of CCN. However, in C2R2 scheme the concentration of activated CCN is a prognostic variable, thereby constrain the number of CCN activated to the CCN number that is actually available in the surrounding atmosphere.

Modeling cold phase microphysics has gone through various stages of development, like the warm phase, resulting then in the one moment diagram ICE3 and, after some improvements, in the one moment diagram ICE4, where the hail hydrometeor class was included. Thereby, the association of these modules to C2R2 for the cold stage or mixed phase clouds, results in a scheme called C1R3. The association C2R2 + C1R3 = C3R5 corresponds to a scheme for mixed-phase clouds, including five mixing ratios (water cloud, rain, pristine ice, snow, graupel, with optional hail), where three concentrations (for cloud water, rain and pristine ice) are prognosticated (Berthet, 2010).

2.1.5 Interaction between aerosols and clouds

According to Denman et al., 2007 and several other authors (i. e. Bréon et al., 2002; DeMott et al., 2003), aerosols interact with clouds through several ways, acting either as CCN or IN, or as absorbing particles, reorganizing solar energy as thermal energy within cloud layers. The aerosol indirect effects, which are the issue of this section, can be separated into diverse contributing processes, as shown in Figure 2.11.

The distribution of the cloud liquid water content over more, therefore smaller, cloud droplets leading to higher cloud reflectivity (the cloud-albedo effect) are connected to radiative forcing (see section 2.1.2.3). Twomey (1974) has considered that aerosols particles decrease the cloud droplet size per given liquid water content (decreasing also the formation of precipitation) and, according to Albrecht (1989), the cloud lifetime is prolonged. According to Ackerman et al. (2000), the semi-direct effect is associated to the absorption of solar radiation by soot, re-emitted as thermal radiation, and consequently heating the air mass. It may also cause evaporation of cloud droplets.

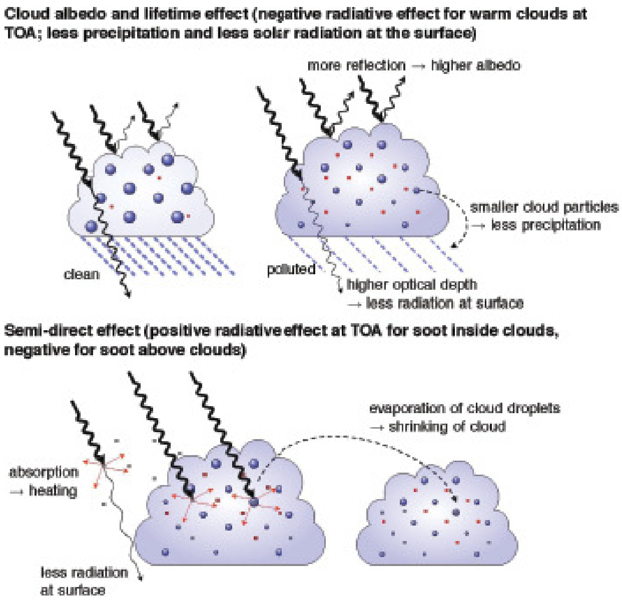

Figure 2.11 Schematic diagram of some aerosol effects (Adapted from Denman et al., 2007).

The aerosol fields are taken into account in the MesoNH cloud microphysics scheme. The aerosol mass transfer inside the cloud and inside the rain droplets is taken into account in MesoNH by autoconversion and accretion processes, according to (Pinty et al., 1998).

On the other hand, the effect of clouds and precipitation on the aerosol fields is also considered in MesoNH: if precipitation occurs, the clouds perturb the aerosol field washing them though collision with drops in free fall. This aerosol field washing is explicitly determined by using a kinetic approach to calculate the aerosol mass transfer in the cloud and in the rain droplets, as defined by Seinfeld et al. (1997), Pruppacher and Klett (1978) and Tost et al. (2006). The aerosol mass sedimentation included in the rain drops is also solved. The aerosol mass released to the atmosphere, after the rain drops evaporation is assumed to be proportional to the quantity of evaporated water (Chin et al., 2000).

2.2 The MODIS instrument

The Moderate Resolution Imaging Spectroradiometer (MODIS, Salmonson et al., 1989; King et al., 1992) is an instrument with the capability to describe the spatial and temporal characteristics of the global atmosphere field. Launched aboard NASA's Terra and Aqua satellites in December 1999 and May 2002, respectively, with the latter joining the A-train constellation (http://modis.gsfc.nasa.gov). The polar orbit of Terra (http://terra.nasa.gov) passes over the equator from north to south in the morning, whereas Aqua (http://aqua.nasa.gov) has an ascending node over the equator during the afternoon.

Primary Use	Band number	Central wavelength [nm]	Bandwidth[nm]	Spatial resolution [m]
Land / Cloud / Aerosols / Boundaries	1	645	620 – 670	250
	2	858.5	841 – 876	
Land / Cloud / Aerosols Properties	3	469	459 – 479	500
	4	555	545 – 565	
	5	1240	1230 – 1250	
	6	1640	1628 – 1652	
	7	2130	2105 – 2155	

Table 2.1 Specification of the first 7 MODIS channels, including primary use, central wavelength, bandwidth and spatial resolution.

The MODIS radiometers are composed of 36 spectral bands, spanning the spectral range from 400nm to 1440 nm representing three spatial resolutions: 250 m × 250 m (2 channels), 500 m × 500 m (5 channels), and 1 km × 1 km (29 channels).

Tables 2.2 and 2.3 present the specifications of the 36 MODIS channels, including their primary use, central wavelengths, bandwidths and spatial resolutions.

Their wide swaths of 110 º (i.e. 2330 km) provide a global coverage of the Earth's surface from one to two days.

Primary Use	Band number	Central wavelength [nm]	Bandwidth[nm]	Spatial resolution [m]
Ocean Colour / Phytoplankton / Biogeochemistry	8	421.5	405 – 420	1000
	9	443	438 – 448	
	10	488	483 – 493	
	11	531	526 – 536	
	12	551	546 – 556	
	13	667	662 – 672	
	14	678	673 – 683	
	15	748	743 – 753	
	16	869.5	862 – 877	
Atmospheric Water Vapour	17	905	890 – 920	
	18	936	931 – 941	
	19	940	915 – 965	
Surface / Cloud Temperature	20	3750	3660 – 3840	
	21	3959	3929 – 3989	
	22	3959	3929 – 3989	
	23	4050	4020 – 4080	
Atmospheric Temperature	24	4465.5	4433 – 4498	
	25	4515.5	4482 – 4549	
Cirrus Clouds / Water Vapour	26	1375	1360 – 1390	
	27	6715	6535 – 6895	
	28	7325	7175 – 7475	
Cloud Properties	29	8550	8400 – 8700	
Ozone	30	9730	9580 – 9880	
Surface / Cloud Temperature	31	11030	10780 - 11280	
	32	12020	11770 - 12270	
Cloud Top Altitude	33	13335	13185 - 13485	
	34	13635	13485 - 13785	
	35	13935	13785 - 14085	
	36	14235	14085 - 14385	

Table 2.2 Specification of the MODIS channels (8-36), including primary use, central wavelength, bandwidth and spatial resolution.

There are two MODIS Aerosol data product files: MOD04_L2, containing data collected from the Terra platform; and MYD04_L2, containing data collected from the Aqua platform. The two MODIS Cloud data product files are: MOD06_L2, containing data collected from the Terra platform; and MYD06_L2, containing data collected from the Aqua platform.

The aerosol retrieval algorithm used to provide the MODIS aerosol product, makes use of seven of the channels (0.47–2.13 µm) to retrieve aerosol several aerosol characteristics, such as aerosol optical depth (AOD), among others, and uses additional wavelengths in other parts of the spectrum to identify clouds (Ackerman et al., 1998; Gao et al., 2002; Martins et al., 2002).

Unlike previous satellite sensors, which did not have sufficient spectral diversity, MODIS has the unique ability to retrieve AOD with greater accuracy (Tanré et al., 1996; Tanré et al., 1997). This aerosol property is then reported at 10 km spatial resolution in the MOD04 data. Based on theoretical sensitivity studies, the uncertainties in the $\tau_{0.55}$ retrievals are estimated to be $\pm 0.05\tau_{0.55}$ over the ocean (Tanré et al., 1997).

Early comparisons of the retrieved aerosol parameters with ground-based data showed significant conformity between the two types of data (Chu et al., 2002; Remer et al., 2002), but also showed situations in which the algorithms could be improved.

Using measured radiances with 500 m spatial resolution from six bands between 459–2155 nm, the primary aerosol products retrieved by the MODIS algorithm include the spectral aerosol optical depth (Tanré et al., 1997).

The MODIS aerosol optical depth product has been validated against sunphotometer derived values over oceans and recent results have confirmed that the MODIS algorithm over ocean areas is performing within the expected accuracy)Remer et al., 2002).

The MODIS Cloud Product (MOD 06) combines infrared and visible techniques to determine both physical and radiative cloud properties. Daily global Level 2 (MOD 06) data are supplied. Cloud optical thickness is derived using the MODIS visible and near-infrared channel radiances. The MOD06 product provides cloud optical parameters, such as cloud optical depth (COD) and cloud effective radius, at 1 km resolution (Ackerman et al., 1998).

Ham et al. (2009) simulated the TOA radiances for 15 MODIS bands for cloud pixels collocated with AIRS (Atmospheric Infrared Sounder), CloudSat, and CALIPSO (Cloud–Aerosol Lidar and Infrared Pathfinder Satellite Observation) measurements. The MODIS cloud products are used as input to a Radiative Transfer Model, and Ham et al. (2009) found that radiances for the SW bands between 0.466 and 0.857 mm can be simulated within about a 5% uncertainty, suggesting that MODIS COD and effective radii seem to provide sufficient information for the radiance simulations at SW bands.

Two data sets are used in this work: the MODIS Level 2 daily aerosol products (Tanré et al., 1997) are used to obtain the AOD; and the MODIS Level 2 daily cloud product (Ackerman et al., 1998) are used to retrieve the COD.

2.3 The VAISALA Ceilometer

A VAISALA Ceilometer CL31 is a compact and lightweight instrument that uses a pulsed diode laser LIDAR (light detection and ranging) technology, where short, powerful laser pulses are sent out in a vertical or near vertical direction, and may be very useful for cloud studies. This instrument measures the reflection of light (backscatter) caused by clouds, precipitation or other obscuration, which is analyzed and used to determine the cloud base height. A VAISALA CL31 Ceilometer is installed in the observatory of the Évora Geophysics Centre (CGE), as shown in Figure 2.11, since the beginning of May 2006 (Costa et al., 2007). The instrument measures the cloud base height up to three layers simultaneously, as well as the atmospheric backscattering.

Figure 2.12 VAISALA Ceilometer CL31, installed in the CGE observatory in Évora (38º34' N, 7º54''W, 300m a.m.s.l.), in the South of Portugal.

The CL31 uses a second generation of advanced single lens design, providing excellent performance, which is used for transmitting and receiving light. This ceilometer also has a measurement range from 0 to 7.5km, maximum reporting resolution of 5m and programmable measurement cycle (from 2 to 120s). The CL31 uses an eye-safe laser InGaAs diode at 910nm. A full description of Vaisala CL31 Ceilometer can be found at http://vaisala.com.

2.4 Case studies

As the main purpose of this work is the study of mineral desert dust aerosol and of cloud properties and as well as their interaction, two periods, in two different years (2006 and 2007), were considered. These selected periods correspond to strong Saharan desert dust storms which travel over the Atlantic Ocean and over the Southwestern part of the Iberian Peninsula.

The first studied period occurred on 27, 28 and 29 May 2006 (see Figure 3.1) and the second one was on 06, 07 and 08 September 2007 (Figure 3.2).

Besides the MesoNH simulations of the aerosol and cloud microphysical properties, the backtrajectory analysis at different altitudes and the comparison with satellite and ground based remote sensing data were performed to validate the model simulations.

2.4.1 MesoNH simulations

In the simulations performed, the MesoNH was initiated and forced by six-hourly ECMWF analyses. A period of May 2006 was considered for the study, with the simulations starting at 00:00 UTC on 26 May and ending at 00:00 UTC on 30 May. On September 2007 the simulations started at 00:00 UTC on 05 September ending at 00:00 UTC on the 09 September. The first day of simulation has been used as a model spin-up period.

For this work, MesoNH run in a two way nested mode on two grids. For the May 2006 episode and in the horizontal plane, the coarser domain had 60 x 90 grid points, with 50 km grid spacing (Figure 2.12a), and the finer domain had 150 x 225 points and a space resolution of 10 km, as shown in Figure 2.12b. The largest domain is defined between 5ºS and 50ºN latitude and 25ºW and 15ºE longitude (which contains the potential dust source) and the smallest domain defined between 28º S and 47ºN latitude and 20ºW and 4ºW longitude.

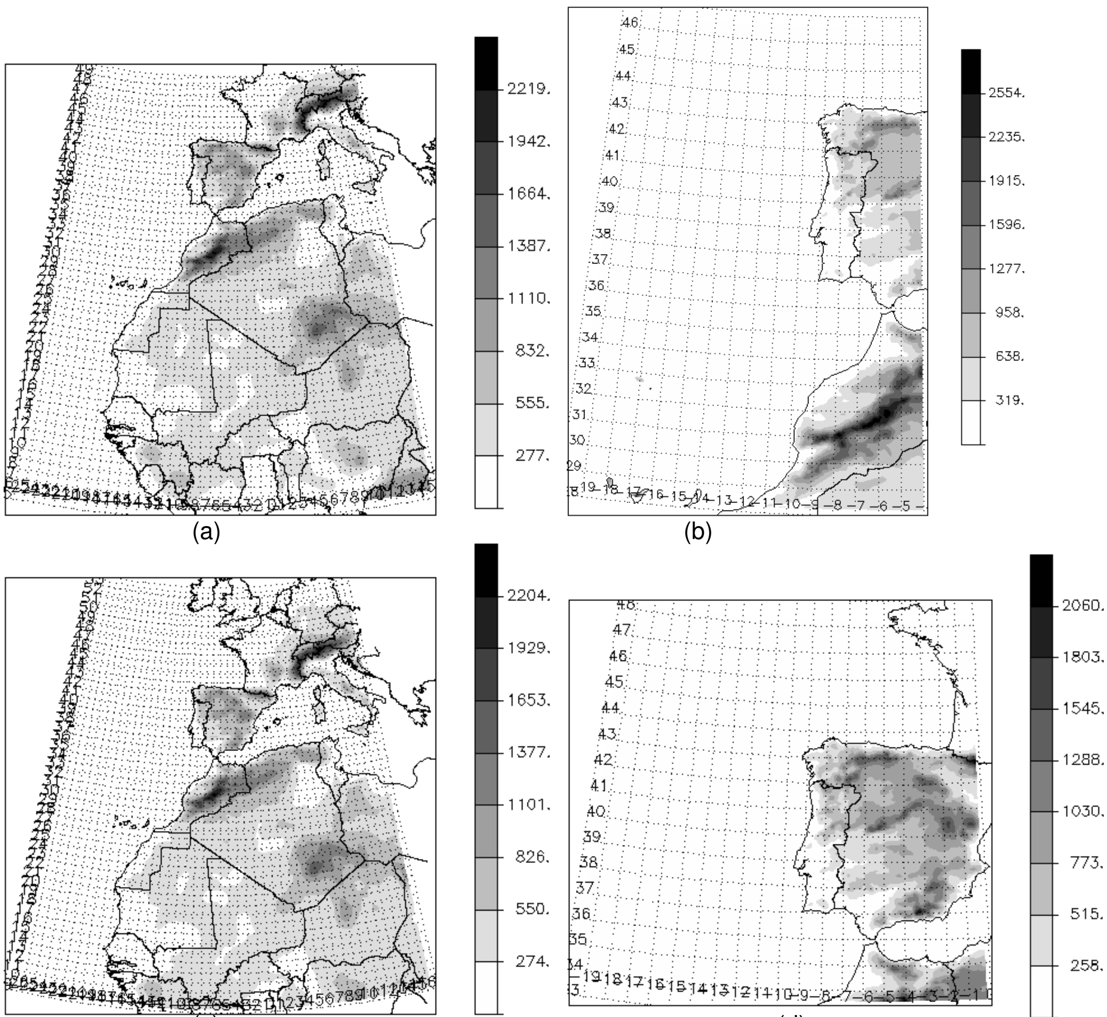

Figure 2.13 Simulation domains with topography (m): 50-km mesh size coarser domain (a, c) and 10km mesh size innermost domain (b,d) for 27 May 2006 (a,b) and 06 September 2007 (c, d).

Concerning the September 2007 episode the coarser domain had 80 x 100 grid points, with 50 km grid spacing in the horizontal plane, as shown in Figure 2.12c, and the finer domain had 180 x 180 points and a space resolution of 10 km (Figure 2.12d). The largest domain is defined between 8ºS and 55ºN latitude and 28ºW and 16ºE longitude (where the dust source is located) and the smallest domain defined between 33º S and 49ºN latitude and 20ºW and 0º longitude.

The vertical resolution used in this work, consists of 49 layers from the surface up to 24km altitude, distributed mostly in the lower troposphere (20 layers in the first 2km altitude). The first layer is situated approximately 10m above the surface.

Some of the model characteristics and options considered for this work are indicated in the Table 2.3.

Dynamics	Anelastic equations system of Lipps e Hemler (1982)
Planetary boundary layer	Bougeault e Lacarrére (1989) scheme
Clouds	ICE3 Mixed microphysical scheme including ice, snow and graupel (six classes of hydrometeors)
Aerosols	Dust aerosols are parameterized following Grini et al. (2006) and Tulet et al.(2005). For emission processes, dust is mobilized using the DEAD model (Zender et al. 2003).
Surface -Atmosphere interactions	ISBA (Interaction Surface Biosphere Atmosphere, Noilhan e Planton, 1989) TEB (Town energy Budget, Masson, 2000)
Databases for surface parameters	Ecoclimap for land cover (Masson, 2003) FAO global soil map (FAO, 1998; Salgado, 1999) GTOPO 30 (USGS, 1997)
Radiation	European Centre for Medium-Range Weather Forecast radiative scheme (Mocrette, 1991)
Horizontal scattering	Operator ∇^4
Lateral boundary conditions	Open, also considered radiative

Table 2.3 MesoNH characteristics and options used in this work.

In this work the MesoNH simulations were made with 1 hour time resolution.

The atmospheric variables simulated in this work are: the aerosol optical depth, at 0.55µm, (AOD), the cloud fraction (CLDFR), the cloud optical depth (COD), the cloud liquid water effective radius (CLWER), the base height of convective clouds (CLBASCONV), the top height of convective clouds (CLTOPCONV) and the upward and downward radiative fluxes (SW and LW) for normal and clear-sky conditions.

2.4.2 HYSPLIT Backtrajectories

The 72-hour air mass backward trajectories, ending over selected regions of the area of study, are calculated at several altitude levels, using HYSPLIT (HYbrid Single-Particle Lagrangian Integrated Trajectory) model available from the U. S. National Oceanic and Atmospheric Administration (NOAA) (Draxler & Hess, 1998), in order to determine the origin of the air masses arriving to these regions. The altitude levels chosen are 0.7, 1, 2, 2.5, 3 and 4km in order to cover a wide range of atmospheric layers potentially affected by the long-range transport of particles from African continent (as the Saharan desert dust).

The 72h air mass backward trajectories for 27, 28 and 29 May 2006 and for 06, 07 and 08 September 2007 are presented in the next chapter (Figures 3.3 and 3.4), in subsection 3.1. The air mass backward trajectories are calculated for a site within the region considered in the MesoNH simulations and considering the minimum time lag between the backward trajectories hour, the MODIS swath hour and the hour of the simulated results (see section 2.4.3).

2.4.3 Comparison with MODIS gauge data

Table 2.4 presents the selected days for this work, as well as the satellite used and the swath hour over the area under study.

The selected days are chosen taking into account the 72-hour air mass backward trajectories and the visual inspection of MODIS RGB images confirming that desert dust episodes are occurring in that days.

The region considered in the MesoNH simulations comprises the swath MODIS region and takes into account the minimum time lag between MODIS and the simulated results.

Day	Hour (UTC)	Satellite
27/05/06	12:00	Terra
28/05/06	14:20	Aqua
29/05/06	13:25	Aqua
06/09/07	14:10	Aqua
07/09/07	13:15	Aqua
08/09/07	14:00	Aqua

Table 2.4 Days selected for this work with correspondent hour and satellite

The MODIS RGB images (http://modis-atmos.gsfc.nasa.gov/IMAGES/index.html) for the selected days, 27, 28 and 29 of May 2006, are shown in Figures 3.1a, 3.1b and 3.1c for the 1200UTC, 1420UTC and 1325UTC, respectively.

Considering now Figures 3.2a, 3.2b and 3.2c, corresponding to the MODIS RGB images for days 06, 07 and 08 of September 2007 for the for the 1410UTC, 1315UTC and 1400UTC, respectively.

To assess the model ability to simulate the behaviour of desert dust aerosols in the atmosphere, the statistical index Equitable Threat Score (ETS) is computed.

The ETS gives a measure of the event forecast accuracy, usually rainfall occurrence (Gallus and Segal, 2001; Chien et al., 2002) above a certain threshold, within a certain time frame. It is defined by Schaefer (1990) as:

$$ETS = \frac{N_c - N_p N_0 / N}{N_p + N_0 - N_c - N_p N_0 / N} \tag{2.69}$$

N_c represents the number of correct modeled values above the threshold value, N_p is the number of modeled values above the threshold value, N_0 corresponds to the number of observed values above the threshold value and N is the total number of pairs of modeled and observed values.

The higher the ETS value, the better the estimation model skill is for that particular threshold. The equitable threat score can vary from a small negative number up to 1.0, where 1.0 represents a perfect modulation.

The evaluation of this established statistical skill score gives a quantitative comparison between the modeled/simulated results and the MODIS data, in this study.

In this work, the ETS is calculated for the occurrence of aerosol optical depth (AOD) and cloud optical depth (COD) values above several threshold values: 0.2, 0.3, 0.4, 0.5, 0.6, 0.7, 0.8 0.9 and 1.0 for AOD values and 5.0, 6.0, 7.0, 8.0, 9.0, 10, 11,12, 13, 14, 15 , 20 and 30 for COD values.

The Bias Score (BS) measures the tendency of the model to overestimate or underestimate an area, where the values of a certain variable are higher than a given threshold value. If the BS values are higher than 1, it means that the model tends to overestimate the occurrence of values above the considered thresholds. On the other hand, if the BS values are lower than 1, it means that the model underestimates the occurrence of values above the considered thresholds. For the discrete case this score is defined as (Anthes, 1983):

$$BS = \frac{N_p}{N_0} \tag{2.70}$$

In this work, the BS is calculated for the same threshold values as for the ETS, mentioned above.

2.4.4 Comparison with VAISALA data

To validate the cloud base height values obtained with the MesoNH model a comparison is made with the ceilometer measurements, over Évora.

Concerning convective clouds, MesoNH provides two quantities: the base height of convective clouds (CLBASCONV) and the top height of convective clouds (CLTOPCONV). The MesoNH simulated results correspond to the smallest innermost domain (10km resolution).Therefore, in order to compare the CLBASCONV modeled height with the ceilometer measured cloud base, the height of CLBASCONV, averaged over the closest area from Évora geographical site, is considered.

The ceilometer measured cloud base height values are averaged over time, considering the closest 15 minutes to the time of simulated data. The correspondent standard deviation values are also calculated.

Another used parameter for cloud studies, especially for cloud precipitation studies (Browning and Gurney, 1999), is the cloud geometrical depth of convective clouds. In this work the simulated cloud geometrical depth is estimated as the difference between the height of top of convective clouds (CLTOPCONV) and the height of base of convective clouds (CLBASCONV) measured with the ceilometer.

2.4.5 Assessment to the radiative forcing due to aerosols and clouds

In order to investigate the effect of Saharan desert dust storms on the local/regional climate, an assessment of the desert dust aerosol direct radiative forcing, shown in equation 2.51, is made.

In order to obtain the radiative fluxes in the presence of mineral desert dust the DEAD dust scheme is switched on in the MesoNH simulations and to achieve the radiative fluxes in the absence of desert dust particles the DEAD dust scheme is switched off in the MesoNH simulations.

Using the small nested area modeled (Figures 2.12b and 2.12d) for the days considered in this work the cloudy regions are removed and only the clear sky conditions are considered for the assessment of direct radiative forcing due to the desert dust aerosols.

Furthermore, with the intention of investigate the effect of different surfaces on the dust radiative forcing; two clear sky regions are selected: one region over the Atlantic Ocean, near the Continental Portugal Coast, and another region over land, in Continental Portugal. This selection is made ensuring that the aerosol optical depth (AOD) presents similar values over the land and over the oceanic regions selected, so one can assume that the aerosol type is the same, with the same properties, over both studied regions.

As for the cloud radiative forcing (equation 2.51), both the clear-sky ($F^{net}_{NO\,perturbation}$) and cloudy ($F^{net}_{perturbation}$) sky fluxes are obtained directly from MesoNH simulations.

The vertical profiles of the simulated AOD, CLDFR, COD, CLWER, CRF (SW and LW) results are obtained using the averaged results over the area of study (land and ocean regions), during the selected periods.

Concerning the vertical profiles of the aerosol and cloud properties, one has to notice the relative position of aerosols and clouds in order to properly simulate the potential interactions aerosol/cloud microphysical and optical properties, namely the radiative ones.

3. Results and Discussion

This chapter presents the results of the applications of the methodologies developed to analyze the direct and indirect effects of Desert Dust (DD) aerosols. The first section presents the verification of the DD presence in the areas and periods chosen for this study (see section 2.4). The comparisons carried out between the simulated results and VAISALA ceilometer retrievals are presented in the second section of this chapter. The following three sections present, respectively, the results obtained for the vertical profiles of some aerosol and cloud properties and the direct and indirect radiative effects of DD aerosols for the days and regions under study. The last section presents a comparison between simulated aerosol and cloud properties and the same properties retrieved by MODIS instrument.

3.1 Backtrajectories and MODIS RGB images

The MODIS RGB images (http://modis-atmos.gsfc.nasa.gov/IMAGES/index.html) for the selected days, 27, 28 and 29 of May 2006, are shown in Figures 3.1a, 3.1b and 3.1c at 1200 UTC, 1420 UTC and 1325 UTC, respectively.

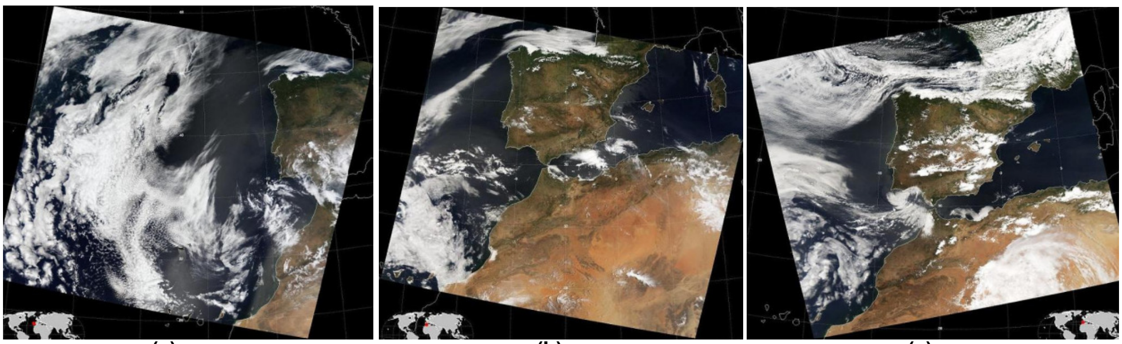

(a) (b) (c)

Figure 3.1 MODIS RGB images for 27, 28 and 29 May 2006.

From visual inspection it is possible to observe, especially in Figures 3.1a, 3.1b, that a desert dust plume is located over the Atlantic Ocean in the southwest region of the Iberian Peninsula.

Figures 3.2a, 3.2b and 3.2c show the MODIS RGB images for days 06, 07 and 08 of May 2007 at 1410 UTC, 1315 UTC and 1400 UTC, respectively.

According to Figures 3.2a, 3.2b and 3.2c it is possible to observe, that the Saharan desert dust plume enters into the southern region of the Iberian Peninsula and travels towards the Atlantic Ocean region located on the Northwest of the Iberian Peninsula.

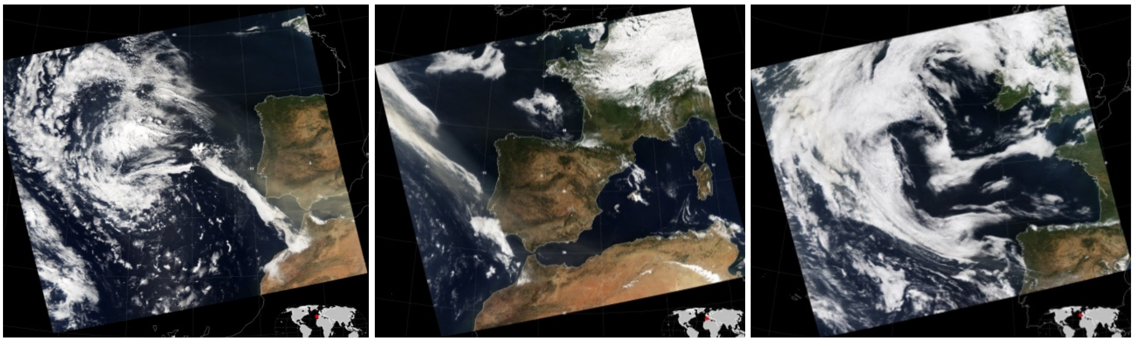

(a) (b) (c)

Figure 3.2 MODIS RGB images for 06, 07 and 08September 2007.

In order to verify the presence of Desert Dust aerosols in the atmosphere, the 72-hour air mass backward trajectories ending over selected regions of the area of study, are calculated at several altitude levels, using HYSPLIT (HYbrid Single-Particle Lagrangian Integrated Trajectory) model available from the U. S. National Oceanic and Atmospheric Administration (NOAA) (Draxler & Hess, 1998), aiming at determining the origin of the air masses arriving to the these regions.

The altitude levels chosen are 0.7, 1, 2, 2.5, 3 and 4km in order to cover a wide range of atmospheric layers potentially affected by the long-range transport of particles from African continent (as the Saharan desert dust).

Figure 3.3 shows the 72h air mass backward trajectories for 27, 28 and 29 May 2006 at 1200 UTC, 1400 UTC and 1300 UTC, respectively, for the levels chosen.

From Figure 3.3 it is also possible to observe that, for all the selected levels in the atmosphere, the air masses arriving to the Atlantic Ocean (southwest of the Iberian Peninsula) are originated directly from the North of Africa.

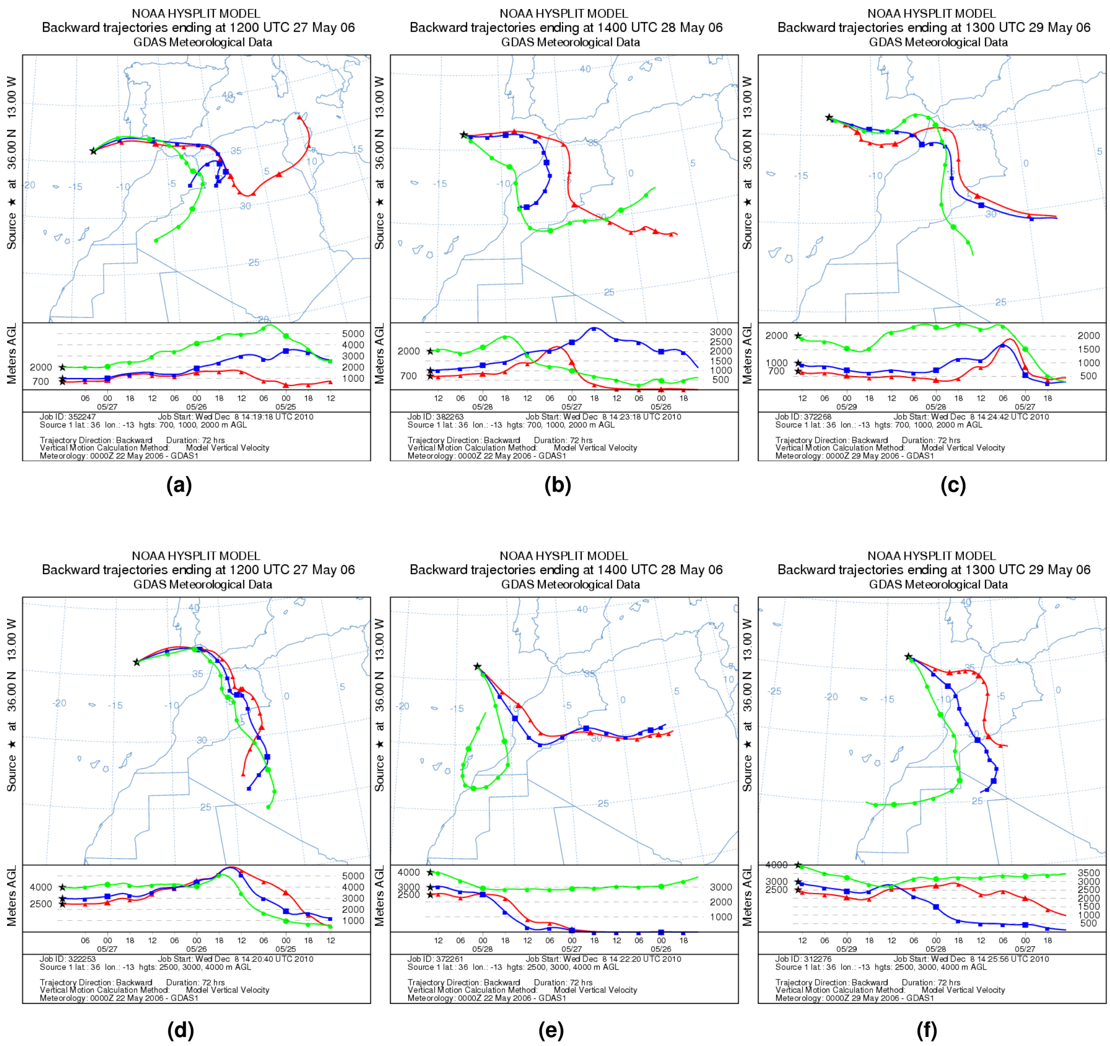

Figure 3.3 Air mass backward trajectories obtained for 27, 28 and 29 May 2006, from NOAA HYSPLIT model.

Figure 3.4 shows the 72h air mass backward trajectories for 06, 07 and 08 September 2007 at 1400 UTC, 1300 UTC and 1400 UTC, respectively, for the selected levels.

From Figures 3.4a and 3.4d, for all the selected levels, on the 06 September 2007, the plume pattern travel can be considered similar to the May 2006 DD episode, but for the 07 and 08 September 2007 (Figures 3.4b, 3.4e, 3.4c and 3.4f, respectively) the plume pattern travels in a different way. For these two days, and for higher levels in altitude (Figures 3.4e and 3.4f), the air masses come, not only from North Africa but also from the Atlantic Ocean area near to the North Africa region. This situation may implicate that, for these two days, the aerosol characteristics, which can be changed during their travel, are not the same as the ones for the DD May 2006 episode.

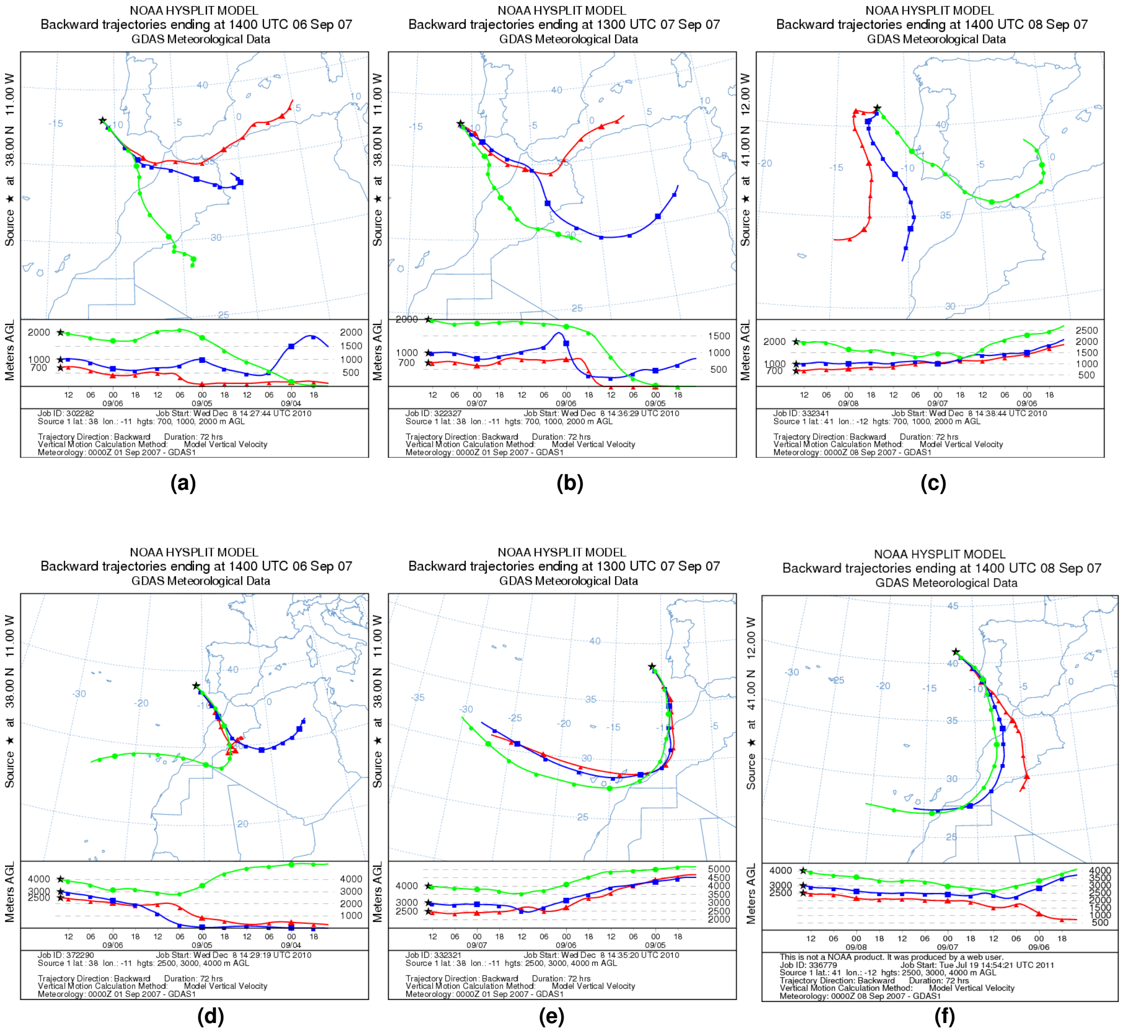

Figure 3.4 Air mass backward trajectories obtained for 06, 07 and 08 September 2007, from NOAA HYSPLIT model.

Based on the 72h air mass backward trajectories it is possible to verify that for all the selected days, and for the majority of the selected levels in the atmosphere, the air masses arriving to the region selected for this work are originated in the North of Africa were the Sahara desert is located. In that case, it is feasible to confirm that the atmosphere in the regions under study contains mineral desert dust aerosols.

3.2 Ceilometer Results Verification

For this particular study, the region selected is the area around Évora city in Continental Portugal. On days 27 and 28 May, low and medium altitude clouds were observed in the afternoon, while in the other days selected for this work, only very few clouds were observed over the region of study. Therefore only the results referring to 27 and 28 May will be analysed and compared with the simulated data obtained from MesoNH. Figures 3.5a and 3.5b show the ceilometer backscattering measurements for 27 and 28 May 2006, respectively, from 0:00 to 24:00 UTC, in Évora.

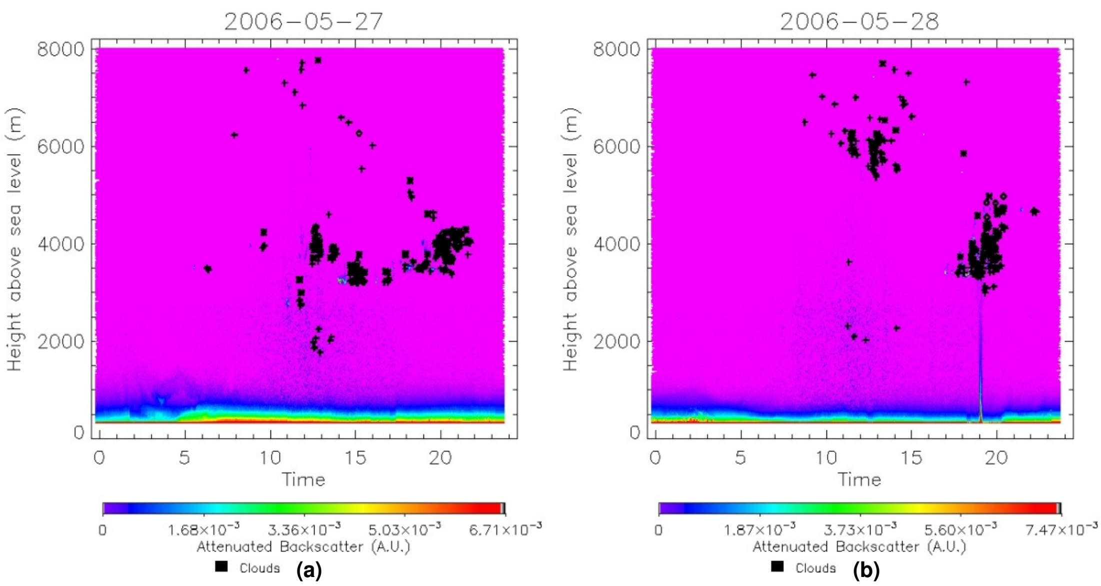

Figure 3.5 CL31 ceilometer backscatter coefficient measurements taken in Évora on 27 (a) and 28 (b) May 2006, from 0:00 to 24:00.

From Figures 3.5a and 3.5b it is noted that in this period, most of the clouds occurred in the afternoon. Between 18:00 and 22:00 UTC it is possible to observe, particularly on 28 May, the formation of clouds. For that reason the time interval between 18:00 and the 22:00 UTC was selected for both days.

Concerning convective clouds, MesoNH provides two important parameters: the base height of convective clouds (CLBASCONV) and the top height of convective clouds (CLTOPCONV). Figures 3.6 and 3.7 show the hourly CLBASCONV simulated results obtained for 27 and 28 May, respectively, between 18:00 and 22:00 UTC. The MesoNH simulated results correspond to the smallest innermost domain (10km resolution) (Figure2.12).

According to Figure 3.6, it is possible to observe that the model simulates the development of convective clouds over different regions, namely over the Atlantic Ocean, the Atlas region in North Africa and the south of Iberian Peninsula. The convective clouds that are formed over the oceanic region are more persistent in the same geographical area, than over land, particularly over the Iberian Peninsula where the formation, development and dissipation of clouds occur in a shorter time interval, probably because of the heating of the ground surface.

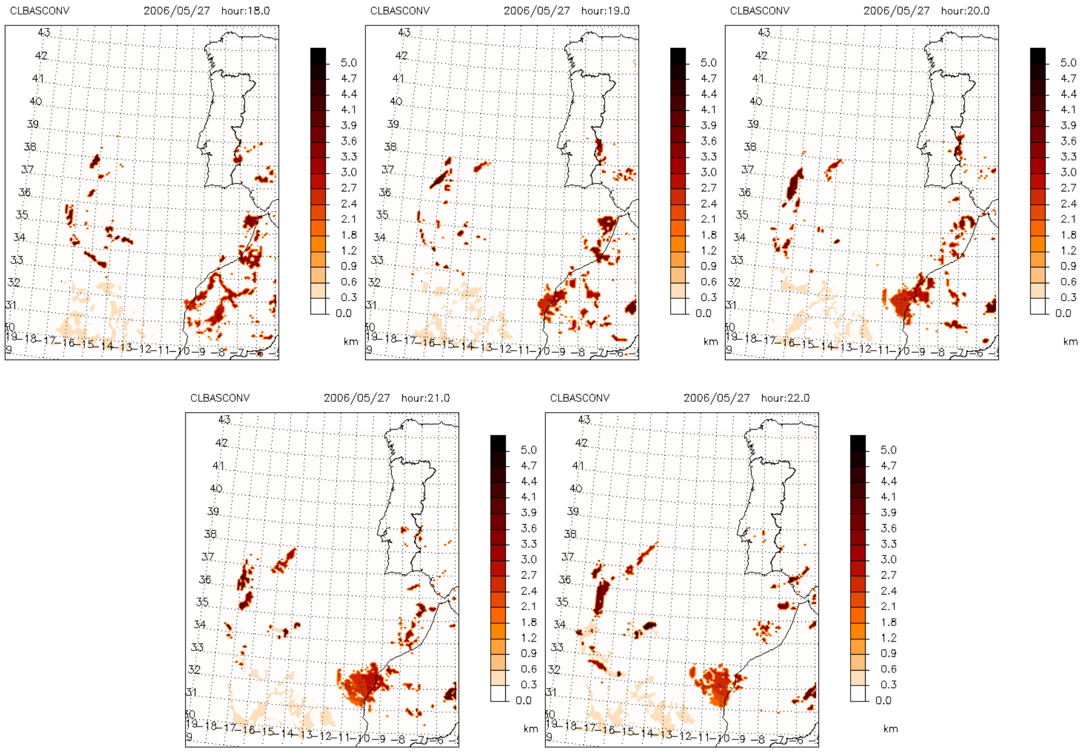

Figure 3.6 Simulated hourly base height of convective clouds, over Portugal and nearby Atlantic Ocean, for 27 May 2006, between 18:00 and 22:00 UTC.

On 28 May 2006, according to Figure 3.7, it is possible to observe that, for both continental and oceanic regions, the convective clouds are more confined to the same geographical regions as compared to the previous day and their occurrence, particularly over the Iberian Peninsula, seem to reduce from 18:00 to 22:00 UTC.

It can be noticed that the modeled convective clouds are not positioned over Évora. On 27 May (Figure 3.6) the convective clouds are located east of Évora area, and on 28 May (Figure 3.7) the clouds are situated in the Center/North of Portugal. Therefore, in order to compare the CLBASCONV modeled height with the ceilometer measured cloud base, the height of CLBASCONV, averaged over the closest area from Évora geographical site, was considered.

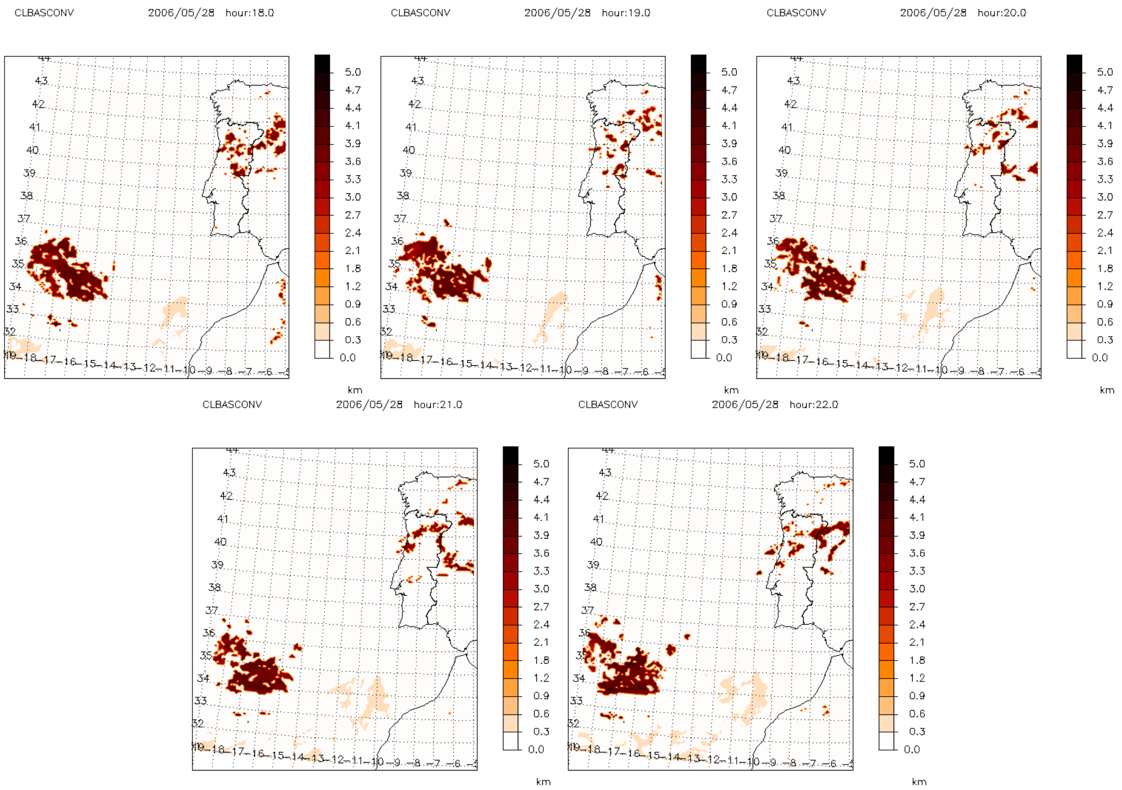

Figure 3.7 Simulated hourly base height of convective clouds, over Portugal and nearby Atlantic Ocean, for 28 May 2006,between 18:00 and 22:00 UTC.

Tables 3.1 and 3.2 present the CLBASCONV simulated height values and the ceilometer measured cloud base height values for 27 and 28 May 2006, respectively. The ceilometer measurements were averaged over time, considering the closest 15 minutes to the time of simulated data. The correspondent standard deviation values are also presented in both Tables.

27 May 2006	Ceilometer Cloud Base Height (km)	Simulated Convective Cloud Base Height (km)
18:00 UTC	3.5 ± 0.5	3.3 ± 0.3
19:00 UTC	3.5 ± 0.5	3.3 ± 0.5
20:00 UTC	3.8 ± 0.5	3.4 ± 0.2
21:00 UTC	4.0 ± 0.9	3.5 ± 0.2
22:00 UTC	4.0 ± 0.2	3.6 ± 0.2

Table 3.1 CL31 ceilometer measured cloud base height and simulated convective cloud base height for 27 May 2006.

For 28May (Table 3.2), around 21:00 UTC, the ceilometer did not detect any cloud, although the corresponding simulated value height of CLBASCONV is presented.

28 May 2006	Ceilometer Cloud Base Height (km)	Simulated Convective Cloud Base Height (km)
18:00 UTC	3.4 ± 0.6	3.6 ± 0.4
19:00 UTC	3.4 ± 0.6	3.5 ± 0.7
20:00 UTC	3.6±1.6	3.4 ± 0.8
21:00 UTC	-	3.5 ± 0.8
22:00 UTC	4.7 ± 0.2	3.5 ± 0.8

Table 3.2 CL31 ceilometer measured cloud base height and simulated convective cloud base height for 27 May 2006.

From the comparison of results shown in tables 3.1 and 3.2, it is possible to observe that although the model slightly dislocates geographically the locations of the convective clouds (Figures 3.6 and 3.7), the modeled cloud base height values seem to be in quite good agreement with the correspondent VAISALA Ceilometer measurements. These results encourage analyzing other situations and more days are already planned to be investigated.

Another important parameter for cloud studies, especially for cloud precipitation studies (Browning & Gurney, 1999), is the cloud geometrical depth of convective clouds. In this study the simulated cloud geometrical depth was estimated as the difference between the top height of convective clouds (CLTOPCONV) and the base height of convective clouds (CLBASCONV).

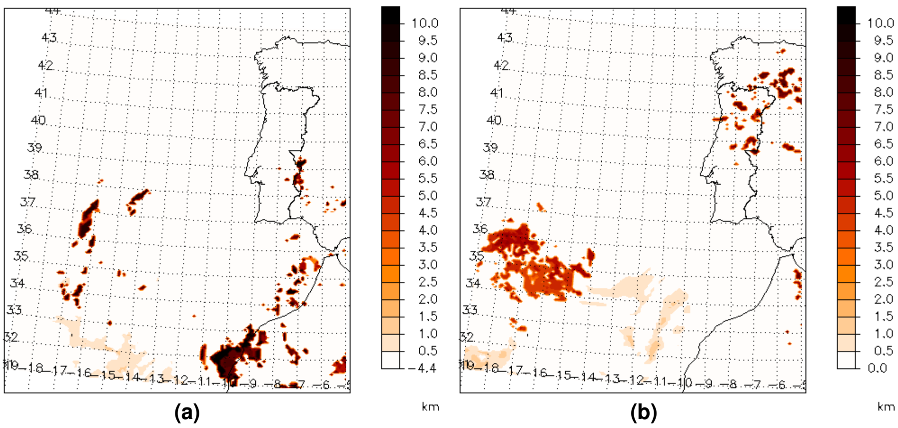

Figure 3.8 Simulated cloud depth of convective clouds over Portugal and nearby Atlantic Ocean for 27 May 2006 (a) and 28 May 2006 (b).

Figures 3.8a and 3.8b show an example of the cloud geometrical depth estimated results obtained for 27 and 28 May, respectively. To note that, in continental regions (Iberian Peninsula and Northern Africa) the cloud geometrical depth values found are greater than the cloud geometrical depth values found over the Atlantic Ocean region.

Table 3.3 shows the results obtained for the estimation of cloud geometrical depth values, averaged over the closest area from Évora geographical site, between 18:00

and 22:00 UTC. The model predicts, for the 27th May, the development of deep convective clouds late in the afternoon (18:00) and that its thickness decreases as night approaches. Further investigation is needed and comparisons with combined satellite and ceilometer data may be of great value.

27 May 2006	Simulated Convective Cloud Geometrical Depth (km)	28 May 2006	Simulated Convective Cloud Geometrical Depth (km)
18:00 UTC	7.0 ± 1.0	18:00 UTC	6.7 ± 1.3
19:00 UTC	6.9 ± 1.0	19:00 UTC	6.8 ± 1.2
20:00 UTC	6.5 ± 0.8	20:00 UTC	6.7 ± 1.3
21:00 UTC	6.1 ± 0.8	21:00 UTC	6.5 ± 1.3
22:00 UTC	5.8 ± 0.7	22:00 UTC	6.0 ± 1.2

Table 3.3 Cloud geometrical depth estimated results for 27 (left) and 28 (right) May 2006.

3.3 Desert Dust Aerosol Direct Radiative Forcing

The modeled cloud fraction is presented in Figure 3.9, for 27, 28 and 29 of May 2006. Figures 3.9a, 3.9c and 3.9e correspond to the situation when DD is not considered in the MesoNH simulations (dust scheme switched off), whereas Figures 3.9b, 3.9d and 3.9f present the modeled cloud fraction in the presence of DD aerosols (dust scheme switched on).

According to Figures 3.9a, 3.9c and 3.9e, when the DD scheme is not taken into account in MesoNH calculations, the total cloud fraction, for the three days considered, is lower than the total cloud fraction in the presence of desert dust aerosols (Figures 3.9b, 3.9d and 3.9f).

The simulated results of total cloud fraction for the 27 and 28 May (Figures 3.9b and 3.9d) seem to be in a good agreement with the actual situation (represented by MODIS RGB images in Figures 3.1a and 3.1b). Nevertheless, for 29 May 2006 (Figures 3.9e and 3.9f), the simulated results obtained seem to overestimate the cloud fraction values (comparing with the MODIS RGB images in Figure 3.1c), particularly when desert dust aerosols are considered in the simulations.

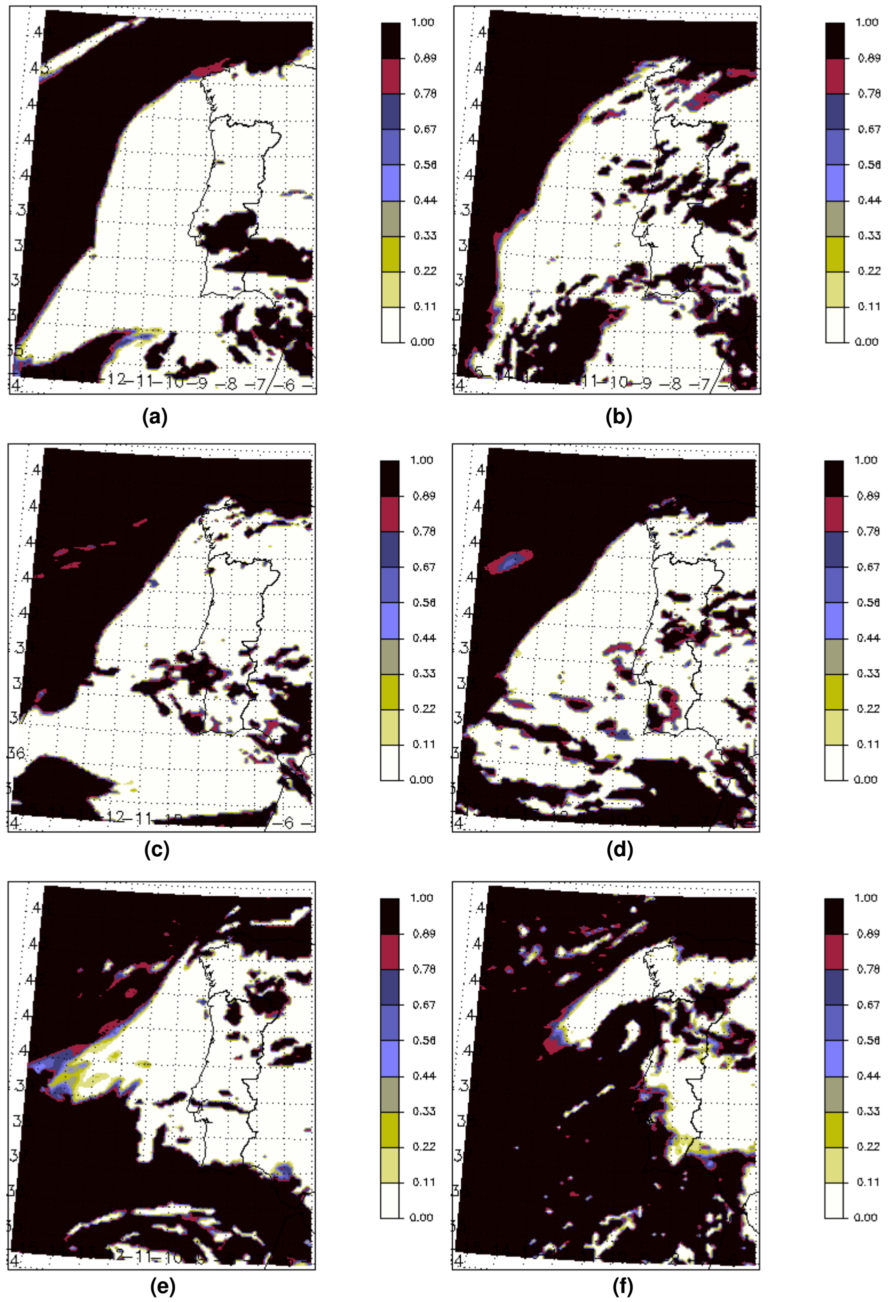

Figure 3.9 Simulated total cloud fraction in the absence of desert dust aerosols (a,c,e) and in their presence (b,d,f), for 27, 28 and 29 May 2006.

Figures 3.10a, 3.10c and 3.10e show the modeled cloud fraction, for days 06, 07 and 08 of September 2007, when desert dust is not considered, respectively, and the modeled cloud fraction in the presence of desert dust aerosols is presented in Figures 3.10b, 3.10d and 3.10f.

Comparing with the MODIS RGB images in Figures 3.2a, 3.2b and 3.2c, the simulated results of total cloud fraction for the 06, 07 and 08 September (Figures 3.10b, 3.10d and 3.10e) seem to overestimate the cloud fraction values, especially for 06 September. Nevertheless, for 07 and 08 September (Figures 3.10d and 3.10e) the cloud pattern can be considered in agreement with the actual situation represented by MODIS RGB images (Figures 3.2a, 3.2b and 3.2c).

In general, when desert dust scheme is not taken into account in MesoNH calculations, the total cloud fraction is lower than the corresponding values in the presence of desert dust aerosols. An exception to this occurs for 06 September (Figures 3.10a and 3.10b), where the presence of DD aerosols seems to induce a decrease of the total cloud fraction.

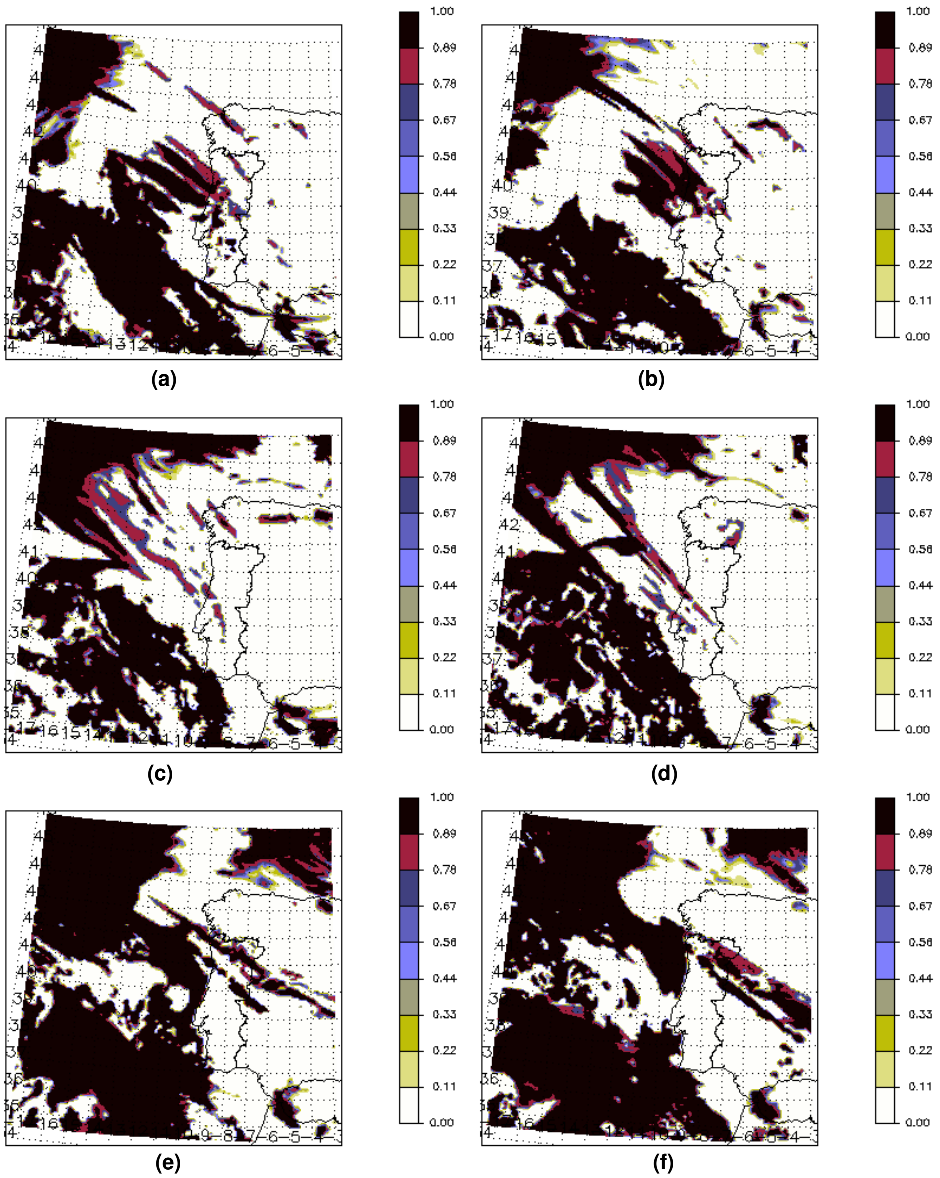

Figure 3.10 Simulated total cloud fraction in the absence of desert dust aerosols (a,c,e) and in their presence (b,d,f), for 06, 07 and 08 September 2007.

The simulated aerosol optical depth (AOD), at 0.55µm, in the dust simulation, for the 27 (1200 UTC), 28 (1400 UTC) and 29 (1300 UTC) May is presented in Figures 3.11a, 3.11c and 3.11e, respectively, for all sky conditions. The UTC hour chosen for the simulated results corresponds to the minimum time lag between MODIS and the simulated results.

Figures 3.11b, 3.11d and 3.11f present the simulated AOD values considered for clear sky conditions, on 27, 28 and 29 May 2006, respectively.

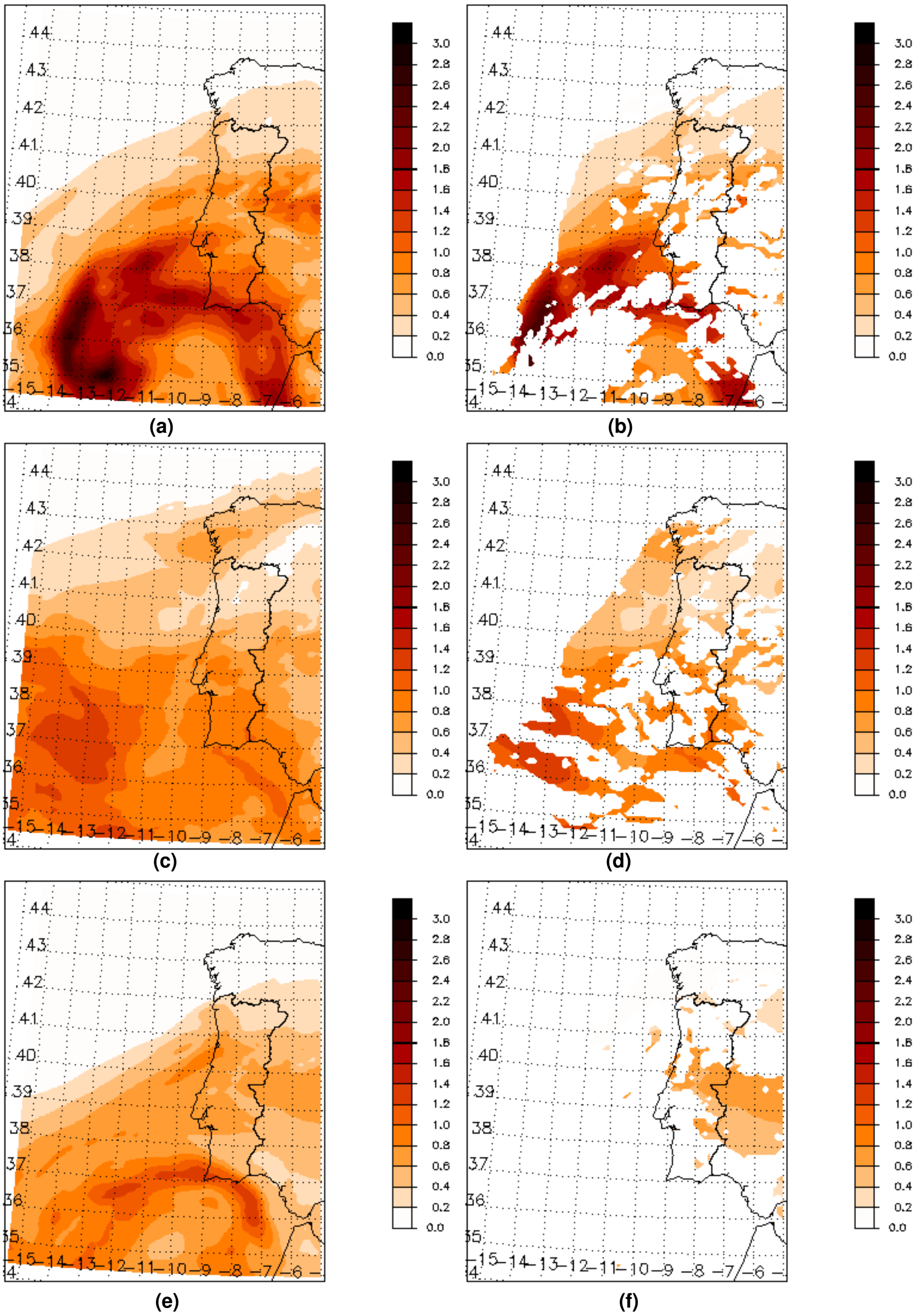

Figure 3.11 Simulated aerosol optical depth (AOD) for all sky conditions (a, c, e) and considering only the clear sky areas (b, d, f) for 27, 28 and 29 May 2006.

According to Figure 3.11a, on 27 May the AOD values are higher than the AOD values for 28 and 29 of May (Figures 3.11c and 3.11e). From Figures 3.11a, 3.11c and 3.11e, it can be observed that the dust plume, with its source in the North of Africa, travels through the South of Continental Portugal and Atlantic Ocean, dispersing all over the center of Continental Portugal and towards Madeira Island, according to the air mass trajectories analyzed (Figure 3.3).

Figures 3.12a, 3.12c and 3.12e show the simulated AOD), at 0.55µm, in the dust simulation, for the 06 (1400 UTC), 07(1300 UTC) and 08 (1400 UTC) September 2007, respectively.

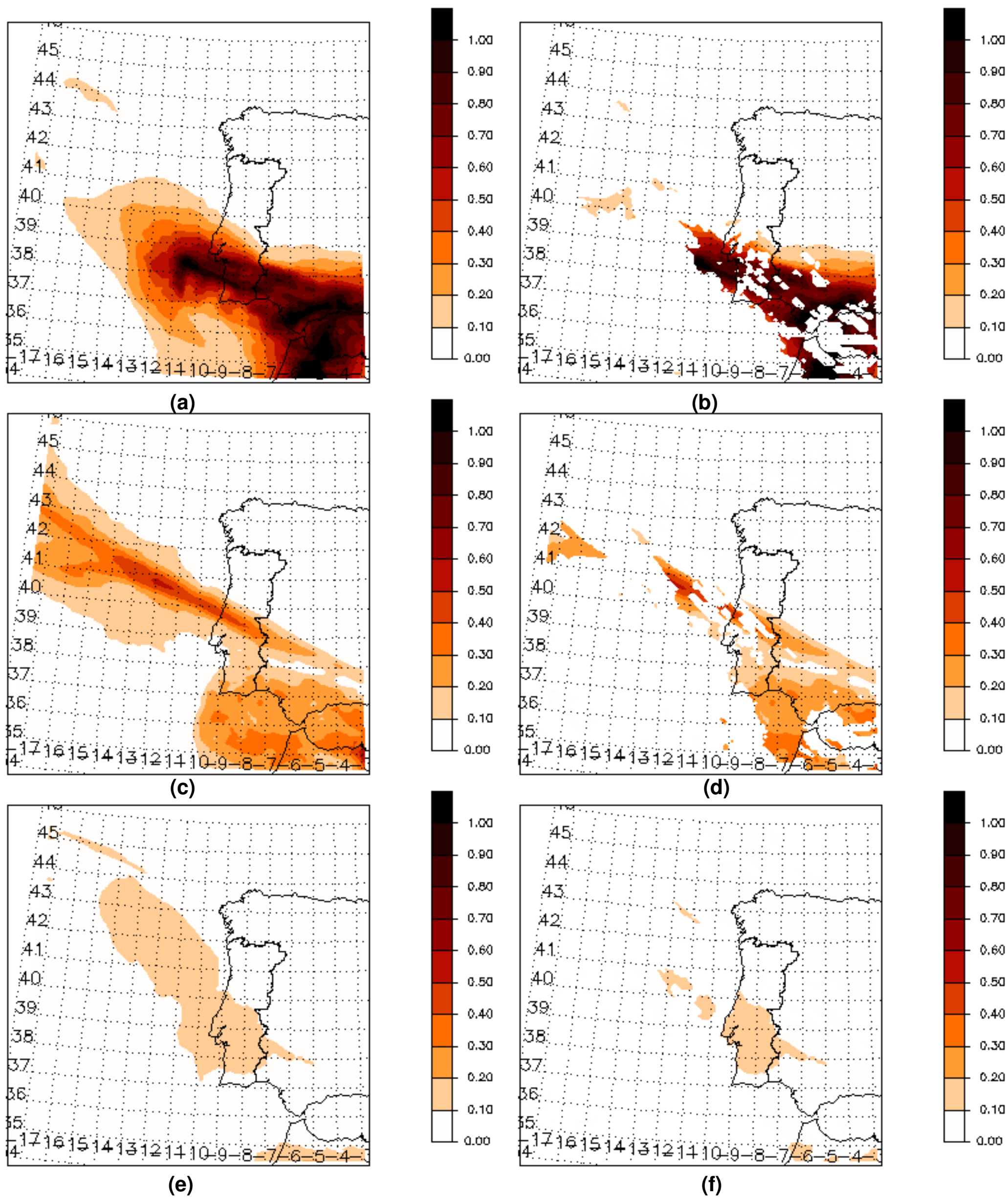

Figure 3.12 Simulated aerosol optical depth (AOD) for all sky conditions (a, c, e) and considering only the clear sky areas (b, d, f) for 06, 07 and 08 September 2007.

The simulated dust plume (Figures 3.12a, 3.12c and 3.12e) travels to the South of the Iberian Peninsula and towards the Northeast of the Iberian Peninsula, in accordance with the air mass trajectories calculated (Figure 3.4).

Figures 3.12b, 3.12d and 3.12f present the simulated AOD values considering only clear sky conditions, on 06, 07 and 08 September, respectively, which will be used subsequently for the assessment of the direct radiative forcing due only to desert dust aerosols.

In order to investigate the radiative effects of Saharan desert dust storms, an assessment of the desert dust aerosol direct radiative forcing, calculated according to equation 2.51, is made. With this purpose, the cloudy regions are not considered and the assessment of desert dust radiative forcing is therefore only made for clear sky conditions.

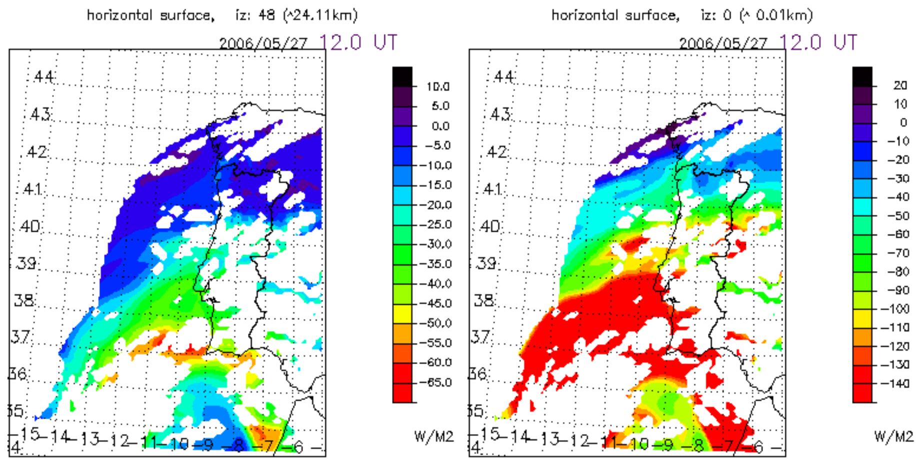

(a) (b)

Figure 3.13 TOA (a) and Surface (b) SW radiative forcing for 27 May 1200UTC.

Figures 3.13, 3.14 and 3.15 show the SW radiative forcing (SWF) and Figures 3.16, 3.17 and 3.18 show the LW radiative forcing (LWF), at the top of the atmosphere TOA and at the surface levels, obtained for the small nested area modeled (Figure 2.12b) for 27, 28 and 29 May 2006.

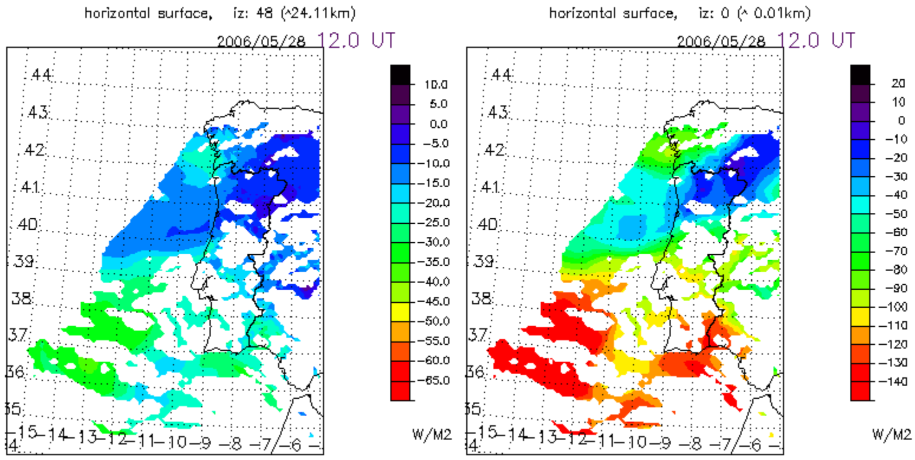

(a) (b)

Figure 3.14 Same as Figure 3.13 for 28 May 1200UTC.

Considering the SWF at the TOA (TOASWF) and at the surface (SurfSWF) for 27 and 28 May (Figures 3.13a, 3.13b, 3.14a and 3.14b, respectively), over the Iberian Peninsula and nearby Atlantic Ocean regions, it is possible to observe that the presence of desert dust aerosols in the atmosphere provokes, in the majority of the cases, a SW cooling effect both at the TOA and at the surface levels, because negative values of TOASWF and of SurfSWF are found.

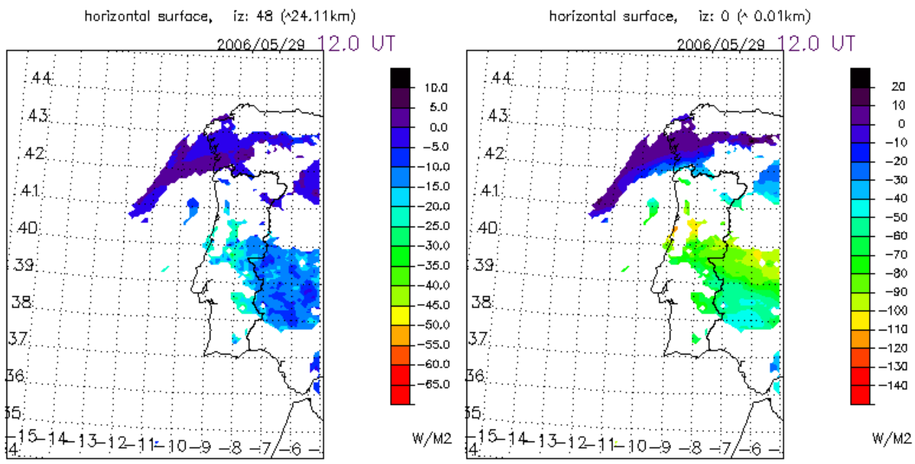

(a) (b)

Figure 3.15 Same as Figure 3.13 for 29 May 1200UTC.

Nevertheless, comparing Figure 3.13a with Figure 3.13b and Figure 3.14a with Figure 3.14b, it can be observed that this cooling effect is more pronounced at the surface level than at the TOA level, since SWF values are more negative at the surface than at the TOA.

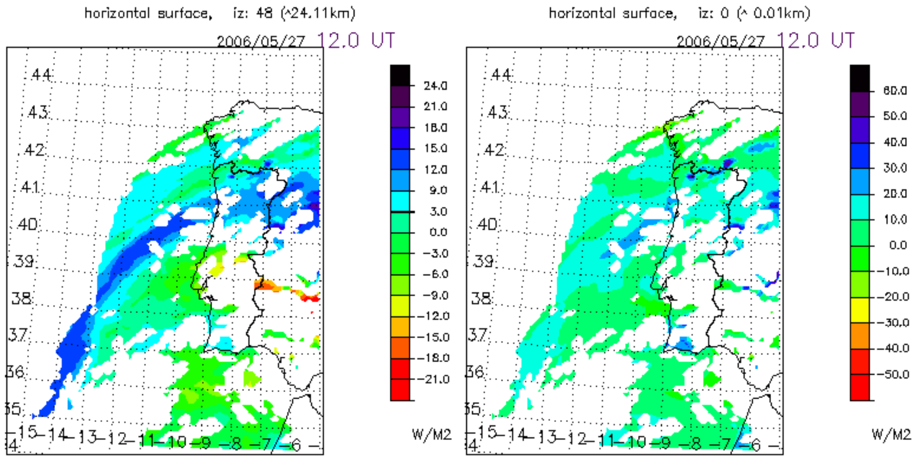

(a) (b)

Figure 3.16 TOA (a) and Surface (b) LW radiative forcing for 27 May 1200UTC.

This situation also occurs for the 29 May (Figures 3.15a and 3.15b) but not so evidently, due the fewer data available over the Iberian Peninsula and nearby Atlantic Ocean regions.

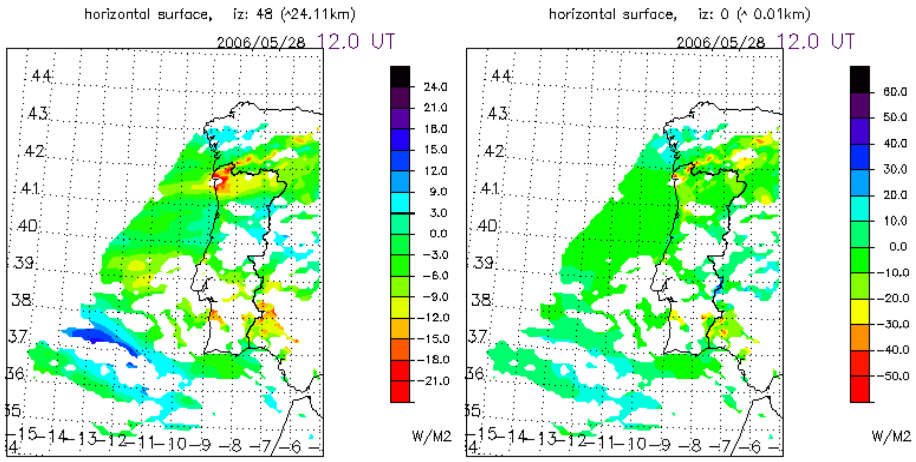

(a) (b)

Figure 3.17 Same as Figure 3.16 for 28 May 1200UTC.

Considering now the LWF at the TOA (TOALWF) and at the surface (SurfLWF) for all the days under study (Figures 3.16a, 3.16b, 3.17a, 3.17b, 3.18a and 3.18b), it can be noted that the differences are not as prominent as for the SW radiation. The TOALWF and SurfLWF simulated values are very close, for the majority of the regions.

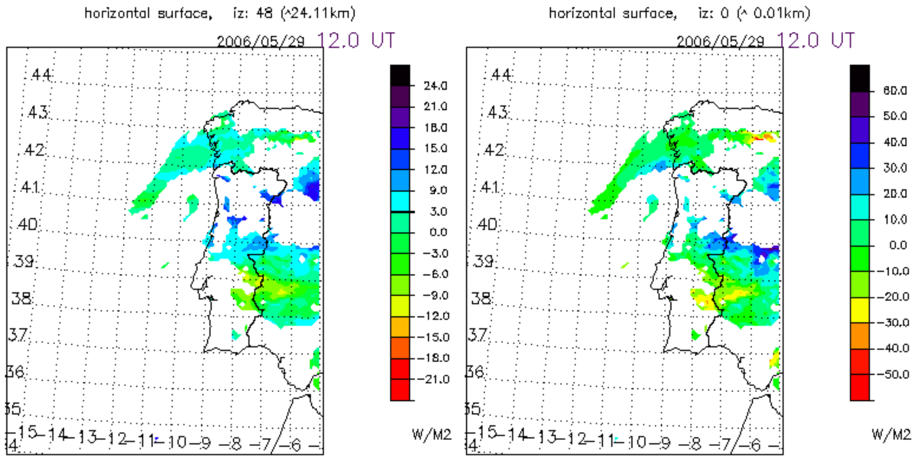

(a) (b)

Figure 3.18 Same as Figure 3.16 for 29 May 1200UTC.

Figures 3.19a, 3.19b, 3.20a, 3.20b, 3.21a and 3.21b show the TOASWF and the SurfSWF for 06, 07 and 08 September 2007, respectively.

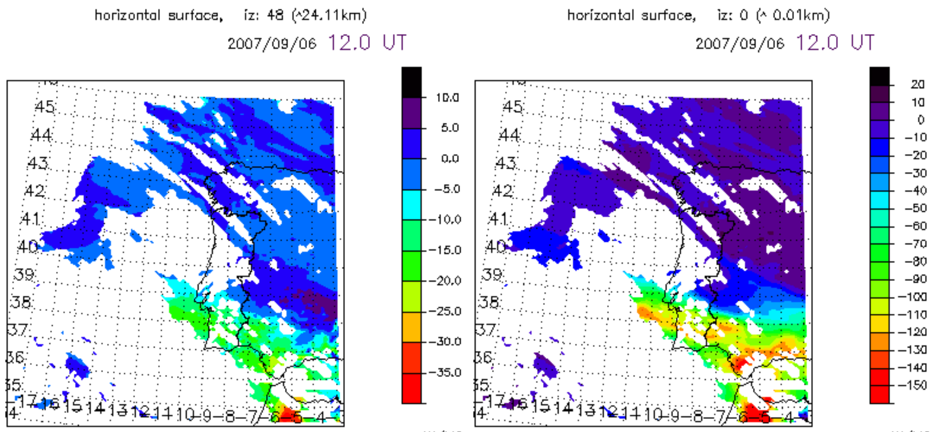

(a) (b)

Figure 3.19 TOA (a) and Surface (b) SW radiative forcing for 06 September 1400UTC.

If one observes Figures 3.19a, 3.19b, 3.20a and 3.20b, over the Iberian Peninsula and nearby Atlantic Ocean regions, it is possible to observe that the existence of desert dust aerosols in the atmosphere incites, in the majority of the cases, a SW cooling effect both at the TOA and at the surface levels, because negative values of TOASWF and of SurfSWF are mostly found.

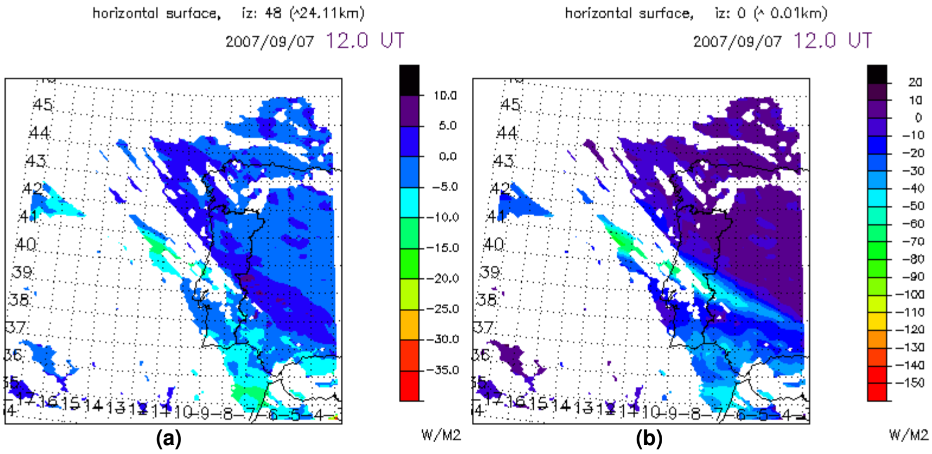

Figure 3.20 Same as Figure 3.19 for 07 September 1300UTC.

Once again, observing Figure 3.19a with Figure 3.19b and Figure 3.20a with Figure 3.20b, the cooling effect is more distinct at the surface level than at the TOA level since SWF values are more negative at the surface than at the TOA.

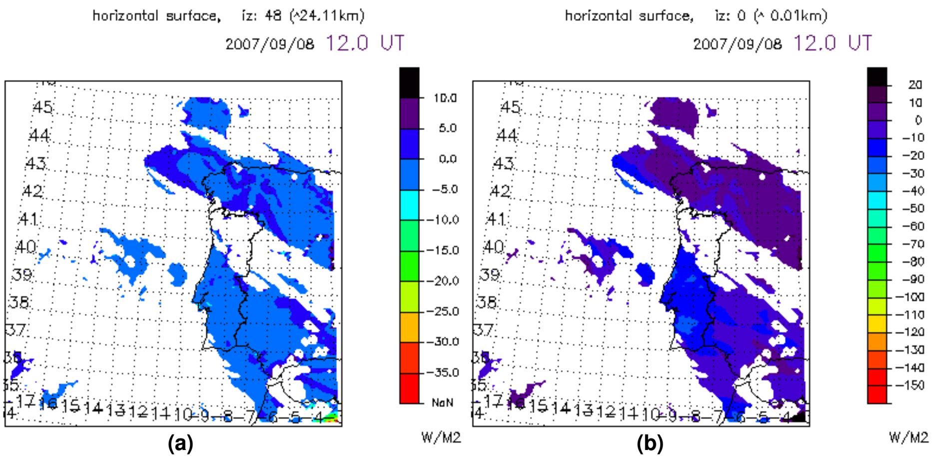

Figure 3.21 Same as Figure 3.19 for 08 September 1400UTC.

For the 08 September (Figures 3.21a and 3.21b), a cooling effect is also observed in the majority of the regions but not so evidently, due the fewer data available over Atlantic Ocean and the Iberian Peninsula regions.

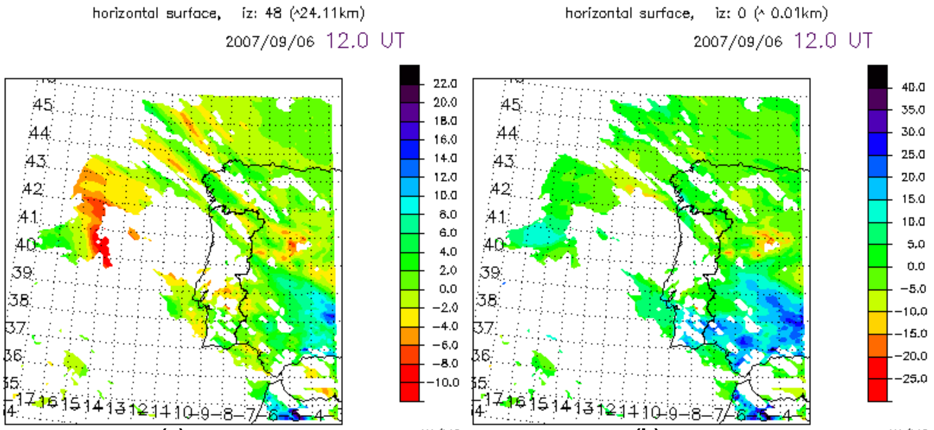

(a) (b)

Figure 3.22 TOA (a) and Surface (b) LW radiative forcing for 06 September 1200UTC.

Considering now the TOALWF and SurfLWF for the 2007 September period under study (Figures 3.22a, 3.22b, 3.23a, 3.23b, 3.24a and 3.24b), it can be noted that the level differences are not so prominent as for the SW radiation.

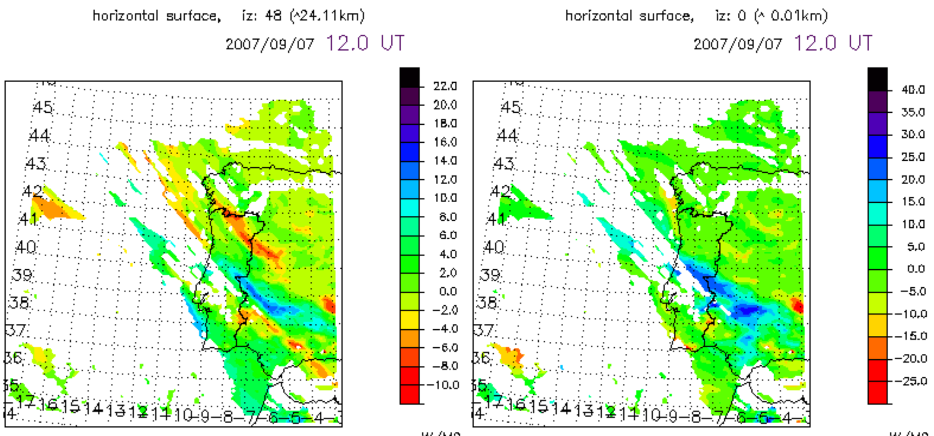

(a) (b)

Figure 3.23 Same as Figure 3.22 for 07 September 1300UTC.

The TOALWF and SurfLWF simulated values, for the September period studied, are very close, for the majority of the regions.

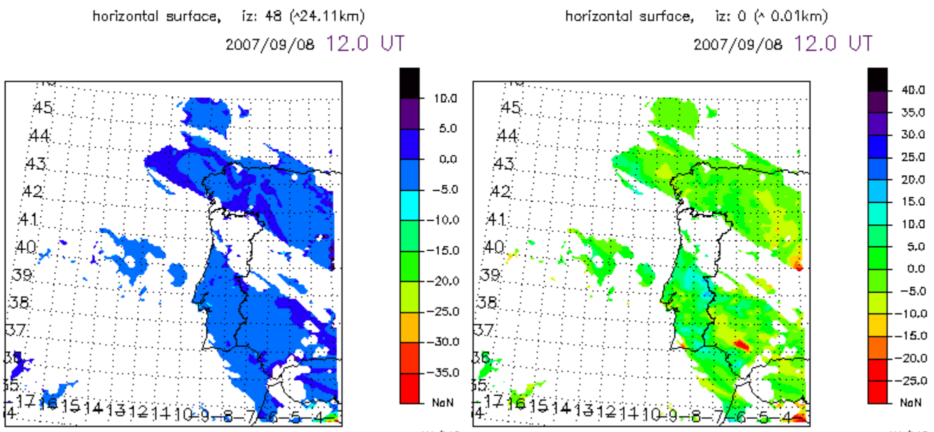

(a) (b)

Figure 3.24 Same as Figure 3.22 for 08 September 1400UTC.

A deeper discussion of the TOA and Surf aerosol radiative forcing results and the comparison with other authors can be found later in this section.

In order to investigate the effect of different surfaces with different radiometric properties on the dust radiative forcing, two clear sky regions are selected: one region over the Atlantic Ocean, near the Continental Portugal Coast, and another region over land, in Continental Portugal. This selection is made ensuring that the aerosol optical depth (AOD) presents similar values over the land and over the oceanic regions selected, so one can assess only the effect of the surface radiometric properties on the radiative forcing.

Considering the large lack of simulated clear sky results over the sea region for the 29 May, it is decided not to include this day for the subsequent studies.

Figures 3.25 and 3.26 present the simulated vertical profiles of the aerosol optical depth (Figures 3.25a and 3.26a) and desert dust aerosol SW and LW radiative forcing (Figures 3.25b and 3.26b), respectively, averaged over the area of study (land and ocean regions), during 27, 28 and 29 May 2006.

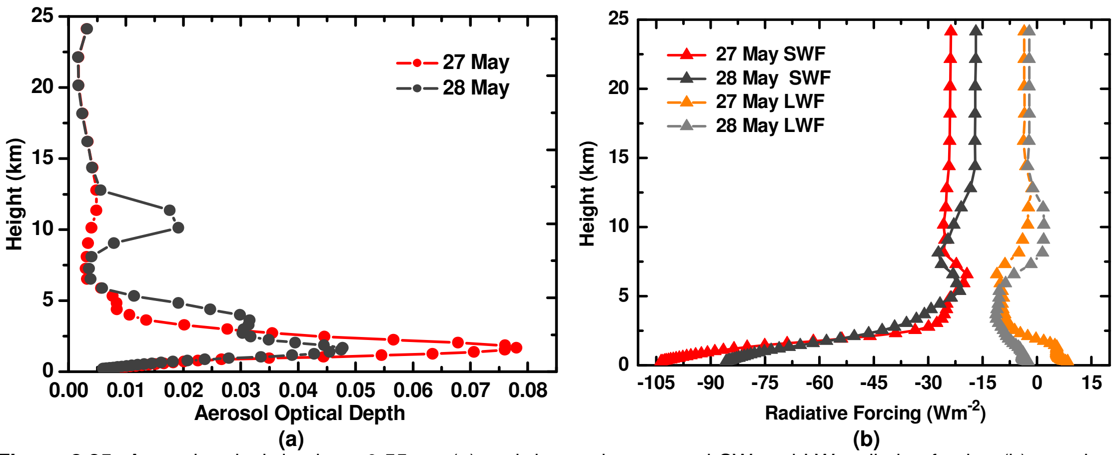

Figure 3.25 Aerosol optical depth, at 0.55µm, (a) and desert dust aerosol SW and LW radiative forcing (b) over land, for 27 and 28 May 2006.

Figure 3.25a shows the AOD values found, for 27 and 28 May, over the land region. On the 27 May, a maximum averaged AOD value of 0.08 is found and on 28 May the maximum AOD value found is 0.05, in accordance with the fact that the desert dust event was more effectual on the 27 of May, starting then to disperse.

Considering Figure 3.25b, over the land area, it is possible to observe that, for the SW radiative forcing (SWF), on the 27 May, lower values (stronger cooling) are found (SWF averaged value of -103 W/m^2 at the surface and -24 W/m^2 at the TOA) compared with the corresponding values for 28 May (SWF averaged value of -86 W/m^2 at the surface and -17 W/m^2 at the TOA). This difference can be related to the fact that the AOD values found for 27May are higher than the corresponding ones for the 28 May.

For the LW radiative forcing (LWF) at the surface level (Figure 3.25b), a warming LW effect is found for the 27 May, but for 28 May a cooling LW effect is found. Actually, the negative SW radiative forcing at the surface induces a decrease of the surface temperature and therefore reduces the earth's LW emission (Tegen et al., 1996). On the other hand, the dust absorption at thermal wavelengths contributes to the greenhouse warming. The balance between the two effects may depend on the vertical structure of aerosol concentration. So, the difference in the sign of the simulated aerosol LW forcing between the two days may be related to the fact that the AOD values on 27 May near the surface ($Z < \sim 2.5\,km$) are higher than the corresponding AOD values on 28 May. Nevertheless, the LWF values in altitude ($Z > 15\,km$), have a tendency to approximate and, at the TOA, the values are very close (-3 W/m^2 for 27 May and -2 W/m^2 for 28 May), also because, the dust layer is located well below ($Z \approx 10\,km$).

Over the sea region, regarding now Figure 3.26b, it is possible to observe, on the 27 May, for most of the entire column, a LW warming effect (positive LWF values) and on the 28th May, below 5km altitude, a LW cooling effect (negative LWF values) is observed. Nevertheless, for this day, as the altitude increases, the LWF values tend to - 4 W/m^2 and, for the 27 May the corresponding LWF values come near 1 W/m^2.

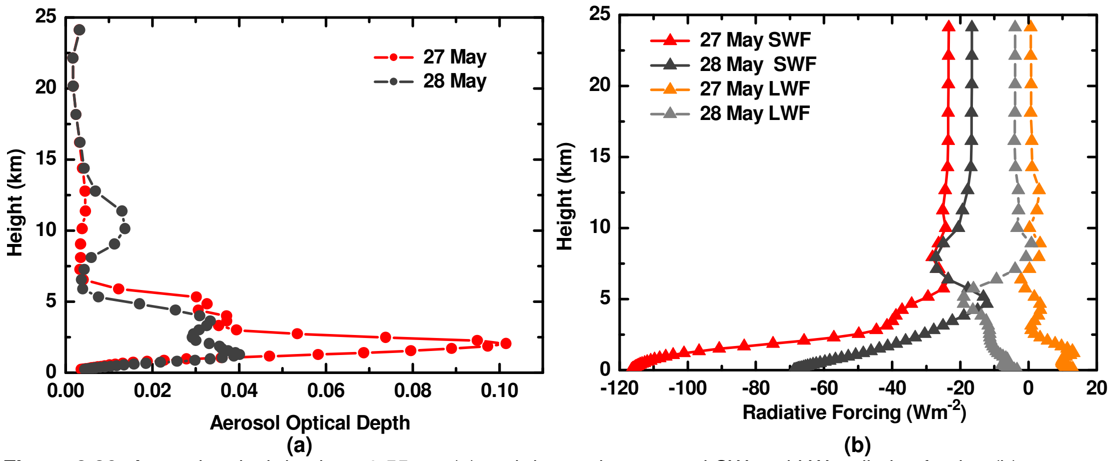

Figure 3.26 Aerosol optical depth, at 0.55µm, (a) and desert dust aerosol SW and LW radiative forcing (b) over ocean, for 27 and 28 May 2006.

Considering Figure 3.26b, for the SW radiative forcing (SWF), lower values are found again on the 27th May (SWF averaged value of -23 W/m^2 at TOA and -116 W/m^2 at the surface) compared with the corresponding values on the 28 May (SWF averaged value of -17 W/m^2 at TOA and -69 W/m^2 at the surface). This difference can, once again, be related to the fact that near the surface ($Z < \sim 2.5\,km$) the AOD values (Figure 3.26a), are higher (maximum averaged value of 0.1), on 27 May, than the AOD values on the 28 May (maximum averaged value of 0.04).

Regarding now the SWF values found for oceanic and land regions (Figures 3.25b and 3.26b, respectively) it is possible to observe that, for similar type of aerosols and aerosol loads (similar AOD values found in Figures 3.25a and 3.26a), over sea region, the average SWF simulated values, at the surface (-116 W/m^2), are more negative than the corresponding values found over the land region (-103 W/m^2), for the 27 May. This may be related to the fact that, the averaged AOD values over ocean are slightly higher than the corresponding values found over land, meaning that, if more desert dust diffusing aerosols are present over ocean, they will reflect more SW radiation backwards. Furthermore if over the ocean there is likely an hygroscopic growth effect of the aerosols due to higher relative humidity compared with the one that may be found over the land they will reflect more backwards over the ocean than over the land. However, when one looks at 28 May, the SWF values over the sea region, at the surface, are less negative than the corresponding values found over the land region. Taking into account that the AOD values found for this day, don’t differ much between over the sea and over the land region (Figures 3.25a and 3.26a). This difference in SWF values may only be explained by the different radiometric properties of the underlying surface (surface albedo). The land surface, which in this case is forest vegetation, reflects more SW than the ocean surface, meaning then, for almost the same AOD values, a more negative SWF is found over land. As for the TOA SWF values, presented before, for both days and both regions, it is possible to observe that, the underlying surface does not appear to have a great impact on the estimation of the TOA SWF. The effect of the underlying surface doesn’t seem, apparently, to interfere in the estimation of LWF at TOA (Figures 3.25b and 3.26b) both over sea as well as over land regions. This could be related to the fact that the surface emissivity of the land region considered, which is about 90% (for forest type), don’t differ much of the surface emissivity of the ocean region, which was considered to be 92-96%.

Table 3.4 shows the summary of the average values of the direct SWF and LWF, obtained in this work, at the TOA and at the surface levels, for the days 27, 28 and 29 May 2006.

	Over Land			Over Ocean		
Forcing (Wm^{-2})	27 May	28 May	29 May	27 May	28 May	29 May
TOA SWF	-24	-17	-19	-23	-17	-21
TOA LWF	-4	-2	6	1	-4	-2
Surf SWF	-104	-86	-81	-116	-69	-74
Surf LWF	8	-2	8	11	-6	-16

Table 3.4 Simulated SW, LW aerosol radiative forcing, at TOA and surface (Surf) levels, for 27, 28 and 29 May 2006, over land and ocean surfaces.

Over the Atlantic Ocean, for a Saharan dust event occurred in July 1998, Liu et al. (2003) estimate a daytime diurnally averaged direct SWF value of -15.2 W/m^2 (for a mean AOD of 0.79 ± 0.39, and wavelength of $0.63 \mu m$), at the TOA, which corresponds to an instantaneous value of - 91 W/m^2. This value is much higher than the TOA direct SWF values found in this work for May 2006 ($\approx$21 W/m^2). This difference confirms the fact that there are considerable uncertainties in estimating the radiative effects of dust aerosols, due to the fact that the net radiative forcing at the TOA depends on several key variables such as: the surface albedo, the particle size spectrum, the vertical distribution of the dust layers, the dust optical depth and the imaginary part of the refractive index (Tegen and Lacis 1996, Liao and Seinfeld 1998b), related with the chemical composition of the aerosols.

The TOA direct SWF values seem to be in agreement with Chen et al. (2009) who found, in the Spring 2006, for mineral desert dust in deserts in western China and southern Mongolia, a daily averaged value of –7 W/m^2 (with an AOD value of 0.1, at $0.55 \mu m$), which corresponds to an instantaneous value of - 21 W/m^2, over ocean region.

Furthermore, on May 2008, the maximum surface direct SWF found by Ge at al. (2010), over land region, was - 107 W/m^2 (with values AOD that range from 0.07 to 0.25, at $0.67 \mu m$). This value is very comparable, at least with the values found in this work on the 27 May 2006 (-104 W/m^2) where the aerosol loading reached its maximum value. For the entire spring period Ge at al. (2010) estimate a surface direct SWF mean value of -67 W/m^2, which is consistent with the direct SWF values found in this work, for a short period, but corresponding to a strong DD event (therefore more negative SWF of $\approx$-90 W/m^2).

Kim et al. (2005) also estimate, at three ground sites over East Asia (over land region), in April 2000 and April 2001, a surface direct SWF value of –117 W/m^2 (with an AOD value of 0.5, at $0.50\mu m$), which can be reasonably comparable to the simulated results, for this work, in May 2006, assuming that occurred the same aerosol loads over both sites and the underlying surface had the same radiometric properties.

Figures 3.27 and 3.28 present the simulated results obtained for the vertical profiles of the aerosol optical depth (Figures 3.27a and 3.28a) and desert dust aerosol SW and LW radiative forcing (Figures 3.27b and 3.28b), respectively, averaged over the area of study (land and ocean regions), during the September 2007 studied period.

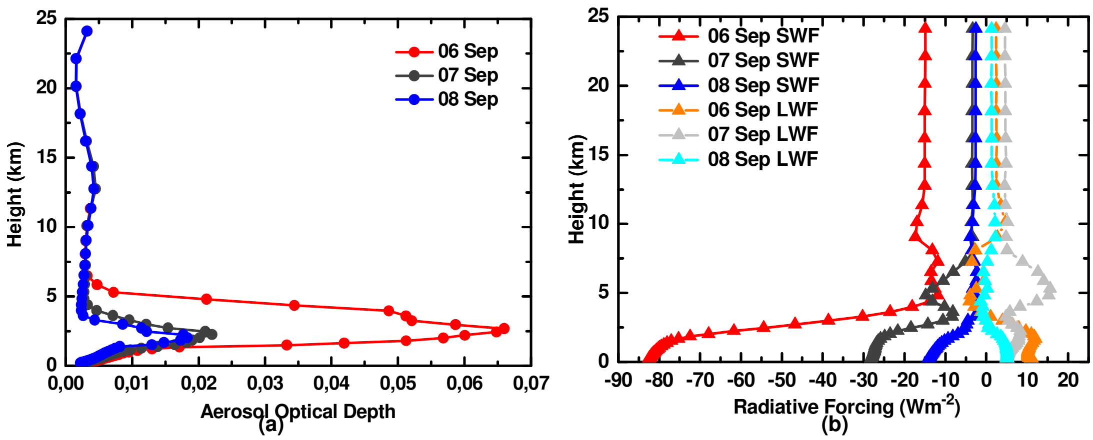

Figure 3.27 Aerosol optical depth, at 0.55µm, (a) and desert dust aerosol SW and LW radiative forcing (b) over land, for 06, 07 and 08 September 2007**.**

Figure 3.27a show the AOD vertical profile found, for 06, 07 and 08 September, over the land region whereas Figure 3.28a show the same quantity over sea region. On the 06 September, a maximum averaged AOD value of 0.07 is found, whereas on the 07 September and on 08 September a maximum averaged AOD value of 0.02 is found, in agreement with the fact that the desert dust event was stronger on the 06 September, starting then onward to dissolve.

Considering Figure 3.27b, it is possible to observe that the SWF values obtained over the land region on the 06th September (SWF averaged value of -83 W/m^2 at the surface and -15 W/m^2 at the TOA) are lower when compared with the corresponding values obtained for 07 September (SWF averaged value of -28 W/m^2 at the surface and -3 W/m^2 at the TOA) and for the 08 September (SWF averaged value of -14 W/m^2 at the surface and -2 W/m^2 at the TOA). This difference can be related, once again to the fact that the AOD values found for 06 September are higher than the ones obtained for the 07 and 08 September (Figure 3.27a).

For the LWF at the surface level as well as at the TOA (Figure 3.27b), a warming LW effect is found for all the September studied days, where the LWF values are always positive.

Considering now the SWF values simulated over the sea region on the 06th September (Figure 3.28b), lower values are found again (SWF averaged value of -14 W/m^2 at TOA and -80 W/m^2 at the surface) compared with the corresponding values obtained for 07 September (SWF averaged value of -4 W/m^2 at TOA and -34 W/m^2 at the surface) and for the 08 September (SWF averaged value of -2 W/m^2 at TOA and -9 W/m^2 at the surface). The fact that on the 06th September the AOD values (Figure 3.28a) have higher values (maximum averaged value of 0.6) than the AOD values obtained for 07 and for 08 September (maximum averaged value of 0.02), as shown in Figure 3.28a, can explain the difference in the SWF values.

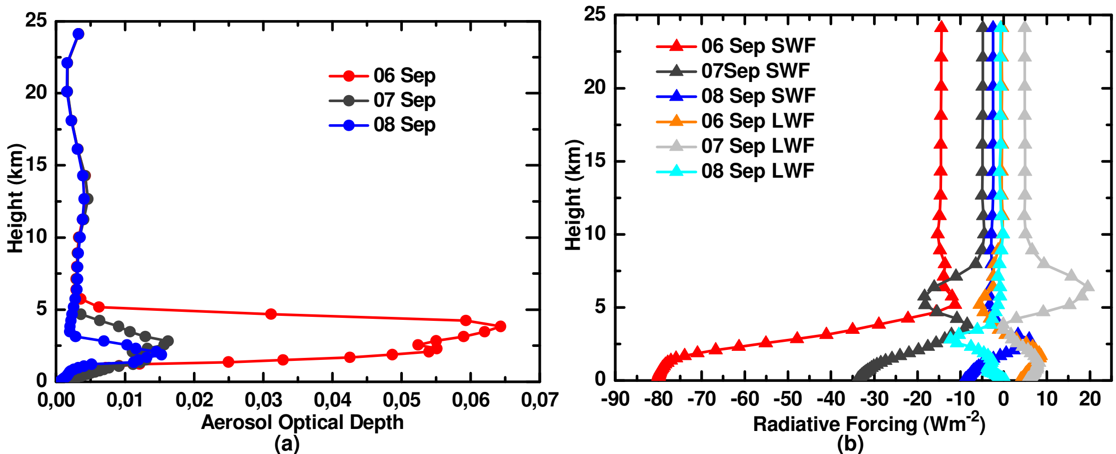

Figure 3.28 Aerosol optical depth, at 0.55µm, (a) and desert dust aerosol SW and LW radiative forcing (b) over ocean, for 06, 07 and 08 September 2007.

Regarding now the LWF values found, over the sea region, and shown in Figure 3.28b, a LW warming effect is found. On the other hand, on 08 September, and below 5km altitude, a LW cooling effect is found. Nevertheless, as the altitude increases, the LWF values, for 06 September and 08 September, tend to 0 W/m^2, meaning that the DD does not exert any radiative effects in these conditions.

Concerning now the SWF values found for land and sea regions (Figures 3.27b and 3.28b) it is possible to observe that, for similar AOD values, shown in Figures 3.27a and 3.28a (respectively, for land and sea regions), the SWF values at the surface, on the 06September and over land region, are more negative than the corresponding values found over the sea region. This may be related to the underlying surface since the AOD values don't differ much both over sea and over land. The land surface reflects more SW radiation than the ocean surface, meaning then a more negative

SWF for the same AOD values. The same situation happens for the TOA SWF values, presented before, for all days and both regions.

As for the LWF at TOA and surface levels, the effect of the underlying surface doesn't seem, in fact, to have a large impact in the estimation of LWF over sea or over land regions.

Table 3.5 shows the summary of the average values of the direct SWF and LWF, at the TOA and at the surface levels, for the days 06, 07 and 08 September 2007.

	Over Land			Over Ocean		
Forcing (Wm^{-2})	06 Sep	07 Sep	08 Sep	06 Sep	07 Sep	08 Sep
TOA SWF	-15	-3	-3	-16	-15	-3
TOA LWF	2	5	1	0	5	-1
Surf SWF	-83	-28	-14	-80	-28	-9
Surf LWF	11	5	5	4	6	0

Table 3.5 Simulated SW, LW aerosol radiative forcing, at TOA and surface (Surf) levels, for 06, 07 and 08 September 2007, over land and ocean surfaces.

As already mentioned before, Liu et al. (2003) estimate an instantaneous TOA direct SWF value of - 91 W/m^2 (for a mean AOD of 0.79 ± 0.39, and wavelength of $0.63 \mu m$), which is much higher than the TOA direct SWF values found in this work for September 2007 ($\approx$7 W/m^2). Again this difference confirms the fact that there are considerable uncertainties in estimating the radiative effects of dust aerosols (such as the direct SWF dependence on the already mentioned key variables previously).

Compared with Chen et al. (2009) who found, in the Spring 2006, for DD in western China and southern Mongolia deserts, an TOA direct SWF value of - 21 W/m^2 (with an AOD value of 0.1, at $0.55 \mu m$), over ocean region, the correspondent simulated values TOA direct SWF are slightly above (-16 and -15 W/m^2 for 06 and 07 September, respectively) the Chen et al. (2009) value. And, for the 08th September, the simulated TOA direct SWF value is very small (-3 W/m^2), compared to the TOA direct SWF value found by Chen et al. (2009).

As for the land region and comparing with the Ge at al. (2010) surface direct SWF mean value of -67 W/m^2 surface direct SWF (with values AOD that range from 0.07 to 0.25, at $0.67 \mu m$) can be comparable with the surface direct SWF values for the 06th and the 07th September (-80 W/m^2 and -28 W/m^2, respectively).

Zhang and Christopher (2003), over land region, found a monthly-mean DD TOA LWF for September 2000 of 7 W/m^2 (with an AOD of 0.55, at $0.55\mu m$), which can be acceptable compared with the simulated TOA LWF values ranging from 1 to 5 W/m^2, for 06, 07 and 08 September 2007.

3.4 Cloud Properties under the influence of desert dust aerosols

As it was already mentioned before, the analysis is made for two situations: clouds developing in a dust free atmosphere (MesoNH dust scheme not activated) and cloud developing in an atmosphere where Saharan dust particles are present (dust scheme activated).

In order to investigate the possible modifications that cloud may suffer due the presence of mineral dust aerosols in the atmosphere, the study of same cloud microphysical properties is made. From now on, the simulated results are presented taking into account the region were the DD particles interact with clouds, over the Atlantic Ocean nearby the Iberian Peninsula.

The simulated cloud optical depth (COD) in the absence of mineral dust aerosols for the two periods under study, May 2006 and September 2007, is presented in Figures 3.29a to 3.34a. The simulated COD values in the presence of DD aerosols are presented in Figures 3.29b to 3.34b, respectively for May 2006 and September 2007.

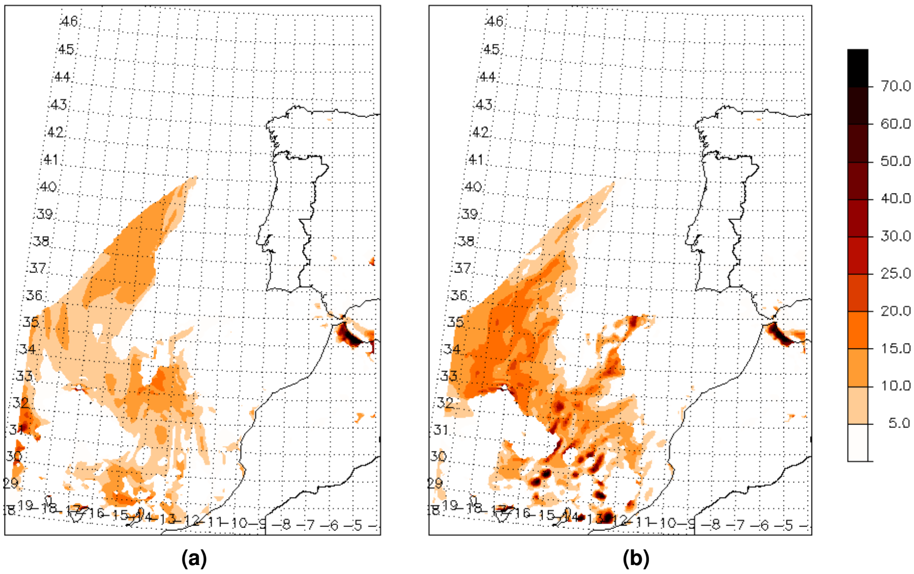

Figure 3.29 Simulated cloud optical depth (COD) in the absence (a) and in the presence (b) of desert dust aerosols and considering only the region were clouds and aerosols co-exist, for 27 May 2006.

According to Figure 3.29b, it is possible to observe that the presence of desert dust seems to increase the COD values.

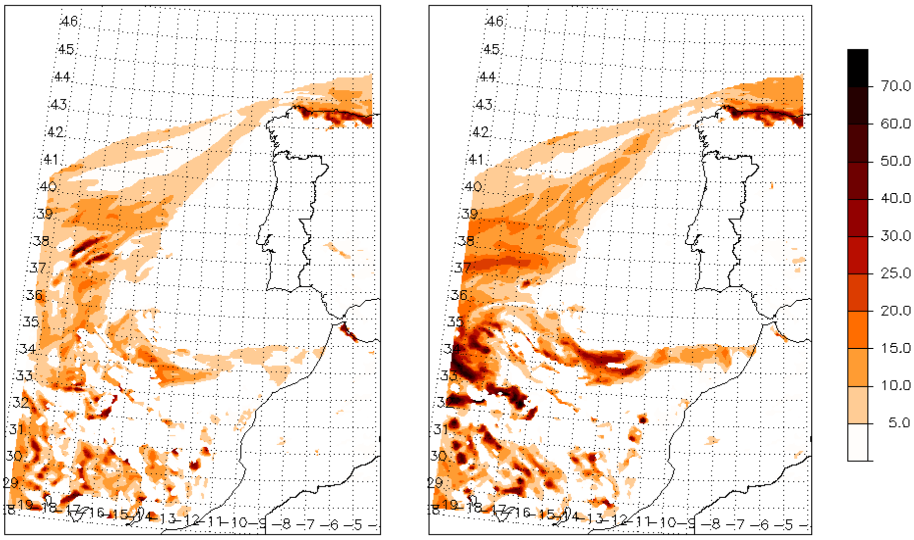

(a) (b)

Figure 3.30 Simulated cloud optical depth (COD) in the absence (a) and in the presence (b) of desert dust aerosols and considering only the region were clouds and aerosols co-exist, for 28 May 2006.

The same situation occurs for 28 May (Figure 3.30b) and for 29 May (Figure 3.31b).

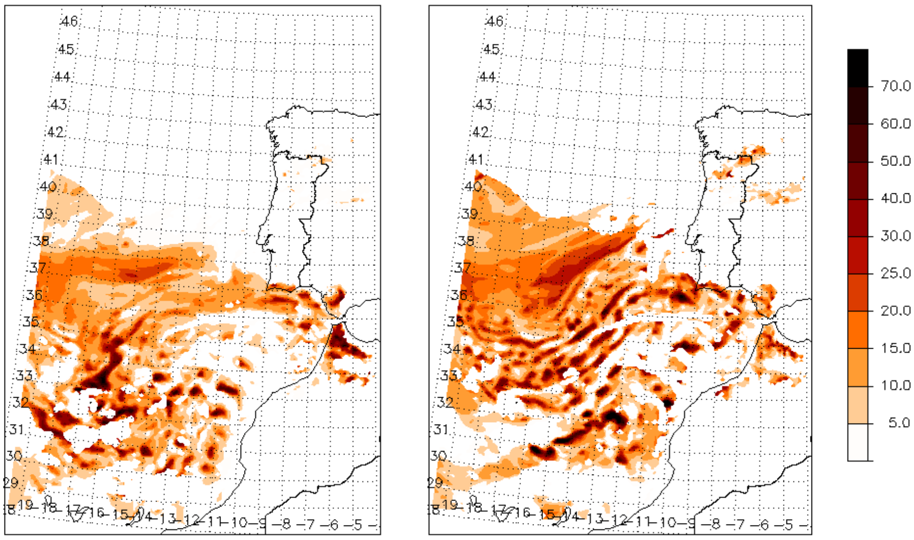

(a) (b)

Figure 3.31 Simulated cloud optical depth (COD) in the absence (a) and in the presence (b) of desert dust aerosols and considering only the region were clouds and aerosols co-exist, for 29 May 2006.

Considering now the desert dust episode that occured in September 2007, and looking again at the simulated COD values (Figures 3.32 to 3.34), the presence of mineral dust seems to have a contrary effect from the one found for the May 2006 episode, that is the presence of desert dust seems to decrease the COD values.

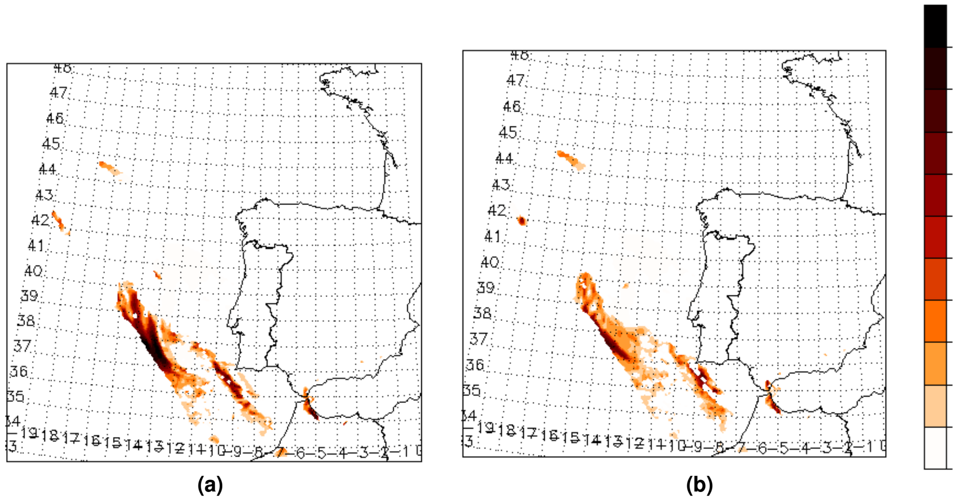

Figure 3.32 Simulated cloud optical depth (COD) in the absence (a) and in the presence (b) of desert dust aerosols and considering only the region were clouds and aerosols co-exist, for 06 September 2007.

Comparing Figures 3.32a with 3.32b, Figures 3.33a with 3.33b and Figures 3.34a with 3.34b one can notice that higher values of COD are found, in the majority of the cases, for clouds developing in an atmosphere where desert dust aerosols are not present.

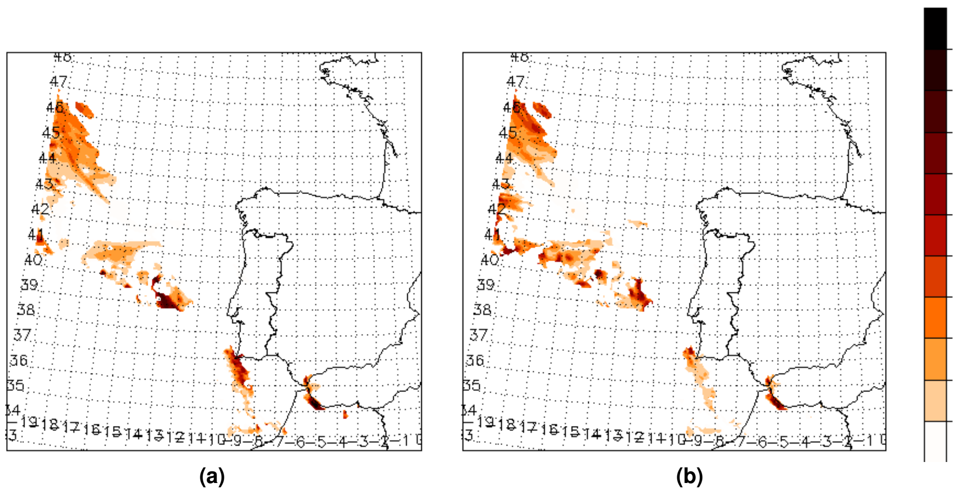

Figure 3.33 Simulated cloud optical depth (COD) in the absence (a) and in the presence (b) of desert dust aerosols and considering only the region were clouds and aerosols co-exist, for 07 September 2007.

Considering that this analysis was not much convinced, since the presence of DD aerosols is based only on information of the top of the cloud (satellite images), it was decided to analyze the vertical profile of certain cloud properties in order to have a better perception of what alterations clouds may suffer in the presence of DD aerosols.

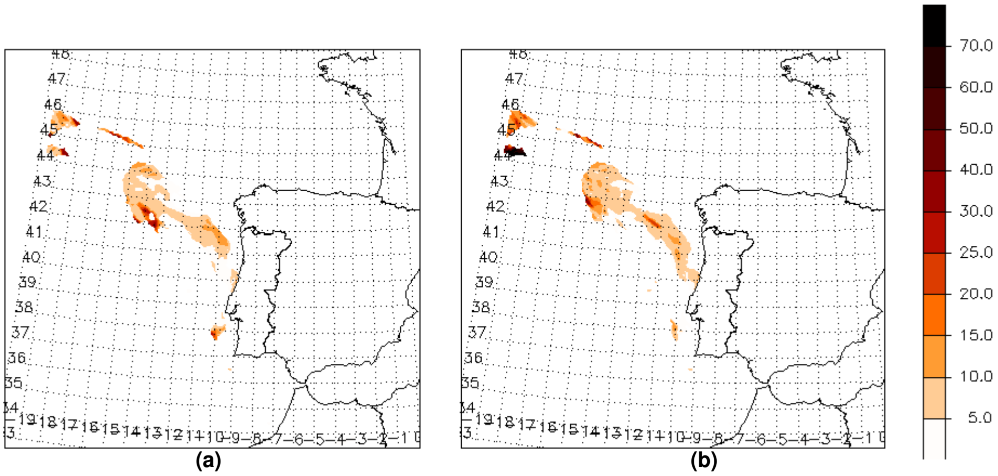

Figure 3.34 Simulated cloud optical depth (COD) in the absence (a) and in the presence (b) of desert dust aerosols and considering only the region were clouds and aerosols co-exist, for 08 September 2007.

The results obtained for the cloud properties, namely, the mean (horizontally averaged for different altitude levels) cloud liquid water effective radius (CLWER) and the mean cloud optical depth (COD), over a selected region where clouds and aerosols are present in the atmosphere, as well as the mean cloud fraction (CLDFR) and the mean aerosol optical depth (AOD) for the 27, 27 and 29 May 2006, are presented in Figures 3.35 to 3.37. These same averaged properties for 06, 07 and 08 September are presented in Figures 3.38 to 3.40.

It was verified that in all our study cases the relative position of the aerosols and clouds, are such that the aerosols layers are always above the clouds and the contamination of clouds by aerosols is done at the top of the cloud, which are always low level clouds.

For the same days and according to Figures 3.35a, 3.36a and 3.37a, the AOD values are higher for the case where desert dust is considered, than the respective values found in the dust free case, as it would be expected, since the desert dust aerosols contribute to the aerosol optical depth increase. On 27 May (Figure 3.35a), for the dust free atmosphere an averaged maximum AOD value of 3.8×10^{-3} is found whereas, in a dusty atmosphere, an averaged maximum AOD value of 0.09 is establish.

When desert dust are not present in the atmosphere, on 28 May (Figure 3.36a), an averaged maximum AOD value of 3.6×10^{-3} is found while the corresponding AOD value in a dusty atmosphere is 0.08. According to Figure 3.37a, for 29 May, in the absence of DD aerosols the averaged maximum AOD value is 3.7×10^{-3} and, the presence of DD aerosols in the atmosphere shows an averaged maximum AOD value of 0.05.

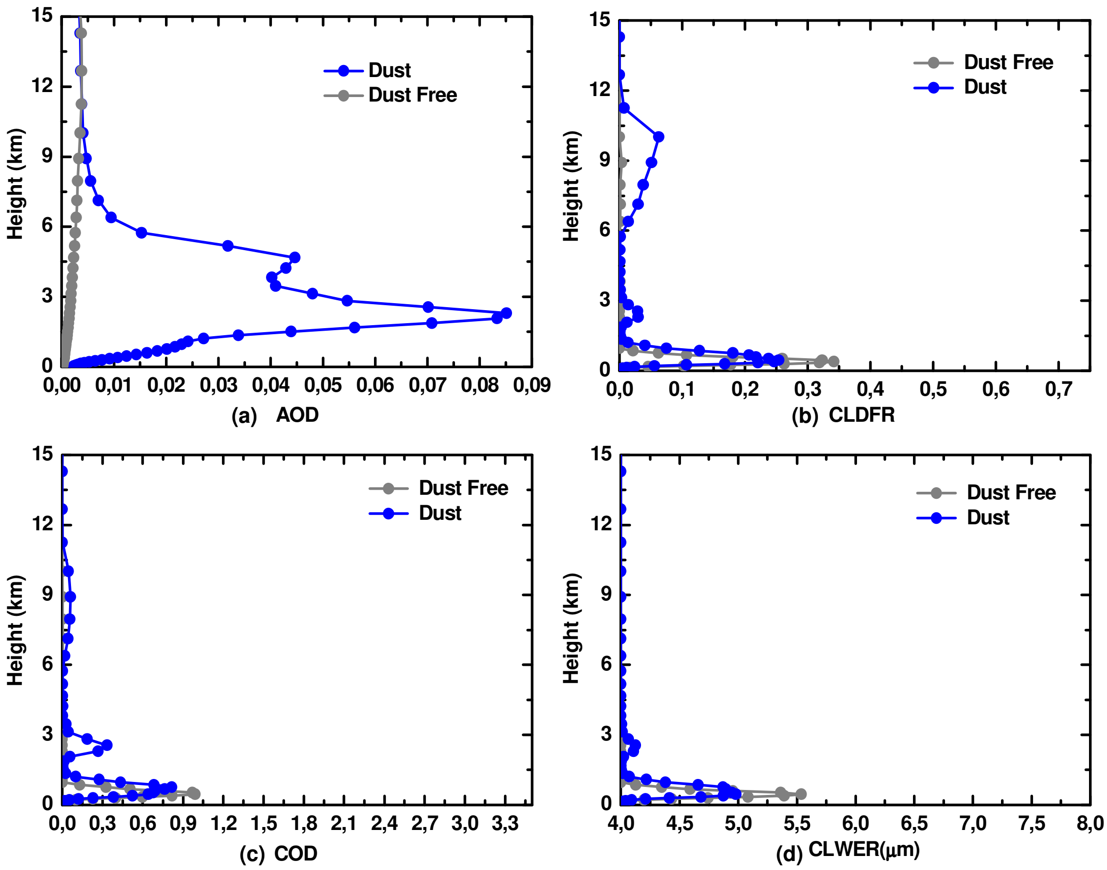

Figure 3.35 Vertical profiles of the aerosol optical depth, at 0.55μm, (a), the cloud fraction (b), the cloud optical depth (c) and cloud liquid water effective radius (d), for clouds in a dust free atmosphere and for clouds in an atmosphere with mineral dust, on 27May 2006.

Looking now at the simulated averaged CLDFR values (Figures 3.35b and 3.36b, respectively, on the 27 and 28 May) it can be seen that the presence of DD aerosols provokes a decrease in the CLDFR values. According to Figure 3.35b, on 27 May, an CLDFR maximum value of 0.34 is found in the absence of mineral dust whereas, in their presence the CLDFR maximum value is only 0.25. On the 28 May (Figure 3.36b), the CLDFR maximum value is 0.72, when DD aren't present in the atmosphere, and the corresponding value considering the presence of mineral dust is only 0.42.

This situation is not so evident on the 29 May (Figure 3.37b): in a dust free atmosphere, the CLDFR maximum value found is 0.61 while, in a dusty atmosphere, an CLDFR maximum value of 0.53 is found. However, considering that, for this day, the MesoNH model overestimates the CLDFR quantities (Figures 3.9e and 3.9f), particularly when desert dust aerosols are considered in the simulations, these difference in the CLDFR values are not so confident.

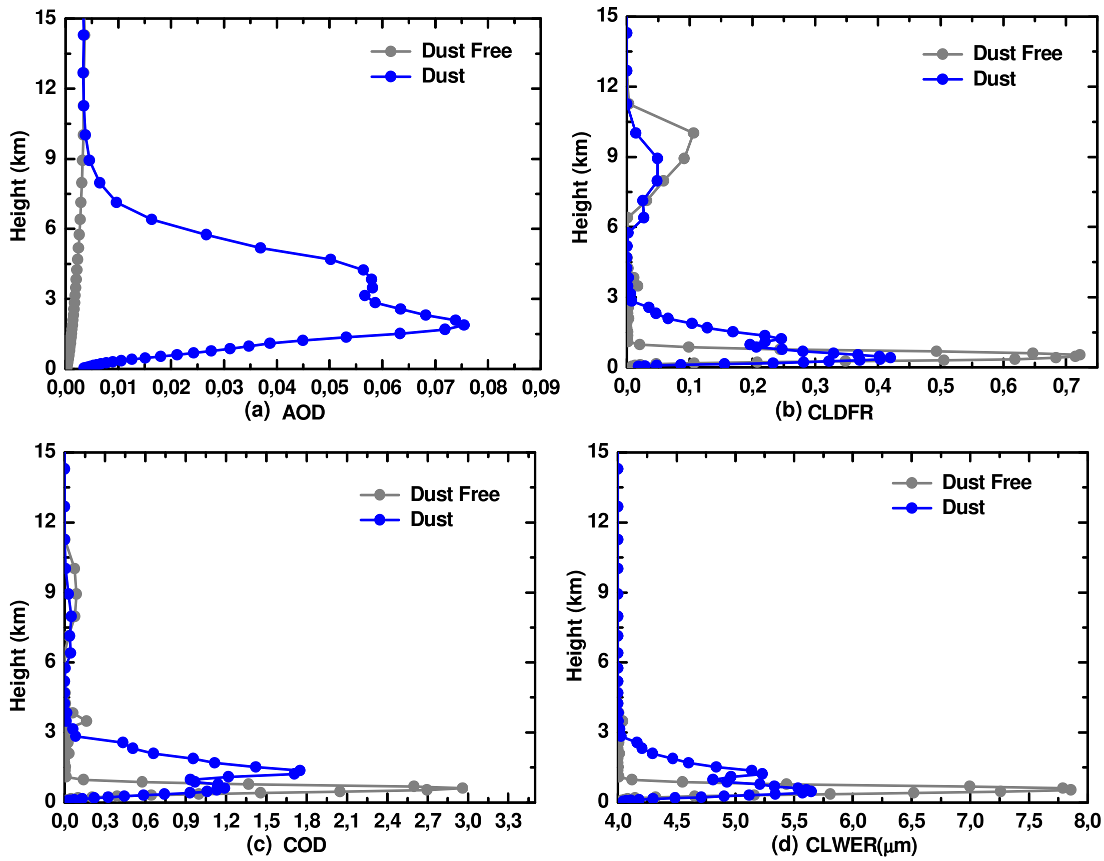

Figure 3.36 Same as Figure 3.35 for 28 May.

This decrease in the cloud fraction, due to the presence of DD aerosols when the clouds are forming, is in agreement with Huang et al. (2006b) and Perlwitz and Miller (2010) who state that, due to the absorption of solar radiation, by DD aerosols, the evaporation of cloud droplets within the clouds is increased, which may lead to a decrease in cloud cover. Ackerman et al. (2000) also found that absorbing aerosols reduced the relative humidity in the boundary layer and caused a 5 - 10 % reduction in cloud fraction.

On the 27 May, for the dust free atmosphere an averaged maximum COD value of 1.0 is found whereas, in an dusty atmosphere, the corresponding COD value is 0.82, as can be shown in Figure 3.35c. On the 28th May, when desert dust aerosols aren't present in the atmosphere, an averaged maximum COD value of 2.96 is found, while the corresponding COD value in a dusty atmosphere is 1.75 (Figure 3.36c). For the 29 May, and according to Figure 3.37c the averaged maximum COD value is 3.40, in the absence of DD aerosols and an averaged maximum COD value of 2.53 is found in the presence of DD aerosols in the atmosphere. This decrease in COD values may be related to the semi-direct effect of aerosols or cloud evaporation. As dust aerosols cool the Earth's surface and heat the aerosol layer, the atmospheric stability within and above the boundary layer is reduced, resulting in enhanced vertical motion and increased airborne dust. Additionally, dust aerosols can cause evaporation of cloud droplets (semi-direct effect). This leads to reduced COD values.

This decrease in COD is in agreement with Huang et al. (2006a) and Wang et al. (2010), who found that desert dust aerosols change the microphysical characteristics of clouds, reducing the cloud optical depth, and effective droplet size.

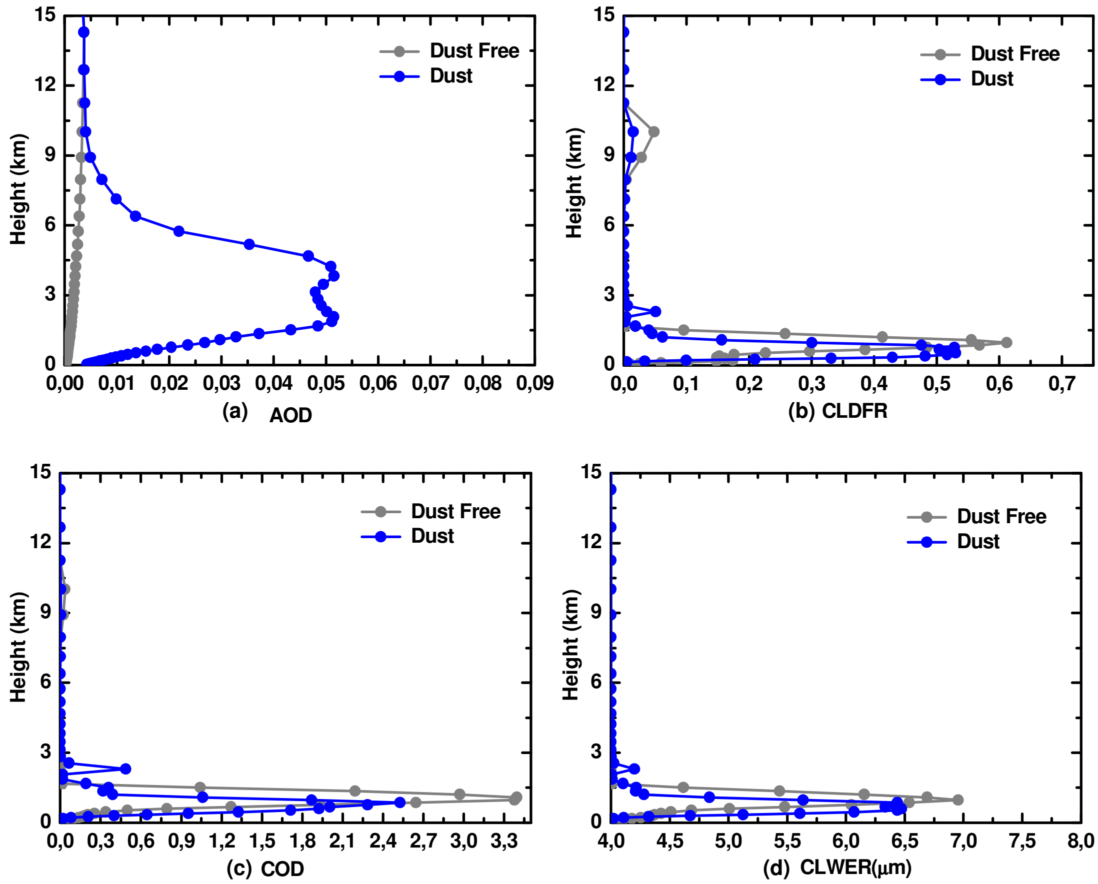

Figure 3.37 Same as Figure 3.35 for 29 May.

Although the presence of desert dust seems to reduce the values of the COD, it is interesting to note that the when dust is considered, during the formation of clouds, the lower level clouds systematically present a higher vertical development. It can be observed that in all days the COD values for the dusty atmosphere present a higher extension in altitude than the COD values for the dust free atmosphere. These results are consistent with Solomos et al. (2011) who estimate that, an increase of 15% in the concentration dust particles, produce clouds that extended about three kilometers higher and the initiation of precipitation was delayed by almost one hour.

Considering now the cloud mean liquid effective radius values (CLWER), for all the days of May under study (Figures 3.35d, 3.36d and 3.37d), it can be observed that when desert dust starts to interact with the cloud layer (altitude bellow 3km), the

CLWER values are, for the dusty atmosphere case, lower than the correspondent CLWER values where no dust is considered.

For the 27 May and according to Figure 3.35d, an CLWER maximum value of 5.5 is found in the absence of mineral dust whereas, in its presence, the CLWER maximum value is 4.9. On the 28 May (Figure 3.36d), the CLWER maximum value is 7.9, when DD aren't present in the atmosphere, and the corresponding value, considering the presence of mineral dust, is 5.7. For the 29 May (Figure 3.37d), in a dust free atmosphere, the CLWER maximum value found is 7.0 while, in a dusty atmosphere, a CLWER maximum value of 6.5 is found. This decrease in CLWER values is in agreement with several authors (e. g. Twomey, 1974; Haywood and Boucher, 2000; Rosenfeld et al, 2001; Ramanathan et al, 2001; Hui et al, 2008; Stevens and Feingold, 2009; and Wang et al., 2010). It can be explained due to the fact that Saharan desert particles often act as cloud condensation nuclei (CCN), which means they are nuclei for the condensating water vapour. When a cloud comes into contact with mineral dust, the number of CCN increases, so that the number of cloud droplets also increases. With the same amount of liquid water, the size of each droplet decreases (water is distributed among more CCN).

Considering now the September 2007 DD event and according to Figures 3.38a, 3.39a and 3.40a, once again, and as it would be expected, the AOD values are higher for the case where mineral DD is considered, than the respective values found in the dust free case. On 06 September (Figure 3.38a), for the dust free atmosphere an averaged maximum AOD value of 4.2×10^{-4} is found were, in a dusty atmosphere, an averaged maximum AOD value of 1.8×10^{-2} is establish. On the 07 September (Figure 3.39a), when desert dust are not present in the atmosphere, an averaged maximum AOD value of 4.3×10^{-4} is found while the corresponding AOD value in a dusty atmosphere is 1.7×10^{-2}. On the 08 September (Figure 3.40a) the averaged maximum AOD value is 4.2×10^{-4} in the absence of DD aerosols and an averaged maximum AOD value of 1.0×10^{-2} is found in the presence of DD aerosols in the atmosphere.

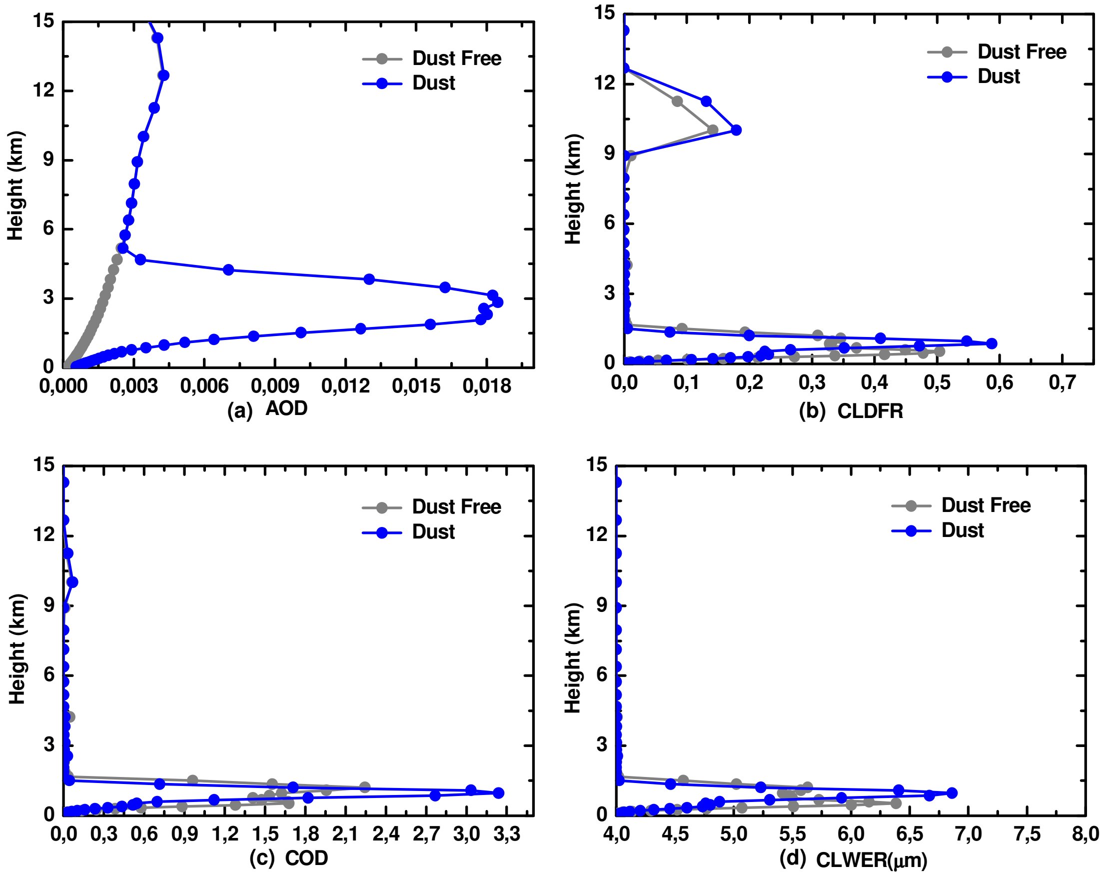

Figure 3.38 Vertical profiles of the aerosol optical depth, at 0.55μm, (a), the cloud fraction (b), the cloud optical depth (c) and cloud liquid water effective radius (d), for clouds in a dust free atmosphere and for clouds in an atmosphere with mineral dust, on 06 September.

Considering the simulated averaged CLDFR values on 06 and 07 September (Figures 3.38b and 3.39b), it can be seen that the presence of DD aerosols increases the CLDFR amount. This situation also occurs on 08 September, but for altitudes above ~1km, where the simulated CLDFR values are lower in the absence of desert dust aerosols. However, for this day, the DD event is not so pronounced as for the other days (AOD values in Figure 3.40a are lower compared with the corresponding ones in Figures 3.38a and 3.39a).

On 06 September, a CLDFR maximum value of 0.59 is found in the absence of mineral dust, as shown in Figure 3.38b, whereas, in their presence an CLDFR maximum value of 0.50 is found. On the 07 September (Figure 3.39b), the CLDFR maximum value is 0.26, when DD aren't present in the atmosphere, and the corresponding value considering the presence of mineral dust is 0.38. This situation doesn't take place on 08 September (Figure 3.40b). In a dust free atmosphere, the CLDFR maximum value found is 0.7 while, in a dusty atmosphere, a CLDFR maximum value of 0.56 is found. This may be related to the fact that, the desert dust event is not so pronounced as for the other days, as already mentioned above, and also due to the fact that the CLDFR values for this day (Figure 3.40b) are higher than the CLDFR values in the other two previous days (Figures 3.38b and 3.39b) leading then to the conclusion that new clouds are reaching the study area and influencing the CLDFR values.

The cloud optical depth (COD) simulated values, for 06, 07 and 08 September, are presented in Figures 3.38c, 3.39c and 3.40c. The presence of desert dust appears to increase the values of the COD, except for 08 September were the dusty clouds present a higher vertical development.

On 06 September (Figure 3.38c), for the dust free atmosphere an averaged maximum COD value of 2.24 is found whereas, in an dusty atmosphere, the corresponding COD value is 3.24. When desert dust aerosols aren't present in the atmosphere (on 08 September, Figure 3.39c), an averaged maximum COD value of 1.42 is found, while the corresponding COD value in a dusty atmosphere is 2.07.

According to Figure 3.40c, for the 08 September the averaged maximum COD value is 1.2, in the absence of DD aerosols and for the presence of DD aerosols in the atmosphere an averaged maximum COD value of 1.8 is found.

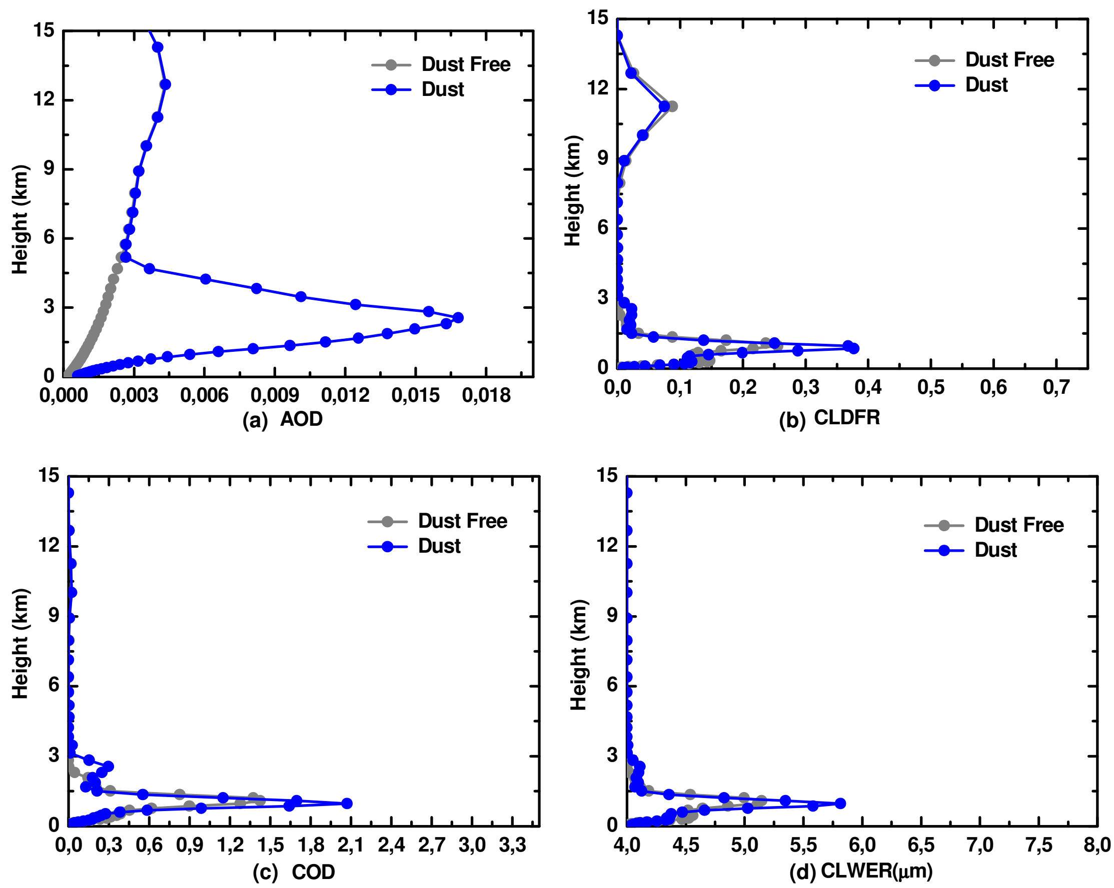

Figure 3.39 Same as Figure 3.36 for 07 September.

Experiment case studies of Erlick et al. (2001) found that absorbing aerosols, particularly supermicron dust and soot aerosols that nucleate small cloud drops can increase cloud optical depth by a factor of 1.5 to 3. This conclusion may support the results of COD found only for the September episode, which is opposite of what was found for the May episode. This means that the DD aerosol optical properties of these two events (May and September) are different being the ones of the May episode less absorbing and more scattering, although with a bigger AOD then the ones from September.

On 06 September (Figure 3.38d), a liquid water effective radius (CLWER) maximum value of 6.4 is found in the absence of mineral dust whereas, in their presence, the CLWER maximum value is 6.9 . On 07 September (Figure 3.39d), the CLWER maximum value is 5.1 when DD aren't present in the atmosphere and the corresponding value, considering the presence of mineral dust, is 5.8 .

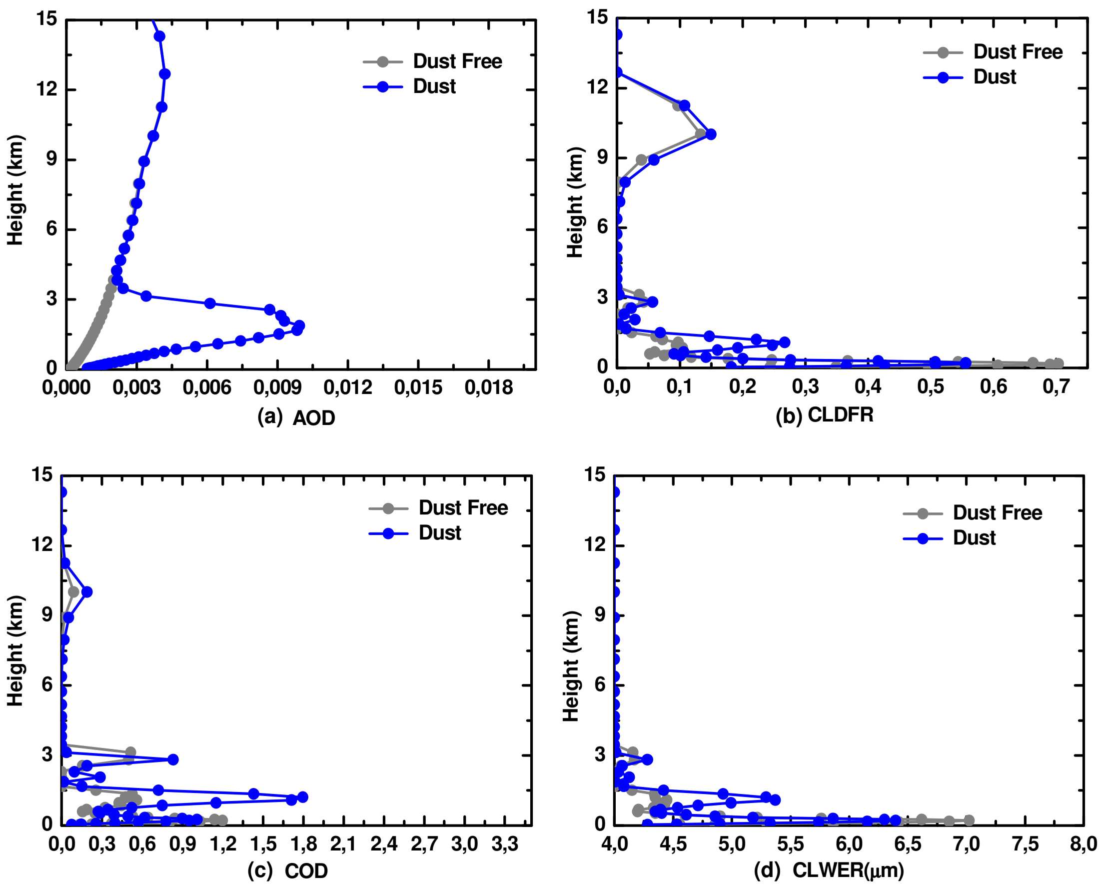

Figure 3.40 Same as Figure 3.36 for 08 September.

For 08 September (Figure 3.40d), in a dust free atmosphere, the CLWER maximum value found is 7.0 while, in a dusty atmosphere, a CLWER maximum value of 6.4 is found. These results show that, except for the 08 September (Figure 3.40d), the desert dust interaction with the cloud layer, provokes an increase in the averaged CLWER values.

It was expected that DD aerosols, when interacting with the cloud layer, produce small droplets, thus changing the cloud properties and extending their lifetime as the water may remain longer within the cloud, as it was mentioned before. In contrast to this "normal" behaviour in the case of generally low droplet sizes in the cloud field, the entrainment of giant condensation nuclei such as (aged) mineral dust particles also has been observed to be able to shift the cloud droplet size spectrum towards larger droplets (Feingold et al., 1999). The increase of effective radii might be the result of the combination of smaller effective radii in clouds and the large dust particle acting as giant CCN directly initiating the formation of large cloud droplets, an effect already described by Feingold et al. (1999) from case study results. This mechanism remains somewhat speculative although the effective radius increase is evident from the simulated values analysis. It would be very useful to have in situ observations to confirm this kind of occurrences where there is a clear need of aerosol type discrimination in aerosol-cloud-interaction studies.

An increase of effective radii was also found by Kluser et al. (2010) who considered that, under moderate dust loadings, the cloud effective radii are increased with respect to dustiness; under heavy dust loads, cloud effective radii are reduced again. This finding can be related to the simulated results obtain in this work: on 06 and 07 September, an increase of effective radii is verified (Figures 3.38d and 3.39d) but on 27, 28 and 29 May, a decrease in CLWER values is found (Figures 3.35d and 3.36d), however, for 06 and 07 September the AOD values (Figures 3.38a and 3.39a), are smaller than the correspondent AOD values on the 27, 28 and 29 May (Figures 3.35a and 3.36a).

3.5 Desert Dust Aerosol Indirect Radiative Forcing

In order to study the radiative effects of clouds under the influence of mineral desert dust aerosols, the vertical profiles of the SW, LW and total cloud radiative forcing values (SW and LW), averaged over the area of study (where desert dust is present), during the period equivalent to the end of May 2006, are presented in Figure 3.41.

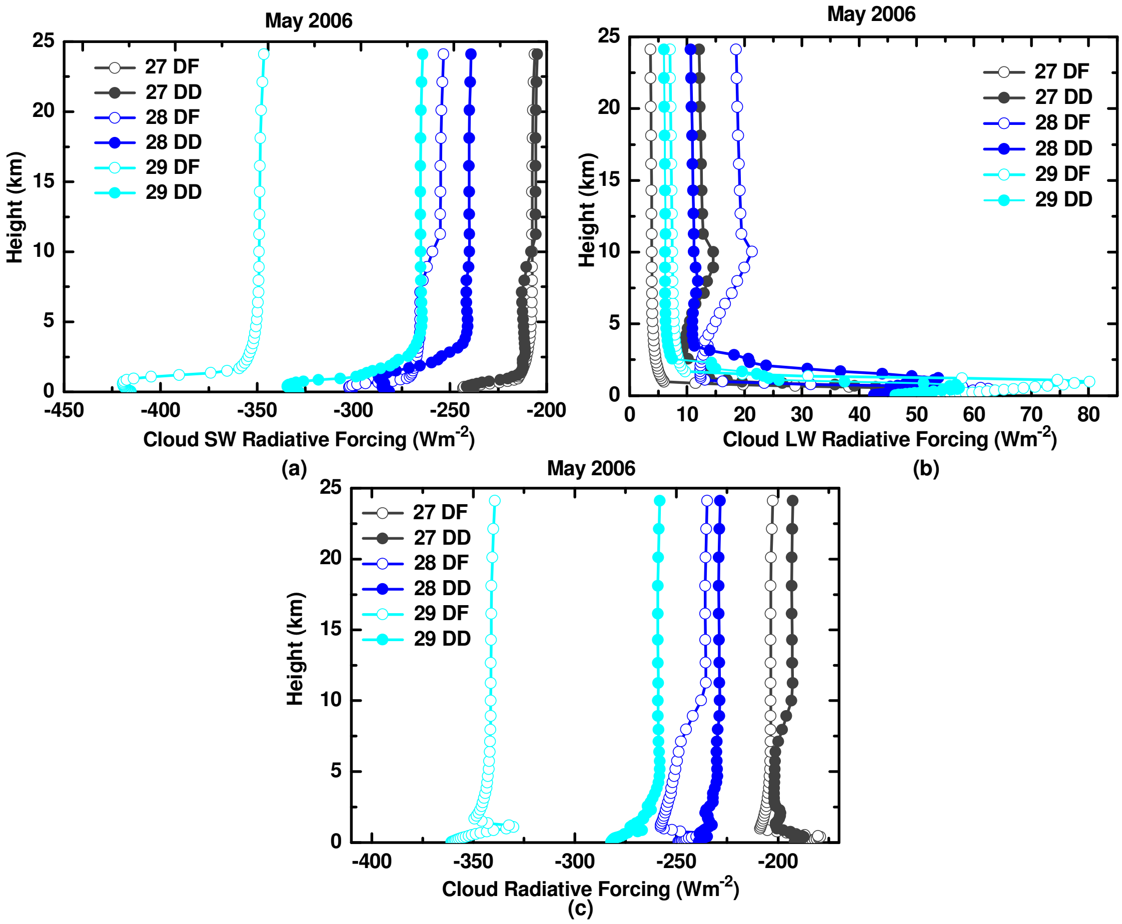

Figure 3.41 Vertical profiles of simulated SW (a), LW (b) and total (c) cloud radiative forcing in the absence (DF) and in the presence (DD) of desert dust aerosols, for 27, 28 and 29 May 2006.

The total Cloud Radiative Forcing (CRF) at the TOA and at the surface levels is calculated according to equation 2.51. When negative values of CRF are found it indicates that clouds cause a cooling effect and when positive values of CRF are found, then it means that a warming effect is present.

Figure 3.41a show the vertical profiles of Cloud SW Radiative Forcing (SWCRF) for the May 2006 desert dust episode. For all the days, a cooling effect is always found, both at surface and TOA levels, but this effect is emphasized as the days pass by. Also, from the analysis of the plots of Figure 3.41, it is feasible to conclude that, for all the studied May days, the cloud cooling effect is more pronounced at the surface level than at the TOA level, since CRF values are more negative at the surface than at the TOA level.

On the 27th May, at TOA level, comparing the cases where the aerosols are present (DD) with the ones where they are absent (DF) in the atmosphere, there is practically no difference in the SWCRF value as in the other days considered in May (Figure 3.41a). In the presence of DD aerosols, a TOA SWCRF value of -205 Wm^{-2} is found and in their absence a TOA SWCRF value of -206 Wm^{-2} is found, meaning, for this specific day, the clouds in the dusty and in the dust free regions reflect roughly the same amount of SW radiation.

For the 28 and 29 May the presence of DD aerosols are responsible for enhancing the TOA SWCRF values since they become more negative. On the 28 May a TOA SWCRF value of -239 Wm^{-2} is obtained for a dusty atmosphere and a TOA SWCRF value of -253 Wm^{-2} for a dust free situation is encountered. For the 29 May a TOA SWCRF value of -264 Wm^{-2} is found for clouds developing in a dusty atmosphere whereas, for dust free clouds, a TOA SWCRF value of -346 Wm^{-2} is found. The weaker TOA SWCRF values in dusty cloud regions may indicate some radiation absorption by the dust aerosol since cloud particle sizes in dusty cloud regions are generally smaller than those in dust free regions.

As already mentioned before, the simulated SWCRF values, at the surface level, confirm that, the presence of DD aerosols increases the cooling effect at the surface, due to clouds, compared to what happen at the TOA level.

Let's analyze what happen at the surface for the situation on clouds developing in the presence of DD and in their absence. On 27 May a surface SWCRF value of -238 Wm^{-2} is found in the presence of DD aerosols, while, in their absence, a surface SWCRF value of -242 Wm^{-2} is found. On the 28 May a surface SWCRF value of -281 Wm^{-2} is encountered for a dusty atmosphere and, for a dust free situation, a surface SWCRF value of -301 Wm^{-2} is obtained. On the 29 May, for clouds developing in a dusty atmosphere, a surface SWCRF value of -328 Wm^{-2} is found and for clouds developing in a dust free atmosphere a TOA SWCRF value of -415 Wm^{-2} is found.

As for the Cloud LW Radiative Forcing (LWCRF) on 27, 28 and 29 May (Figure 3.41b) a warming effect is always found, since positive LWCRF values are presented both at TOA and surface levels. On the 27 May, at TOA level, the TOA LWCRF is 12 Wm^{-2} in the presence of DD aerosol and, in their absence, is 4 Wm^{-2}. On the 28 May, for clouds contaminated by mineral particles, the TOA LWCRF is 11 Wm^{-2} and for non contaminated clouds the TOA LWCRF is 19 Wm^{-2}. On 29 May, for dusty clouds, the TOA LWCRF is 6 Wm^{-2} whereas for non dust free clouds the TOA LWCRF is 7 Wm^{-2}.

However, it is important to note that the LW radiation (Figure 3.41b) has small impact when compared with the SW radiation (Figure 3.41a), as can be seen by the total CRF values presented in Figure 3.41c.

Knowing that the desert dust aerosol layer is, in this study, always situated above the cloud for all the May days (see Figures 3.35a, 3.36a and 3.37a), considering that these type of particles may absorb and reflect radiation, causing a decrease of the radiation reaching the cloud and, consequently, a diminution of the cloud reflected radiation, this phenomena could explain the less negative TOA CRF values compared with the ones encountered for all clouds developing in a dust free atmosphere (Figure 3.41c).

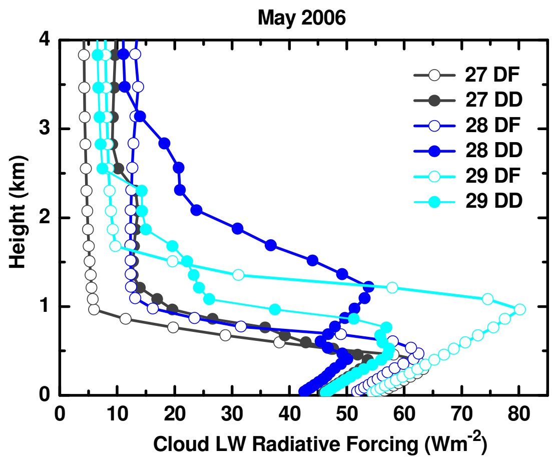

Figure 3.42 Same as Figure 3.39b for the first four kilometers in the atmosphere.

In order to have a better perception of the cloud radiative effects at the surface level, and in the first adjacent atmosphere kilometers, the plots of Figure 3.42 show the vertical profiles of longwave LWCRF for the desert dust episode that occur in the end of May 2006.

As it would be expected, clouds generally reduce the longwave radiation emission from the Earth surface to space resulting in a heating effect (Figure 3.42). Since on 29 May the simulated values for the cloud fraction (Figure 3.9f) present higher values than the respective values obtained for 27 and 28 May, the LWCRF present also higher values (maximum of 57 Wm^{-2} for a dusty atmosphere and 80 Wm^{-2} for a dust free atmosphere) than the LWCRF for 27 and 28 May.

As shown in Figure 3.42, for an atmosphere where clouds and DD aerosols interact, at the surface level, less upwelling LW radiation is emitted compared with the situations where the clouds develop in a dust free atmosphere (DF). On 27 May the mean surface LWCRF value in the presence of DD aerosols is 46 Wm^{-2} and in the absence of DD aerosols is 56 Wm^{-2}. On 28 May the simulated surface LWCRF value is 43 Wm^{-2} for a dusty atmosphere, while, for a dust free atmosphere the corresponding value is 52 Wm^{-2}. Lastly, on 29 May, a value of 46 Wm^{-2} is found for the surface LWCRF in dusty clouds and, for dust free clouds, the surface LWCRF is 55 Wm^{-2}. All these differences in the surface LWCRF values (for the presence and for absence of desert dust aerosols where clouds develop) confirm the importance of the underlying surface contribution to the LW radiation emission to space, whenever the DD aerosol layers are above the clouds.

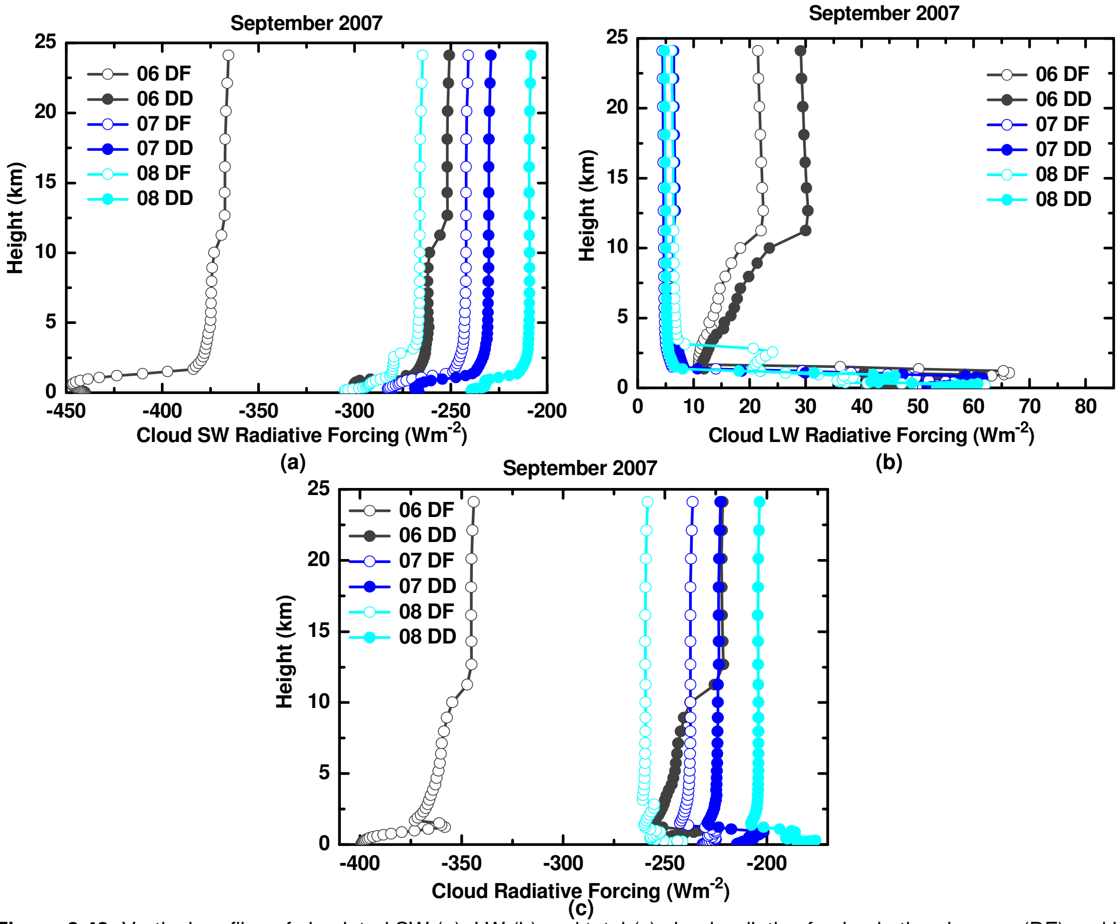

Figure 3.43 Vertical profiles of simulated SW (a), LW (b) and total (c) cloud radiative forcing in the absence (DF) and in the presence (DD) of desert dust aerosols, for 6, 7 and 8 September 2007.

Figure 3.43 present the vertical profiles of the SW, LW and total cloud radiative forcing values, averaged over the area of study (where desert dust are considered), during the period equivalent to 6 - 8 September 2007.

The plots in Figure 3.43c show that, only for 06 September, the cloud cooling effect (black curve with filled circles) is more pronounced at the surface level (≈ - 250 Wm^{-2}) than at the TOA level (≈ - 225 Wm^{-2}), since SWCRF values are more negative at the surface than at the TOA level.

Figure 3.43a show the vertical profiles of Cloud SW Radiative Forcing (SWCRF) for the September 2007 desert dust episode. For all the days, a cooling effect is always found, both at surface and TOA levels (in the presence or absence of DD aerosols).

On the 06 September, at TOA level comparing the cases where the aerosols are present and are absent in the atmosphere, a TOA SWCRF value of -251 Wm^{-2} is found in the presence of DD aerosols and, in their absence, a TOA SWCRF value of -366

Wm^{-2} is found. On the 07 September a TOA SWCRF value of -229 Wm^{-2} is obtained for a dusty atmosphere and, for a dust free situation, a TOA SWCRF value of -241 Wm^{-2} is encountered; on the 08 September a TOA SWCRF value of -265 Wm^{-2} is found, for dust free clouds and a TOA SWCRF value of -208 Wm^{-2} is found for clouds developing in a dusty atmosphere. The TOA SWCRF values encountered for all days suggest that the presence of DD aerosols attenuate the cloud cooling effect. This could be related with the fact that, the presence of DD aerosols increase the AOD, and if the aerosol layer is situated above the cloud, the DD aerosols may absorb and reflect radiation, causing a decrease of the radiation reaching the cloud and, consequently, a diminution of the cloud reflected radiation, explaining the less negative TOASWCRF values compared with the ones encountered for all clouds developing in a dust free atmosphere.

At the surface level, the simulated SWCRF values suggest that, the presence of DD aerosols also attenuate the cooling effect at the surface, due to clouds, but, in all cases (6-8 September) the SWCRF values are always more negative than at the TOA (in the presence or in the absence of DD aerosols). On 06 September, a surface SWCRF value of -296Wm^{-2} is found In the presence of DD aerosols, while, in their absence, a surface SWCRF value of -440 Wm^{-2} is found; on 07 September surface SWCRF value of -266 Wm^{-2} is encountered for an atmosphere contaminated with DD aerosols and a surface SWCRF value of -281 Wm^{-2} is obtained for a dust free atmosphere; on 08 September a surface SWCRF value of -238 Wm^{-2} is found for dust free clouds, whereas a surface SWCRF value of -304 Wm^{-2} is found for clouds developing in a contaminated atmosphere.

As for the Cloud LW Radiative Forcing (LWCRF) a warming effect is always found on 06, 07 and 08 September (Figure 3.43b), since positive LWCRF values are presented both at TOA and surface levels. However at TOA level and on 06 September, the warming effect, due to clouds is more significant than on 07 and 08 September. On 06 September the TOA LWCRF is 29 Wm^{-2} in the presence of DD aerosol and, in their absence, is 22 Wm^{-2}; on 07 September, for clouds contaminated by mineral particles, the TOA LWCRF is 6 Wm^{-2} and for non contaminated clouds is 4 Wm^{-2}; on 08 September, for dusty clouds, the TOA LWCRF is 5Wm^{-2} and, for dust free clouds the TOA LWCRF is 6 Wm^{-2}. Also, for the September case study the LW radiation still have small impact on the total cloud radiative forcing, CRF (Figures 3.43b and 3.43c, respectively) compared with the impact of the SW radiation on the total cloud radiative forcing (Figures 3.43a and 3.43c, respectively), since the pattern of CRF values (Figure

3.43c) for the three days, is very similar to the one obtained for the cloud SWCRF (Figure 3.43a).

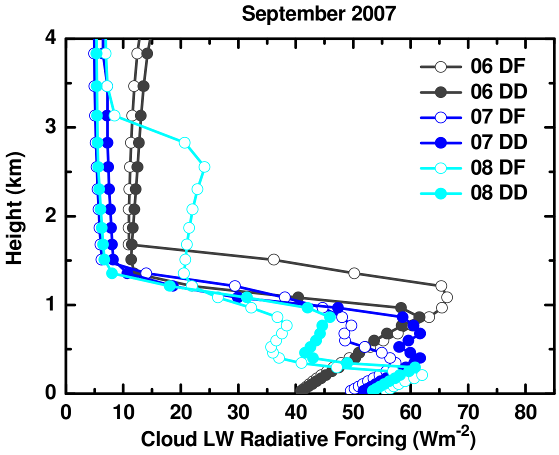

Figure 3.44 Same as Figure 3.41b for the first four kilometers in the atmosphere.

In order to have a better awareness of the LW cloud radiative effects at the surface level, and in the first kilometers of atmosphere, the plots of Figure 3.44 show the vertical profiles of LWCRF for the DD episode that occur in the beginning of September 2007.

As can be seen from the analysis of Figure 3.44, clouds reduce the LW radiation emission to the atmosphere, as expected and already mentioned in page 99, after Figure 3.42. Nevertheless, the surface LWCRF values in the presence of DD aerosols don't differ much from the corresponding values when DD are not present in the atmosphere, as already mentioned in the same page 127. On the 06 September the mean surface LWCRF value has the same value in the presence of DD aerosols as the one encountered in the absence of DD aerosols (41 Wm^{-2}); on the 07 September, for a dusty atmosphere, the simulated surface LWCRF value is 52 Wm^{-2} while, for a dust free atmosphere the corresponding value is 50 Wm^{-2}; finally, on 08 September, a value of 53 Wm^{-2} is found for the surface LWCRF in dusty clouds whereas, for dust free clouds, the surface LWCRF is 56 Wm^{-2}.

Table 3.6 shows the summary of the simulated cloud SWCRF and LWCRF, at the TOA and the surface levels, due to clouds developing in dusty and in dust free conditions, for the all days considered in this work.

In order to compare the simulated cloud forcing results estimated in this work, an effort was made to find similar studies made by other authors. Concerning the cloud radiative forcing at the surface level no findings of results in similar situations could be obtained. However, for the cloud radiative forcing at TOA, under the presence of mineral desert dust several results could be found obtained by several authors (e. g. Huang et al., 2006a; Huang et al., 2006c; Wang et al., 2010). However, these assumptions have to be carefully considered since in the work of Wang et al. (2010) the cloud layer is situated at a higher altitude ($5km$) than the cloud layer found in this work ($\sim 3km$) and in the work of Huang et al., (2006a and 2006c) no information about the cloud height is given, being then not accessible if the cloud type studied by the above mentioned authors can be considered similar to the cloud type (low level clouds) considered in this work.

Forcing (Wm^{-2})	27 May	28 May	29 May	06 Sep	07 Sep	08 Sep
TOASWFndst	-206	-253	-346	-366	-241	-265
TOASWFdst	-205	-239	-264	-251	-229	-208
TOALWFndst	4	19	7	22	4	6
TOALWFdst	12	11	6	29	6	5
SurfSWFndst	-242	-301	-415	-440	-281	-304
SurfSWFdst	-238	-281	-328	-296	-266	-238
SurfLWFndst	56	52	55	41	50	56
SurfLWFdst	46	43	46	41	52	53
TOACRFndst	-203	-235	-339	-344	-236	-259
TOACRFdst	-193	-228	-258	-222	-223	-203
SurfCRFndst	-186	-249	-361	-399	-231	-248
SurfCRFdst	-192	-239	-282	-255	-215	-185

Table 3.6 Simulated SW, LW and total cloud radiative forcing in the absence (ndst) and in the presence (dst) of desert dust aerosols, at TOA and surface (Surf) levels, for 27, 28 and 29 May 2006 and 06, 07 and 08 September 2007.

Over land region, Huang et al. (2006a) analyzed the effects of dust storms on cloud radiative forcing, over Northwestern China from April 2001 to June 2004 using data collected from CERES (Clouds and the Earth's Radiant Energy System) instrument on the Aqua and Terra satellites. Huang et al. (2006a) found, for clouds growing in the presence of dust, an average instantaneous TOASWFdst value of -210 Wm^{-2}, and for the dust free clouds an average instantaneous TOASWFndst value of -280 Wm^{-2} is estimated by this author. These values can be compared respectively with the mean of the simulated TOASWFdst values (- 233 Wm^{-2}) and TOASWFndst values (- 280 Wm^{-2}) obtained in this work for both May and September periods. The differences can be related to the fact that the underlying surface type is not the same (this work estimates the cloud radiative forcing over sea and the described work estimates it over land region).

Huang et al. (2006a) also estimate an TOA LWFndst value of 119 Wm^{-2}, and an TOA LWRFdst of 92 Wm^{-2}, which cannot be comparable with the correspondent results of this work, since lower values are found in the present study (TOA LWFndst mean value of about 10 Wm^{-2} and TOA LWRFdst mean value of about 11.5 Wm^{-2}, for both periods). This fact can be related, one again, with the fact that the underlying surface of Huang et al. (2006a) is land region, which will probably emit more LW radiation than the ocean region considered in this work.

Huang et al. (2006c) estimate the dusty cloud radiative forcing over the middle latitude regions of East Asia, using 2-year (July 2002-June 2004) measured data from the A-Train constellation (information available in http://www.nasa.gov/mission_pages/a-train/). Huang et al. (2006c) found that the instantaneous TOACRFndst is about - 208 Wm^{-2}, which can be comparable although lower with the simulated TOACRFndst values estimated in this work (- 270 Wm^{-2}) and the TOACRFdst is about - 147 Wm^{-2}, which is lower than the TOACRFdst values found in this study (- 221 Wm^{-2}).

Also, Wang et al. (2010) estimate the dusty cloud radiative forcing over the the northwestern Pacific; using measured data from the Pacific Dust Experiment (PACDEX; April 2007 to May 2007) and from the A-Train constellation. Wang et al. (2010) found that the instantaneous TOACRFndst is - 243 Wm^{-2}, which is closer to simulated TOACRFndst values found in this work, and that the instantaneous TOACRFdst is - 208 Wm^{-2}, which can be also comparable with the TOACRFdst values estimated in the current work.

Although the findings of Huang et al. (2006c), and Wang et al. (2010), are different from the ones estimated in the present study, all indicate that the presence of dust aerosols in the atmosphere where clouds develop, significantly reduces the cooling effect of clouds when these develop in a dust free atmosphere.

3.6 Comparison between Model Simulations and Satellite Retrievals

This section presents the comparison between the aerosol optical depth (AOD), at 0.55µm, and the cloud optical depth (COD), simulated with MesoNH model and the same quantities obtained from the MODIS aerosol and cloud products. The current section aims to assess the model ability to simulate the behaviour of desert dust aerosols and clouds in the atmosphere. For this purpose, some statistical indexes are computed; in particular the Equitable Threat Score (ETS) and the Bias Score (BS) (see definition at section 2.4.3).

As for the simulated AOD values, the correspondent ETS and BS results are presented only for the day May 28, 2006 and September 06, 2007, respectively in tables 3.7 and 3.8, as representatives of the other days of their corresponding periods.

The AOD threshold values chosen for 28th of May and shown in table 3.7 are: 0.2, 0.3, 0.4, 0.5, 0.6, 0.7 and 0.8. These values are chosen according to the range of measured values. The largest ETS value found is 0.35 for AOD values greater than the threshold AOD 0.2.The simulated results show that the model represents well the aerosol layer when the AOD values vary between 0.2 and 0.4. For higher AOD values, the ETS values decrease but the number of correct modeled values above the threshold value, N_c becomes smaller as well, and the significance of the result also becomes less reliable.

N = 4098				**28 May 2006**			
AOD Threshold	**>0.2**	**>0.3**	**>0.4**	**>0.5**	**>0.6**	**>0.7**	**>0.8**
ETS	0.35	0.25	0.16	0.10	0.06	0.03	0.01
BS	1.11	1.35	1.92	3.23	5.60	14.8	38.1
N_c	3451	2615	1722	935	482	166	57

Table 3.7 Equitable Threat Score (ETS) and Bias Score (BS) for aerosol optical depth (AOD) on 28 May 2006.

Looking now to the BS values obtained for 28 May it is possible to observe that, for AOD threshold values higher than 0.2, the BS values are slightly above 1 confirming the model tendency to overestimate the areas occupied by aerosols (trough AOD values). For AOD threshold > 0.2, the BS is slightly greater than 1 meaning that the model simulates very well the DD events which results on the occurrence of AOD values between 0.2 and 0.4. On the other hand, the high values of BS for threshold values greater than 0.5 show that the model tends to overestimate the areas where the DD concentrations are very high.

The AOD threshold values chosen for 06 September and shown in table 3.8 are: 0.2, 0.3, 0.4, 0.5, 0.6, 0.7, 0.8, 0.9 and 1.0. The highest ETS value is 0.47, for AOD values above the 0.6 threshold value, which can be considered a good result, since the ETS value is about 0.50, meaning that the MesoNH model reproduces very well the AOD values, especially between 0.5 and 0.8. The lowest ETS value found is 0.01 but the corresponding N_c value is very small, compared to the total number of pairs of modeled and observed values N , and the significance of the result also becomes less reliable.

N = 4819				**06 September 2007**					
AOD Threshold	**>0.2**	**>0.3**	**>0.4**	**>0.5**	**>0.6**	**>0.7**	**>0.8**	**>0.9**	**>1.0**
ETS	0.23	0.23	0.29	0.42	0.47	0.43	0.36	0.16	0.01
BS	0.49	0.49	0.55	0.71	0.83	0.84	0.71	0.35	0.13
N_c	1347	866	557	408	321	244	180	62	5

Table 3.8 Equitable Threat Score (ETS) and Bias Score (BS) for aerosol optical depth (AOD) on 06 September 2007.

Looking now to the BS values on Table 3.8 for AOD threshold values higher than 0.2, the bias score value BS is below one, indicating that, the model has a tendency to underestimate the AOD values. The reproduction of desert dust AOD is considered good for AOD threshold values higher than 0.5, 0.6, 0.7 and 0.8, since the BS values approach the value 1.

As for the simulated COD values, the correspondent ETS results are presented only for the day May 27, 2006 and September 08, 2007, respectively in tables 3.9 and 3.10, as representatives of the other days of their corresponding periods.

N=2533				**27 May 2006**					
COD Threshold	**>5.0**	**>6.0**	**>7.0**	**>8.0**	**>9.0**	**>10.0**	**>15.0**	**>20.0**	**>30.0**
ETS	0.30	0.19	0.18	0.17	0.16	0.14	0.11	0.01	0.05
BS	1.13	1.24	1.39	1.54	1.73	1.86	2.57	2.12	4
N_c	1421	1263	1111	955	817	706	260	27	2

Table 3.9 Equitable Threat Score (ETS) and Bias Score (BS) for cloud optical depth (COD) on 27 May 2006.

The COD threshold values chosen for 27 May and shown in table 3.9 are: 5.0, 6.0, 7.0, 8.0, 9.0, 10.0, 15.0, 20.0 and 30.0. These values are chosen according to the values (measured and simulated). The largest ETS value found is 0.30 for COD values greater than threshold COD 5.0. The simulated results show that the model represents well the appearance of clouds with cloud optical depth values between 5.0 and 6.0. For COD threshold values higher than 20.0 a very low ETS value (0.01) is found, nevertheless, once again the corresponding N_c value is very small, compared to N , and the significance of this result also becomes less consistent.

Looking now to the BS values obtained for 27 May it is possible to observe that the MesoNH model overestimates the areas where COD values for COD threshold values higher than 5.0 (BS values >1) but the COD simulations, higher than 5.0 and 6.0, are relatively trustfully since the BS values approach 1.

The COD threshold values chosen for 08 September and shown in table 3.10 are: 10.0, 11.0, 12.0, 13.0, 14.0 and 15.0.The highest ETS value found is 0.26, for COD threshold values higher than 11.0, meaning that, for these threshold values, the model represents well the cloud optical depth values. As the COD threshold values increase, the ETS values decrease reaching a value of 0.06 for COD values higher than 14.0, showing that the model does not accurately capture the coverage of clouds with high optical depths.

N=1396	**08 September 2007**					
COD Threshold	**>10.0**	**>11.0**	**>12.0**	**>13.0**	**>14.0**	**>15.0**
ETS	0.15	0.26	0.10	0.09	0.06	0.06
BS	1.52	0.90	0.96	0.97	0.97	1.24
N_c	166	870	970	1019	1060	32

Table 3.10 Equitable Threat Score (ETS) and Bias Score (BS) for cloud optical depth (COD) on 08 September 2007.

According to table 3.10, the BS value for COD higher than 11.0 is very close to 1, meaning that the model simulates very well the areas covered by clouds with COD values above 11.0.

The ETS and BS values found in this work are comparable with the corresponding values obtained by other authors (e.g. Gallus and Segal, 2001; Chien et al., 2002) in the work of validation of models particularly for precipitation forecasts. This is an indicator that the MesoNH model is able to represents relatively well the AOD and COD values for DD episodes.

4. Conclusions and final remarks

4.1 Conclusions

The general aim of this thesis was to investigate the relationship between mineral desert dust aerosols and cloud properties over Iberian Peninsula and the Atlantic Ocean surrounding area. This interaction was studied by combining regional atmospheric modelling and remote sensing data, provided by satellite and in situ measurements.

With this study a contribution was made in order to better understand the interaction of clouds/aerosols as well as their interaction with solar or IR radiation. With this research, a contribution was also made in the quantification of cloud/aerosol radiative effects.

Following the main goals of this study presented in section 1.2, the following conclusions can be presented.

- Concerning the assessement of the MesoNH performance to simulate the DD aerosol and cloud behaviour in the atmosphere the main conlusions are:

According to the simulated aerosol optical depth (AOD) results it is possible to conclude that the MesoNH model simulates very well the DD aerosols plume since the AOD pattern results were in a good agreement with the actual situation represented by MODIS instrument.

From the comparison between the cloud base height values obtained from the VAISALA ceilometer measurements and the corresponding similated ones obtained with the MesoNH model, over Évora, it was shown that, although the simulated results of the cloud locations are slightly spatially dislocated from the observation site, the simulated values of the base height of convective clouds agree fairly well with the ones obtained from measurements.

As for the simulated total cloud fraction (CLDFR), suplied by MesoNH calculations for the days considered in the study, 27 to 29 May 2006 and 06 to 07 September 2007, the CLDFR was, in general less, when desert dust scheme is not taken into account, than the CLDFR in the presence of desert dust aerosols. However, when compared with the actual CLDFR retrieved from MODIS, the simulated results seem to overestimate the CLDFR quantities, particularly when DD aerosols are considered in the simulations.

In order to evaluate the model capacity to simulate the behaviour of desert dust aerosols and clouds in the atmosphere the Equitable Threat Score (ETS) index and the

Bias Score (BS) were calculated for Saharan desert dust (DD) aerosol optical depth (AOD) and cloud optical depth (COD). The computed scores revealed the MesoNH skill to simulate both the AOD and the COD with a performance comparable to other models and reported in literature (e. g. Gallus and Segal, 2001; Chien et al., 2002).

- Concerning the estimation of the radiative forcing due to mineral desert dust aerosols and the effect of different surfaces on these estimations, the main results were achieved:

In order to investigate the effect of Saharan desert dust storms, an assessment of the desert dust aerosol direct radiative forcing was made at TOA and surface levels over the land (Iberian Peninsula) and over the ocean (Atlantic Ocean). It was possible to observe that the presence of DD aerosols in the atmosphere provokes, in the majority of the cases, a SW cooling effect both at the top at the atmosphere (TOA) and at the surface (Surf) levels and over the two different surfaces (land/ocean), because negative values of TOA shortwave forcing (SWF) and SurfSWF are found. Nevertheless, it was observed that this cooling effect is always more pronounced at the surface (e.g. -116 Wm^{-2}, for 27 May 2006, over the ocean) level than at the TOA level (e.g. -23 Wm^{-2}, for 27 May 2006, over the ocean), since SWF values are more negative at the surface than at the TOA. The TOA SWF values simulated in this study seem to be in agreement with Chen et al. (2009) (- 21 W/m^{-2}), over ocean region, and the simulated SurfSWF values found in this study are comparable with the ones found by Ge at al. (2010) (- 107 W/m^{-2}), over land region.

As for the longwave forcing (LWF) at the TOA (TOALWF) and at the surface (SurfLWF), it was noted that, for all the days under study, the differences were not so prominent as for the case of SW radiation forcing. The TOALWF and SurfLWF simulated values were very close to each other, for the majority of the regions.

For the 27 May 2006, over sea region, the average SWF simulated values found at the surface, were more negative than the corresponding values found over the land region. This may be related to the fact that, the averaged AOD values over ocean are slightly higher than the corresponding values found over land. However, for the 28 May, the SWF values over the sea region, at the surface, were less negative than the corresponding values found over the land region. As for the TOA SWF values, presented before, for both days and both regions (over the ocean and land), it is possible to observe that, the underlying surface does not appear to have a great impact on the estimation of the TOA SWF.

On the 06September, the SWF values found at the surface, and over land region, are more negative than the corresponding values found over the sea region. The same situation happens for the correspondent SWF values, for all days and both regions.

For all the days considered in this study, the effect of the underlying surface doesn't seem, apparently, to interfere in the estimation of LWF, at TOA and surface levels, both over sea as well as over land regions.

- As to the possible modifications that clouds may suffer due to their interactions with desert dust aerosols, the following main results could be obtained:

Mineral dust aerosols appear to change the microphysical characteristics of clouds. With the purpose of investigate these possible modifications, the study of same cloud microphysical properties and aerosol quantities was made for the May 2006 and for the September 2007 DD aerosol episodes. The cloud properties simulated for the two desert dust events were: the mean liquid water effective radius (CLWER) and the mean cloud optical depth (COD), over a selected region where clouds and aerosols are present in the atmosphere, simultaneously; the mean total cloud fraction (CLDFR) and the mean aerosol optical depth (AOD).

Considering the May 2006 DD episode, it was shown that the presence of DD aerosols provokes a decrease in the CLDFR values (e. g. 0.72 to 0.42 for 28 May). The decrease in CLDFR is in agreement with several authors, namely Ackerman et al. (2000), Huang et al. (2006b) and Perlwitz and Miller (2010). Although the presence of DD seems to reduce the values of the COD (e. g. 1.0 to 0.82 for 27 May), in agreement with Huang et al. (2006a) and Wang et al. (2010), the lower clouds systematically present a higher vertical development. In all May days it was possible to observe, that the COD values for the dusty atmosphere present a higher extension in altitude than the COD values for the dust free atmosphere, which was also found by Solomos et al., 2011. As for the CLWER values and for the May period under study, a reduction of CLWER is verified when DD aerosols start to interact with the cloud layer (e. g. 7.9 to 5.7 for 28 May), similar to what was also found by several authors (Twomey, 1974; Haywood and Boucher, 2000; Rosenfeld et al., 2001; Ramanathan et al., 2001; Hui et al., 2008; Stevens and Feingold, 2009; and Wang et al., 2010).This reduction is consistent with the decreasing on cloud droplet size, since the DD particles often act as cloud condensation nuclei (CCN), which means they are nuclei for the condensating water vapour. Therefore, when a warm water cloud comes into contact with mineral dust, the number of CCN increases, so that the number of cloud droplets also increases and assuming the amount of liquid water within the cloud is constant, the size of each droplet decreases (water is distributed among more CCN).

However for the September 2007 DD event, the presence of DD seems to increase the CLDFR values (e. g. 0.5 to 0.59 for 06 September) as well as the cloud optical depth (e. g. COD= 1.42 on the 6th September to 2.07 for 07 September). This increase in COD was also found by Erlick et al. (2001). The same situation happens for the CLWER simulated values (e. g. 6.4 to 7.0 for 07 September). These results were also found, under moderate dust loadings (which can be considered the September 2007 DD event) by Kluser et al. (2010).

- Concerning the estimation of the indirect radiative forcing due to the contamination of clouds by mineral desert dust aerosols, the main results can be summarized as follows:

With the aim of study the radiative effects of clouds under the influence of mineral desert dust aerosols, the vertical profiles of the SW, LW and total cloud radiative forcing values, averaged over the area of study (where DD are present), during the periods mentioned before were calculated.

For all the days considered in this study, May 2006 and September 2007 DD episodes, the cloud SW radiative forcing (SWCRF) values found showed that a cooling effect is always found and that effect was more pronounced at the surface level than at the TOA level (mean SurfSWCRF value of -275 Wm^{-2} and mean TOASWCRF value of -233 Wm^{-2}). The results obtained are comparable with the ones found by Huang et al. (2006a) and Wang et al. (2010). At the surface level, the simulated SWCRF values supported that, the presence of DD aerosols decreases the cooling effect at the surface, due to clouds.

Though, for the Cloud LW Radiative Forcing (LWCRF) in all studied days, a warming effect was always found. The cloud LW radiative forcing (LWCRF) values found that the warming effect was more pronounced at the surface level than at the TOA level (mean SurfLWCRF value of 47 Wm^{-2} and mean TOASWCRF value of 12 Wm^{-2}). However, it is important to note that the LW radiation has small impact when compared with the SW radiation.

Considering now the results obtained for total cloud radiative forcing in the presence of desert dust aerosols and in their absence, it was possible to observe, that the presence of DD interacting with clouds significantly reduced the cooling effect of clouds (compared with the situation of absence of dust), for all the days considered in this study, both at the TOA and at the surface levels. At the TOA level, and in the presence of DD aerosols, a mean TOACRFdst of -221 Wm^{-2} was found whereas in the absence of DD a mean TOACRFndst of -269 Wm^{-2} was estimated. At the surface level, and in the presence of DD, a mean SurfCRFdst of -228 Wm^{-2} was found while in the absence of DD a mean SurfCRFndst of -279 Wm^{-2} was assessed.

4.2 Future work

It is planned to proceed with this work and extend the comparisons between modeling and measurements made by other instruments than MODIS. New instruments such as the Infrared Atmospheric Sounder Interferometer (IASI) onboard the MetOp satellite may provide height information about dust aerosol and clouds. Also active RADAR and LIDAR instruments (e.g. CloudSat, Caliop) provide height information of clouds and aerosol. With these new observation methods the question of interaction of aerosol and cloud layers may be addressed deeper in future studies.

It is also planned to extend this work for longer periods, for several aerosol types, other than deser dust aerosols, such as biomass burning, pollution, sea salt and various cloud types, other than the warm low/middle clouds, in order to quantify the uncertainties of this model associated with the different simulations.

Bibliography

A

Ackerman, S. A., K. I. Strabala, W. P. Menzel, R. A. Frey, C. C. Moeller, and L. E. Gumley, 1998: Discriminating clear sky from clouds with MODIS. *J. Geophys. Res.,* 103, 32 139– 32 140.

Ackerman, A.S., O.B. Toon, D.E. Stevens, A.J. Heymsfield, V. Ramanathan, and E.J. Welton, 2000: Reduction of tropical cloudiness by soot. *Science*, 288, 1042-1047, doi:10.1126/science.288.5468.1042.

Albrecht, B., 1989: Aerosols, cloud microphysics, and fractional cloudiness, Science, 245, 1227– 1230, doi:10.1126/science.245.4923.1227.

Alfaro, S., 1997: Simulation expérimentale et modélisation de la production d'aérosol mineral par érosion éolienne, Thèse, Université Paris 12 Val de Marne, Laboratoire Interuniversitaire des Systèmes Atmosphériques, Créteil, France.

Alfaro, S. C., Gaudichet, A., Gomes, L., and Maille, M., 1998: Mineral aerosol production by wind erosion: aerosol particle sixes and binding energies, *Geophys. Res. Lett.*, 25, 991–994.

Alfaro, S. C., and L. Gomes, 2001: Modeling mineral aerosol production by wind erosion : Emission intensities and aerosol distributions in source areas, *J. Geophys. Res.*, 106 (D16),18,075–18,084.

Andreae, M.O., Jones, C.D., Cox, P.M., 2005. Strong present-day aerosol cooling implies a hot future. *Nature* 435 (3671), 1187–1190.

Andreae, M.O., Rosenfeld, D., 2008: Aerosol-cloud-precipitation interactions. Part 1.The nature and sources of cloud-active aerosols. *Earth Science Reviews*, Vol. 89, No. 1-2., pp. 13-41.

Anthes, R. A., 1983: A review of regional models of the atmosphere in middle latitudes, *Mon. Weather. Rev.*, 111(6), 1306–1335.

Asselin R. 1972. Frequency filter for time integrations. *Mon. Weather Rev.* 100: 487–490.

B

Bagnold, R. A.,1941: The physics of blown sand and desert dunes, Methuen, London, 265 pp.

Baker, M. B., Peter, T., 2008: Small-scale cloud processes and climate, *Nature*, v. 451, p. 299-300.

Bechtold, P., E. Bazile, F. Guichard, P. Mascart and E. Richard, 2001: A mass-flux convection scheme for regional and global models. Quarterly Journal of the Royal Meteorological Society, Volume 127, Issue 573, April 2001 Part A, Pages: 869–886. DOI: 10.1002/qj.49712757309.

Berthet, S., 2010: Développement d'un nouveau schéma de physique des nuages dans le modèle de méso-échelle MésoNH pour l'étude des interactions aérosol-nuage, PhD Dissertation, Ecole doctorale Sciences de l'Univers, de l'Environnement et de l'Espace (SDU2E), Toulouse University.

Best, M. J., A. Beljaars, J. Polcher, P. Viterbo, 2004: A Proposed Structure for Coupling Tiled Surfaces with the Planetary Boundary Layer. J. Hydrometeor, 5, 1271 – 1278. doi: http://dx.doi.org/10.1175/JHM-382.1.

Binkowski, F. S., and S. J. Roselle, 2003: Models-3 Community Multiscale Air Quality (CMAQ) model aerosol component, 1, Model description, *J. Geophys. Res.*, 108(D6), 4183, doi:10.1029/2001JD001409.

Bou Karam, D., 2008: Mécanismes de soulèvement d'aérosols désertiques en Afrique de l'Ouest, PhD Dissertation, Université Pierre et Marie Curie - Paris VI.

Bougeault, P., and P. Lacarre`re, 1989: Parameterization of orography-induced turbulence in a mesobeta-scale model. Mon. Wea. Rev., 117,1872–1890.

Bouet, C., 2007: Modélisation multi-échelle de la dynamique des panaches d'aérosols naturels en Afrique, PhD Dissertation, Université Blaise Pascal - Clermont-Ferrand II.

Brenguier, J.-L., Burnet, F., and Geoffroy, O., 2011: Cloud optical thickness and liquid water path. Does the k coefficient vary with droplet concentration?, Atmos. Chem. Phys. Discuss., 11, 5173-5215, doi:10.5194/acpd-11-5173-2011.

Bréon, F.-M., F.-M., D. Tanré, and S. Generoso, 2002: Aerosol effect on cloud droplet size monitored from satellite, Science, 295, 834–838.

Brooks, M. E., R. J. Hogan and A. J. Illingworth, 2005: Parameterizing the difference in cloud fraction defined by area and volume as observed with radar and lidar. *J. Atmos. Sci.,*62, 2248-2260.

Browning , K., A., and Robert J. Gurney, 1999: Global Energy and Water Cycles. pp. 304. ISBN 0521560578. Cambridge, UK: Cambridge University Press.

C

Chaboureau, J.-P., P. Tulet, and C. Mari, 2007: Diurnal cycle of dust and cirrus over West Africa as seen from Meteosat Second Generation satellite and a regional forecast model, *Geophys. Res. Lett.*, *34*, L02822, doi:10.1029/2006GL027771.

Chen, L., Shi, G-Y, Zhong, L-Z, and Tan, S-C., 2009: Assessment of Dust Aerosol Optical Depth and Shortwave Radiative. Forcing over the Northwest Pacific Ocean in Spring Based on Satellite Observations, *Atmospheric and Oceanic Science Letters*, Vol. 2, NO. 4, 224–229.

Chin, M., R. Rood, S. J. Lin, J. F. Müller, and A. Thompson, 2000: Atmospheric sulfur cycle simulated in the global model GOCART: Model description and global properties, *J. Geophys. Res.*, 105(D20), 24671-24687.

Chin, M., Kahn, R. A., Remer, L. A., Yu, H., Rind, D., Feingold, G., Quinn, P. K., Schwartz, S. E., Streets, D. G., DeCola, P., Halthore, R., 2009: Atmospheric Aerosol Properties and Climate Impacts, *Report by the U.S. Climate Change Science Program And the Subcommittee on Global Change Research*.

Charlson, R. J., Heintzenberg, J. (Eds.) 1995. Aerosol Forcing of Climate. Wiley, New York, 416p.

Clark, T.L., and R.D. Farley, 1984: Severe Downslope Windstorm Calculations In Two And Three Spatial Dimensions Using Anelastic Interactive Grid Nesting: A Possible Mechanism For Gustiness. *J. Atmos. Sci.*, **41**, 329-350.

Cohard, J. and Pinty, J., 2000a: A comprehensive two-moment warm microphysical bulk scheme. I: Description and tests, *Q. J. R. Meteorology Society*, 126, 1815–1842.

Cohard, J. and Pinty, J., 2000b: A comprehensive two-moment warm microphysical bulk scheme. II: 2D experiments with a non hydrostatic model, *Q. J. R. Meteorology Society*, 126, 1843–1859.

Costa, M. J., Silva, A. M., Levizzani, V., 2004a: Aerosol Characterization and Direct Radiative Forcing Assessment over the Ocean. Part I: Methodology and Sensitivity Analysis. *J. Appl. Meteor.*, 43, 1799–1817. doi: 10.1175/JAM2156.1

Costa, M. J., Silva, A. M., Levizzani, V., 2004b: Aerosol Characterization and Direct Radiative Forcing Assessment over the Ocean. *Part II*: *Application to Test Cases and Validation. J. Appl. Meteor.*, 43, 1818–1833. doi: 10.1175/JAM2156.1.

Costa, M. J., B.-J. Sohn, V. Levizzani, and A. M. Silva, 2006: Radiative forcing of Asian dust determined from the synergized GOME and GMS satellite data - A case study. *J. Meteor. Soc. Japan*, 84, 85-95.

Costa, M. J., D. Bortoli, V. Costa, A. M. Silva, F. Wagner, S. Pereira, J. L. Guerrero-Rascado and L. Alados-Arboledas, 2007: Analysis of the measurements taken by a Ceilometer installed in the south of Portugal. In Remote Sensing of Clouds and the Atmosphere XII, edited by Adolfo Camerón, Klaus Schäfer, James R. Slusser, Richard H. Picard, Also Amodeo, Proceedings of SPIE, (SPIE Bellingham, WA, 2007) Vol. 6745, 674523-1 - 674523-12.

Costa, M. J., R. Salgado, D. Santos, V. Levizzani, D. Bortoli, A. M. Silva, and P. Pinto, 2010: Modelling of orographic precipitation over Iberia: a springtime case study, *Adv. Geosci.*, *25*, 103-110.

Chu, D. A., Y. J. Kaufman, C. Ichoku, L. A. Remer, D. Tanre, and B. N. Holben, 2002: Validation of MODIS aerosol optical depth retrieval over land. *Geophys. Res. Lett.,* 29, 8007, doi:10.1029/ 2001GL013205.

Charlson, R.J., Heintzenberg, J. (Eds.), 1995: Aerosol Forcing of Climate.Wiley, Chichester, New York.416 pp.

Coulson, K. L. , J. V. Dave, and Z. Sekera, 1960: Tables Related to Radiation Emerging from a Planetary Atmosphere with Rayleigh Scattering, U. California Press.

Crumeyrolle S, Gomes L, Tulet P, Matsuki A, Schwarzenboeck A, Crahan K. 2008. Increase of the aerosol hygroscopicity by aqueous mixing in a mesoscale convective system: a case study from the AMMA campaign. *Atmospheric Chemistry and Physics Discussion* **8**: 10057–10103.

Cuxart, J., Bougeault, Ph. and Redelsperger, J.L., 2000: A turbulence scheme allowing for mesoscale and large-eddy simulations. Q. J. R. Meteorol. Soc., 126, 1-30.

D

D'Almeida, G. A., 1986: A model for Saharan dust transport, J. Clim. Appl. Meterol., 25, 903–916.

Denman, K.L., G. Brasseur, A. Chidthaisong, P. Ciais, P.M. Cox, R.E. Dickinson, D. Hauglustaine, C. Heinze, E. Holland, D. Jacob, U. Lohmann, S Ramachandran, P.L. da Silva Dias, S.C. Wofsy and X. Zhang, 2007: Couplings Between Changes in the Climate System and Biogeochemistry. In: Climate Change 2007: The Physical Science Basis. Contribution of Working Group I to the Fourth Assessment Report of the Intergovernmental Panel on Climate Change [Solomon, S., D. Qin, M. Manning, Z. Chen, M. Marquis, K.B. Averyt, M.Tignor and H.L. Miller (eds.)]. Cambridge University Press, Cambridge, United Kingdom and New York, NY, USA.

Delmas, R., G. Mégie, and V. Peuch, 2005: Physique et chimie de l'atmosphère, Echelles, Belin, 639 pp.

DeMott, P. J., Sassen, K., Poellot, M. R., Baumgardner, D., Rogers, D. C., Brooks, S. D., Prenni, A. J., and Kreidenweis, S. M., 2003: African dust aerosols as atmospheric ice nuclei, Geophys. Res. Lett., 30, 1732, doi:10.1029/2003GL017410.

Dong Z.; Wang H.; Liu X.; Li F.; Zhao A., 2002. Velocity profile of a sand cloud blowing over a gravel surface, *Geomorphology*, Volume 45, Number 3, 15 June 2002 , pp. 277-289(13).

Draxler, R. R., and G. D. Hess, 1998: An overview of the Hysplit_4 modelling system for trajectories, *Australian Meteorological Magazine*, **47**, 295-308.

Durran D. R., 1989: Improving the anelastic approximation, J. Atmos. Sci., **46**, 1453-1461.

E

Erlick, C., L. M. Russell, and V. Ramaswamy, 2001: A microphysics-based investigation of the radiative effects of aerosol-cloud interactions for two MAST Experiment case studies, J. Geophys. Res., 106, 1249–1269.

F

Fécan, F., B. Marticorena, and G. Bergametti, 1999: Parameterization of the increase of the aeolian erosion threshold wind friction velocity due to soil moisture for arid and semi-arid areas, *Ann. Geophysicae*, 17, 149–157.

Feingold, G., Cotton, W. R., Kreidenweiss, S. M., and Davies, J. T., 1999: The Impact of Giant Cloud Condensation Nuclei on Drizzle Formation in Stratocumulus: Implications for Cloud Radiative Properties, *J. Atmos. Sci.*, 56, 4100–4117.

Forster, P., V. Ramaswamy, P. Artaxo, T. Berntsen, R. Betts, D.W. Fahey, J. Haywood, J. Lean, D.C. Lowe, G. Myhre, J. Nganga, R. Prinn, G. Raga, M. Schulz and R. Van Dorland, 2007: Changes in Atmospheric Constituents and in Radiative Forcing. *In: Climate Change 2007: The Physical Science Basis. Contribution of Working Group I to the Fourth Assessment Report of the Intergovernmental Panel on Climate Change* [Solomon, S., D. Qin, M. Manning, Z. Chen, M. Marquis, K.B. Averyt, M.Tignor and H.L. Miller (eds.)]. Cambridge University Press, Cambridge, United Kingdom and New York, NY, USA.

Fouquart, Y., and B. Bonnel, 1980: Computations of solar heating of the Earth's atmosphere : A new parameterization, *Beitr. Phys. Atmos.*, 53, 35–62.

G

Gao, B.-C., Y. J. Kaufman, D. Tanré, and R.-R. Li, 2002: Distinguishing tropospheric aerosols from thin cirrus clouds for improved aerosol retrievals using the ratio of 1.38-µm and 1.24-µm channels. *Geophys. Res. Lett.,* **29,** 1890, doi:10.1029/ 2002GL015475.

Gal-Chen, T.and R. Summerville, 1975: On the use of a coordinate transformation for the solution of the Navier–Stokes equations. *J. Comput. Phys.***17** (1975), pp. 209–228.

Ge, J. M., J. Su, T. P. Ackerman, Q. Fu, J. P. Huang, and J. S. Shi, 2010: Dust aerosol optical properties retrieval and radiative forcing over northwestern China during the 2008 China U.S. joint field experiment, *J. Geophys. Res.*, VOL. 115, D00K12, doi:10.1029/2009JD013263

Geoffroy, O., 2007: Modelisation LES des precipitations dans les nuages de couche limite et parametrisation pour les GCM, Ph.D. thesis, Universite Paul Sabatier (Toulouse III).

Gillette, D. A., and P. A. Goodwin, 1974: Microscale transport of sand-sized soil aggregates eroded by wind, *J. Geophys. Res.*, 79 (27), 4080–4084.

Gillette, D. A., and T. R. Walker, 1977: Characteristics of airborne particles produced by wind erosion of sandy soil, high plains of West Texas, *Soil Sci.*, 123, 97–110.

Gillette, D.A., 1978: A wind tunnel simulation of the erosion of soil: Effect of soil texture, sandblasting, windspeed, and soil consolidation on dust production, *Atmos. Environ.*, 12: 1735-1743.

Greeley, R., and J. D. Iversen, 1985: Wind as a geological process, Cambridge University Press, 333 pp.

Grini, A., P. Tulet, and L. Gomes, 2006: Dusty weather forecasts using the MesoNH mesoscale atmospheric model, *J. Geophys. Res.*, *111*, D19205, doi:10.1029/2005JD007007.

Hansen, J., M. Sato, A. Lacis, R. Ruedy, I. Tegen, and E. Matthews, 1998: Climate forcings in the Industrial Era. *Proc. Natl. Acad. Sci.*, 95, 12753-12758.

H

Ham, Seung-Hee, Byung-Ju Sohn, Ping Yang, Bryan A. Baum, 2009: Assessment of the Quality of MODIS Cloud Products from Radiance Simulations, *J. Appl. Meteor. Climatol.*, 48, 1591–1612. doi: 10.1175/2009JAMC2121.1

Hansen, J. E., 1971: Circular polarization of sunlight reflected by clouds, *J. Atmos. Sci.* 28, 1515–1516.

Hansen, J. E. and Travis, L. D., 1974: Light scattering in planetary atmospheres, *Space Sci. Rev.*, 16, 527–610, doi:10.1007/BF00168069.

Haywood, J. M., and V. Ramaswamy, 1998: Global sensitivity studies of the direct radiative forcing due to anthropogenic sulfate and black carbon aerosols, *J. Geophys. Res.*, 103, 6043–6058.

Haywood, J. and Boucher, O., 2000: Estimate of the direct and indirect radiative forcing due to tropospheric aerosols: a review, *Rev. Geophys.*, 38, 513–543.

Heintzenberg, J. and Charlson, R. J., 2009: Clouds in the perturbed climate system – Their relationship to energy balance, atmospheric dynamics, and precipitation, MIT Press, Cambridge, UK, 58–72.

Hogan, R. J., C. Jakob and A. J. Illingworth, 2001: Comparison of ECMWF winter-season cloud fraction with radar derived values, *J. Appl. Meteorol.,*40(3), 513-525.

Hogan, R. J., P. N. Francis, H. Flentje, A. J. Illingworth, M. Quante and J. Pelon, 2003a, Characteristics of mixed-phase clouds - 1. Lidar, radar and aircraft observations from CLARE'98.*Quart. J. Roy. Meteorol. Soc.,*129, 2089-2116.

Hogan, R. J., A. J. Illingworth, E. J. O'Connor and J. P. V. Poiares Baptista, 2003b, Characteristics of mixed-phase clouds - 2. A climatology from ground-based lidar. *Quart. J. Roy. Meteorol. Soc.,*129, 2117-2134.

Hogan, R. J., E. J. O'Connor and A. J. Illingworth, 2009: Verification of cloud-fraction forecasts, *Q. J. R. Meteorol. Soc.,*135, 1494-1511.

Houghton, J.T., et al. (Ed.), 2001. Climate Change, 2001: The Scientific Basis. Contribution of Working Group I to the Third Assessment Report of the Intergovernmental Panel on Climate Change. Cambridge University Press, Cambridge, UK.881 pp.

Hovenier, J. W., van der Mee, C. and Domke, H., 2004: Transfer of Polarized Light in Planetary Atmospheres: Basic Concepts and Practical Methods, Kluwer Academic.

Huang, J., P. Minnis, B. Lin, T. Wang, Y. Yi, Y. Hu, S. Sun-Mack, and K. Ayers, 2006a: Possible influences of Asian dust aerosols on cloud properties and radiative forcing observed from MODIS and CERES, *Geophys. Res. Lett.*, 33, L06824, doi:10.1029/ 2005GL024724.

Huang, J., B. Lin, P. Minnis, T. Wang, X. Wang, Y. Hu, Y. Yi, and J. K. Ayers, 2006b: Satellite-based assessment of possible dust aerosols semidirect effect on cloud water path over east Asia, *Geophys. Res. Lett.*, 33, L19802, doi:10.1029/2006GL026561.

Huang J, Wang Y, Wang Y, Yi Y., 2006c: Dusty cloud radiative forcing derived from satellite data from middle latitude regions of East Asia. *Prog Nat Sci*;16(10):1084–9.

Hui, W. J., Cook, B. I., Ravi, S., Fuentes, J. D., and D'Odorico, P., 2008: Dust-rainfall feedbacks in the West African Sahel, *Water Resources Research*, 44, W05202, doi:10.1029/2008WR006885.

I

IAPSAG, 2007. WMO/IUGG International Aerosol Precipitation Science Assessment Group (IAPSAG) Report: Aerosol Pollution Impact on Precipitation: A Scientific Review, World Meteorological Organization. Geneva.

Illingworth, A. J., R. J. Hogan, E. J. O'Connor, D. Bouniol, M. E. Brooks, J. Delanoe, D. P. Donovan, J. D. Eastment, N. Gaussiat, J. W. F. Goddard, M. Haeffelin, H. Klein Baltink, O. A. Krasnov, J. Pelon, J.-M. Piriou, A. Protat, H. W. J. Russchenberg, A. Seifert, A. M. Tompkins, G.-J.van Zadelhoff, F. Vinit, U. Willen, D. R. Wilson and C. L. Wrench. 2007, Cloudnet - continuous evaluation of cloud profiles in seven operational models using ground-based observations, *Bull. Am. Meteorol. Soc.*,88, 883-898:

IPCC, Climate change 2001: The scientific basis., Contribution of working group I to theThird Assessment Report of the Intergovernmental Panel on Climate Change, Cambridge University Press, Cambridge, United Kingdom and New York, NY, USA, 2001.

IPCC, Climate change 2007: The physical science basis., Contribution of working group I to the Fourth Assessment Report of the Intergovernmental Panel on Climate Change, Cambridge University Press, Cambridge, United Kingdom and New York, NY, USA, 2007.

Isotta, F.A., P. Spichtinger, U. Lohmann, K. von Salzen, 2011: Improvement and Implementation of a Parameterization for Shallow Cumulus in the Global Climate Model ECHAM5-HAM, *J. Atmos. Sci.* ; 68 ; 515-532.

Israelevich, P.L., Levin, Z., Joseph, J.H., Ganor, E., 2002: Desert aerosol transport in the Mediterranean region as inferred from the TOMS aerosol index, *J. Geophys. Res*. 107 (D21), 4572.doi:10.1029/2001JD002011.

Ishizuka, M., M. Mikami, Y. Yamada, F. Zeng, and W. Gao, 2005: An observational study of soil moisture effects on wind erosion at a Gobi site in the Taklimakan desert, *J. Geophys. Res*., 110, D18S03, doi :10.1029/2004JD004709.

Iversen, J. D., and B. R. White, 1982: Saltation threshold on Earth, Mars and Venus, Sedimentology, 29, 111–119.

J

Jacobson, M. Z., 1998: Fundamentals of Atmospheric Modeling, Cambridge University Press, New York, ISBN 0-521-63717-1.

K

Kaufman, Y. J., I. Koren, L. A. Remer, D. Tanré, P. Ginoux, and S. Fan, 2005a: Dust transport and deposition observed from the Terra-Moderate Resolution Imaging Spectroradiometer (MODIS) spacecraft over the Atlantic Ocean, *J. Geophys. Res*., 110, D10S12, doi:10.1029/ 2003JD004436.

Kessler, E., 1969: On the distribution and continuity of water substance in atmospheric circulation, Meteor. Monogr., 32, 84 pp.

Khairoutdinov, M. and Kogan, Y., 2000: A new cloud parameterization in a Large-Eddy Simulation Model of Marine Stratocumulus, *Mon. Weather Rev.*, 128, 229–243.

Kiehl, J., and K. Trenberth, 1997: Earth's annual global mean energy budget. *Bull. Am. Meteorol. Soc.*, **78**, 197–206.

Kim, D.-H., B. J. Sohn, T. Nakajima, and T. Takamura, 2005: Aerosol radiative forcing over east Asia determined from ground-based solar radiation measurements, *J. Geophys. Res.*, 110, D10S22, doi:10.1029/2004JD004678.

King, M. D., Kaufman, Y. J., Menzel, W. P., and Tanre, D., 1992: Remote sensing of cloud, aerosol, and water vapor properties from the Moderate Resolution Imaging Spectrometer (MODIS), *IEEE T. Geosci. Remote*, 30(1), 2–27.

Klüser, L., and Holzer-Popp, T., 2010: Relationships between mineral dust and cloud properties in the West African Sahel, *Atmos. Chem. Phys.*, 10, 6901-6915.

Koehler, K. A., Kreidenweis, S. M., DeMott, P. J., Petters, M. D., Prenni, A. J., and Möhler, O. 2010: Laboratory investigations of the impact of mineral dust aerosol on cold cloud formation, Atmos. Chem. Phys., 10, 11955-11968, doi:10.5194/acp-10-11955.

L

Lafore, J. P., J. Stein, N. Asencio, P. Bougeault, V. Ducrocq, J. Duron, C. Fischer, P. Hereil, P. Mascart, J. P. Pinty, J. L. Redelsperger, E. Richard, and J. Vila-Guerau de Arellano, 1998: The Meso-NH Atmospheric Simulation System. Part I: Adiabatic formulation and control simulations, *Annales Geophysicae*, 16, 90-109.

Laurent, B., 2005: Simulation des émissions d'aérosols désertiques à l'échelle continentale : Analyse climatologique des émissions du nord-est de l'Asie et du nord de l'Afrique, Thèse, Université de Paris 12, Laboratoire Interuniversitaire des Systèmes Atmosphériques, Créteil, France.

Lenoble, J., 1993: Atmospheric Radiative Transfer. A. Deepak Publishing, USA, 532pp.

Levin, Z., and E. Ganor, 1996: The effects of desert particles on cloud and rain formation in the eastern Mediterranean, in The Impact of Desert Dust Across the Mediterranean, edited by S. Guerzoni and R. Chester, pp. 77– 86, Kluwer Acad., Norwell, Mass.

Levin, Z., A. Teller, E. Ganor, B. Graham, M. O. Andreae, W. Maenhaut, A. H. Falkovich and Y. Rudich, 2003: Role of aerosol size and composition in nucleation scavenging within clouds in a shallow cold front, *J. Geophys. Res.*, 108 (D22), 4700, doi:10.1029/2003JD003647.

Liao, H., and Seinfeld, J. H., 1998a: Effects of clouds on direct aerosol radiative forcing of climate, *J. Geophys. Res.*, 103, 3781– 3788.

Liao, H., and Seinfeld, J. H., 1998b: Radiative forcing by mineral dust aerosols: sensitivity to key variables, *J. Geophys. Res*, 103, 31637–31645.

Liepert, B. G., 2002: Observed reductions of surface solar radiation at sites in the United States and worldwide from 1961 to 1990, *Geophys. Res. Lett.*, 29(10), 1421, doi:10.1029/2002GL014910.

Liou, K. N., 1980: An Introduction to Atmospheric Radiation, Academic Press, USA, 392 pp.

Lipps F., and R. S. Hemler, 1982: A scale analysis of deep moist convection and some related numerical calculations, *J. Atmos. Sci.*, **39**, 2192-2210.

Lohmann, U., Feichter, J., 2005: Global indirect aerosol effects: a review. *Atmos. Chem. Phys.* 5, 715–737.

Lohmann, U., 2006: Aerosol Effects on Clouds and Climate, Solar Variability and Planetary *Climates Space Sciences Series of ISSI*, Volume 23, Section II:, 129-137, DOI: 10.1007/978-0-387-48341-2_10.

Lohmann, U., Rotstayn, L., Storelvmo, T., Jones, A., Menon, S., Quaas, J., Ekman, A. M. L., Koch, D., and Ruedy, R., 2010: Total aerosol effect: radiative forcing or radiative flux perturbation?, *Atmos. Chem. Phys.*, 10, 3235–3246, doi:10.5194/acp-10-3235-2010.

Lohmann, U. and C. Hoose, 2009: Sensitivity studies of different aerosol indirect effects in mixed-phase clouds, *Atmos. Chem. Phys.* ; 9 ; 8917-8934.

M

Mahowald, N. M. and Kiehl, L. M., 2003: Mineral aerosol and cloud interactions, *Geophys. Res. Lett.*, 30, 1475, doi:10.1029/2002GL016762.

Marticorena, B., G. Bergametti, B. Aumont, Y. Callot, C. N'Doumé, and M. Legrand, 1997a: Modeling the atmospheric dust cycle : 2-Simulations of Saharan dust sources, J. Geophys. Res., 102 (D4), 4387–4404.

Marticorena, B., G. Bergametti, D. A. Gillette, and J. Belnap, 1997b: Factors controlling threshold friction velocity in semiarid and arid areas of the United States, J. Geophys. Res., 102 (D19), 23,277–23,287.

Marticorena, B., and G. Bergametti, 1995: Modeling the atmospheric dust cycle : 1-Designed of a soil-derived dust emission scheme, J. Geophys. Res., 100 (D8), 16415-16430.

Martins, J. V., D. Tanré, L. A. Remer, Y. J. Kaufman, S. Mattoo, and R. Levy, 2002: MODIS cloud screening for remote sensing of aerosol over oceans using spatial variability. *Geophys. Res. Lett.,* **29,** 8009, doi:10.1029/2001GL013252.

Masson, Valéry, Jean-Louis Champeaux, Fabrice Chauvin, Christelle Meriguet, Roselyne Lacaze, 2003: A Global Database of Land Surface Parameters at 1-km Resolution in Meteorological and Climate Models. J. Climate, 16, 1261 – 1282. doi: http://dx.doi.org/10.1175/1520-0442-16.9.1261.

McKenna-Neumann, C., and W. G. Nickling, 1989: A theoretical and wind tunnel investigation of the effect of capillarity water on the entrainment of sediment by wind, Can. J. Soil Sci., 69, 79–96.

Meloni, D., A. di Sarra, T. Di Iorio, and G. Fiocco, 2005: Influence of the vertical profile of Saharan dust on the visible direct radiative forcing, J. Quant. Spectrosc. Radiat.Transfer, 93, 397– 413.

Messinger F, Arakawa A., 1976: Numerical methods used in atmospheric models. GARP Tech. Rep. 17, WMO/ICSU: Geneva.

Miller, R. and I. Tegen, 1998: Climate response to soil dust aerosols. J. Clim., 11, 3247-3267.

Min, Q.-L., R. Li, B. Lin, E. Joseph, S. Wang, Y. Hu, V. Morris, and F. Chang, 2009: Evidence of mineral dust altering cloud microphysics and precipitation. Atmospheric Chemistry and Physics, 9, 3223–3231.

Mironov, D. V., 2008: Parameterization of lakes in numerical weather prediction. Description of a lake model.*COSMO Technical Report*, No. 11, Deutscher Wetterdienst, Offenbach am Main, Germany, 41 pp.

Morcrette, J.-J., 1989: Description of the radiation scheme in the ECMWF model, Tech. Rep. 165, Res. Dep. of the European Center for Medium range Weather Forecasts, Reading, England.

Myhre, G., A. Grini, J. M. Haywood, F. Stordal, B. Chatenet, D. Tanré, J. K. Sundet, and I. S. A. Isaksen, 2003: Modeling the radiative impact of mineral dust during the Saharan Dust Experiment (SHADE) campaign, J. Geophys. Res., 108(D18), 8579, doi:10.1029/2002JD002566.

Myhre, G., Stordal, F., Johnsrud, M., Kaufman, Y. J., Rosenfeld, D., Storelvmo, T., Kristjansson, J. E., Berntsen, T. K., Myhre, A., and Isaksen, I. S. A., 2007: Aerosol-cloud interaction inferred from MODIS satellite data and global aerosol models, Atmos. Chem. Phys., 7, 3081-3101, doi:10.5194/acp-7-3081-2007.

N

Nakajima, T., and M. Tanaka, 1986: Matrix formulation for the transfer of solar radiation in a plane-parallel scattering atmosphere, J. Quant. Spectrosc. Radiat. Transfer, 35, 13-21.

Nakajima, T., and M. Tanaka, 1988: Algorithms for radiative intensity calculations in moderately thick atmospheres using a truncation approximation, J. Quant. Spectrosc. Radiat.Transfer , 40, 51-69.

O

Oke, T.R., 1987: Boundary Layer Climates. Methuen, London and New York.

P

Perlwitz, J, and Miller, R.L., 2010: Cloud cover increase with increasing aerosol absorptivity: A counterexample to the conventional semidirect aerosol effect; Journal of Geophysical Research 115; 2010

Petitjohn, F. J., P. E. Potter, and R. Siever, 1972: Sand and sandstone, Springer-Verlag, New York, 618 pp.

Pinty, J.-P.and P. Jabouille, 1998: A mixed-phase cloud parameterization for use in a mesoscale non-hydrostatic model: simulations of a squall line and of orographic precipitations. *Proc. AMS conference on cloud physics, 17-21 August 1998, Everett, Wa, USA*, 217–220.

Polcher, J., B. McAvaney P. Viterbo, M.-A. Gaertner, A. Hahmann, J.-F. Mahfouf, J. Noilhan, T. Phillips, A. Pitman, C.A. Schlosser, J.-P. Schulz, B. Timbal, D. Verseghy, Y. Xue, 1998: A proposal for a general interface between land surface schemes and general circulation models. Global Planet. Change, 19, 261–276.

Pöschl, U., 2005: Atmospheric aerosols: composition, transformation, climate and health effects, Angewandte Chemie International Edition, 44, 7520-7540.

Press, W. H., S. A. Teukolsky, W. T. Vetterling, and B. P. Flannery, 1992: Numerical Recipes in FORTRAN: The Art of Scientific Computing. 2nd Ed. Cambridge University Press, 963 pp.

Priestley, C. H. B., 1959: Turbulent Transfer in the Lower Atmosphere.. University of Chicago Press, 130 pp.

Pruppacher, H. R. and J. D. Klett, 1997: Microphysics of Clouds and Precipitation, second edition, Kluwer Academic Publishers, Dordrecht, The Netherlands, 954 pp., ISBN 0-79-234211-1.

Pye, K., 1987: Aeolian dust and dust deposit, Academic Press, San Diego, 334 pp.

R

Ramanathan, V., and M. V. Ramana, 2005: Persistent, Widespread, and strongly absorbing haze over the Himalayan foothills and the Indo- Ganges plains, Pure Appl. Geophys., 162, 1609–1626.

Ramaswamy, V., Boucher, O., Haigh, J., Hauglustaine, D., Haywood, J., Myhre, G., Nakajima, T., Shi, G., Solomon, S. ; Betts, R. E., Charlson, R., Chuang, C. C., Daniel, J. S., Del Genio, A. D., Feichter, J., Fuglestvedt, J., Forster, P. M., Ghan, S. J., Jones, A., Kiehl, J. T., Koch, D., Land, C., Lean, J., Lohmann, U., Minschwaner, K., Penner, J. E., Roberts, D. L., Rodhe, H., Roelofs, G.-J., Rotstayn, L. D., Schneider, T. L., Schumann, U., Schwartz, S. E., Schwartzkopf, M. D., Shine, K. P., Smith, S. J., Stevenson, D. S., Stordal, F., Tegen, I., van Dorland, R., Zhang, Y., Srinivasan, J., Joos, F., 2001: Radiative forcing of climate change. Climate Change 2001: The Scientific Basis, J. T. Houghton et al., Eds., Cambridge University Press, 349–416.

Remer, L. A., D. Tanré, Y. J. Kaufman, C. Ichoku, S. Mattoo, R. Levy, D. A. Chu, B. Holben, O. Dubovik, A. Smirnov, J. V. Martins, R.-R. Li, Z. Ahmad, 2002: Validation of MODIS aerosol retrieval over ocean. *Geophys. Res. Lett.,* **29,** 8008, doi:10.1029/2001GL013204.

Rosenfeld, D., Y. Rudich, and R. Lahav, 2001: Desert dust suppressing precipitation: A possible desertification feedback loop, Proc. Natl. Acad. Sci. U. S. A., 98, 5975– 5980.

Rosenfeld, D., 2006a: Aerosols, Clouds, and Climate.*Science*, 312, 1323-1324, June.

Rosenfeld, D. 2006b: Aerosol-Cloud Interactions Control of Earth Radiation and Latent Heat Release Budgets".*Space Sci Rev*125 (1-4): 149–157. doi:10.1007/s11214-006-9053-6**.**

Rosenfeld, D., Lohmann, U., Raga, G. B., O'Dowd, C. D., Kulmala, M., Fuzzi, S., Reissell, A., and Andreae, M. O., 2008: Flood or drought: How do aerosols affect precipitation?, Science, 321, 1309–1313.

Rummukainen, M., 2010: nState-of-the-art with regional climate models.WIREs Clim. Change1*,* 82–96*. doi:*10.1002/wcc.008*.*

S

Salgado, R., and P. Le Moigne, 2010: Coupling of the FLake model to the Surfex externalized surface model, Boreal Env. Res., 15, 231-244.

Santos, D., Costa, M. J., and Silva, A. M., 2008: Direct SW aerosol radiative forcing over Portugal, Atmos. Chem. Phys., 8, 5771-5786, doi:10.5194/acp-8-5771-2008.

Santos, D., M. J. Costa, A. M. Silva, R. Salgado, A. Domingues, and D. Bortoli, 2011: Saharan desert dust radiative effects: a study based on atmospheric modelling, *Int. J. Global Warming*, *3*, 88-102.

Salmonson, V. V., Barnes, W. L., Maymon, P. W., Montgomery, H. E., and Ostrow, H., 1989: MODIS: Advanced Facility Instrument for Studies of the Earth as a System, IEEE Trans. Geosci. Remote, 27, 145–153.

Sassen, K., 2002: Indirect climate forcing over the western US from Asian dust storms, Geophys. Res. Lett., 29, 1465, doi:10.1029/2001GL014051.

Schaefer, J. T.: The critical success index as an indicator of warning skill, Weather. Forecast, 5, 570–575, 1990.

Seinfeld J. H. and Pandis S. N., 1998: Atmospheric Chemistry and Physics: From Air Pollution to Climate Change, J. Wiley, New York.

Shao, Y., M. R. Raupach, and J. F. Leys, 1996: A model for predicting aeolian sand drift and dust entrainment on scales from paddock to region, Aust. J. Soil Res., 34, 309–342.

Shao, Y., and H. Lu, 2000: A simple expression for wind erosion threshold friction velocity, J. Geophys. Res., 105 (D17), 22,437–22,444.

Shao, Y., 2000: Physics and modelling of wind erosion, Kluwer Academic Publishers, Boston, 393 pp.

Shao, Y., 2001: A model for mineral dust emission, J. Geophys. Res., 106 (D17), 20,239–20,254.

Shonk, J. K. P., R. J. Hogan, J. M. Edwards and G. G. Mace, 2010a: Effect of improving representation of horizontal and vertical cloud structure on the Earth's radiation budget - 1. Review and parameterisation..Q. J. R. Meteorol. Soc.,136, 1191-1204.

Shonk, J. K. P. and R. J. Hogan. Q. 2010b: Effect of improving representation of horizontal and vertical cloud structure on the Earth's radiation budget -1. Review and parameterisation. J. R. Meteorol. Soc.,136, 1205-1215.

Solomos, S., Kallos, G., Kushta, J., Astitha, M., Tremback, C., Nenes, A., and Levin, Z., 2011: An integrated modeling study on the effects of mineral dust and sea salt particles on clouds and precipitation, Atmos. Chem. Phys., 11, 873-892, doi:10.5194/acp-11-873-2011.

Stamnes, K., S.-C. Tsay, W. Wiscombe, and K. Jayaweera, 1988: Numerically stable algorithm for discrete-ordinate-method radiative transfer in multiple scattering and emitting layered media, Appl. Opt., 27, 2502-2509.

Stanhill, G., and S. Cohen, 2001: Global dimming: A review of the evidence for a widespread and significant reduction in global radiation with discussion of its probable causes and possible agricultural consequences, Agric. For. Meteorol., 107, 255– 278.

Stein J., E. Richard, J.P. Lafore, J.P. Pinty, N. Asencio and S. Cosma, 2000: High -resolution non-hydrostatic simulations of flash-flood episodes with grid-nesting and ice-phase parametrization. Meteorol. Atmos. Phys., 72, 101-110.

Stephens, G. L.,1978: Radiation profiles in extended water clouds. II: parameterization schemes, *J. Atmos. Sci.*, 35, 2123–2132.

Stevens, B. and Feingold, G., 2009: Untangling aerosol effects on clouds and precipitation in a buffered system, Nature, 461, 607–613, doi:10.1038/nature08281.

Swap, R., Ulanski, S., Cobbett, M., and Garstang, M., 1996: Temporal and spatial characteristics of Saharan dust outbreaks, J. Geophys. Res., 101, 4205–4220.

T

Tanré, D., M. Herman, and Y. J. Kaufman, 1996: Information on aerosol size distribution contained in solar reflected spectral radiances. *J. Geophys. Res.,* 101, 19 043–19 060.

Tanré, D., Y. J. Kaufman, M. Herman, and S. Mattoo, 1997: Remote sensing of aerosol properties over oceans using the MODIS/EOS spectral radiances. *J. Geophys. Res.,* 102, 16 971–16 988.

Tegen, I. and A. Lacis, 1996: Modeling of particle size distribution and its influence on the radiative properties of mineral dust. J. Geophys, Res., 101, 19237-19244.

Tegen, I., A. Lacis, and I. Fung, 1996: The influence of mineral aerosols from disturbed soils on climate forcing. Nature, 380, 419-422.

Tost, H., Jöckel, P., Kerkweg, A., Sander, R., and Lelieveld, J., 2006: Technical note: A new comprehensive SCAVenging submodel for global atmospheric chemistry modelling, Atmos. Chem. Phys., 6, 565-574, doi:10.5194/acp-6-565-2006.

Tulet, P., V. Crassier, F. Cousin, K. Suhre, and R. Rosset, 2005: ORILAM, a three-moment lognormal aerosol scheme for mesoscale atmospheric model: Online coupling into the Meso-NH-C model and validation on the Escompte campaign, J. Geophys. Res., 110, D18201, doi:10.1029/2004JD005716.

Tulet, P., M. Mallet, V. Pont, J. Pelon, and A. Boone, 2008: The 7-13 March 2006 dust storm over West Africa: Generation, transport, and vertical stratification, J. Geophys. Res., 113, D00C08, doi:10.1029/2008JD009871.

Twohy, C. H., Kreidenweis, S. M., Eidhammer, T., Browell, E. V., Heymsfield, A. J., Bansemer, A. R., Anderson, B. E., Chen, G., Ismail, S., DeMott, P. J., and Van den Heever, S. C., 2009: Saharan dust particles nucleate droplets in eastern Atlantic clouds, Geophys. Res. Lett., 36, L01807, doi:10.1029/2008gl035846.

Twomey, S. A., 1977: The influence of pollution on the shortwave albedo of clouds, *J. Atmos. Sci.*34, 1149–1152.

Twomey, S. A., 1974: Pollution and the planetary albedo; Atmospheric Environment 8, Issue 12, p. 1251-1256.

W

Wang, W., J. Huang, P. Minnis, Y. Hu, J. Li, Z. Huang, J. K. Ayers, and T. Wang, 2010: Dusty cloud properties and radiative forcing over dust source and downwind regions derived from A-Train data during the Pacific Dust Experiment, J. Geophys. Res., 115, D00H35, doi:10.1029/2010JD014109.

White, B. R., 1979: Soil transport by winds on Mars, J. Geophys. Res., 84, 4643–4651.

Wiacek, A., T. Peter and U. Lohmann, 2010:The potential influence of Asian and African mineral dust on ice, mixed-phase and liquid water clouds, Atmos. Chem. Phys. ; 10 ; 8649-8667

Wilhelmson, R., and Y. Ogura, 1972: The pressure perturbation and the numerical modelling of a cloud, J. Atmos. Sci., 29, 1295-1307.

Z

Zender, C., H. Bian, and D. Newman, 2003: The mineral dust entrainment and deposition (DEAD) model: Description and global dust distribution. *J. Geophys. Res.* 108 (D14):4416.

Zhang, J., and S. A. Christopher, 2003: Longwave radiative forcing of Saharan dust aerosols estimated from MODIS, MISR, and CERES observations on Terra, Geophys. Res. Lett., 30(23), 2188, doi:10.1029/ 2003GL018479.